The Dissertation Committee for Pratixa Paritosh Joshi Certifies that this is the approved version of the following dissertation:

Near-IR Plasmonic Contrast Agents for Molecular Imaging, Cells Tracking and Clinical Translation

Committee:

Konstantin Sokolov, Supervisor

Stanislav Emelianov

Jeanne Stachowiak

Keith Johnston

Haley Tucker

Near-IR Plasmonic Contrast Agents for Molecular Imaging, Cell Tracking and Clinical Translation

by

Pratixa Paritosh Joshi, B.E., M.S.

Dissertation

Presented to the Faculty of the Graduate School of

The University of Texas at Austin

in Partial Fulfillment

of the Requirements

for the Degree of

Doctor of Philosophy

The University of Texas at Austin

May 2014

Dedication

To my parents, mother-in-law, husband and daughter for their unconditional love and support.

Acknowledgements

I am truly grateful to many people for the successful completion of this dissertation. First, I am indebted to my supervisor, Dr. Konstantin Sokolov (Kostia), for his full support while I progressed toward completion. His continuous encouragement, mentoring, openness to new ideas, and persistently positive attitude contributed significantly to this dissertation.

I would like to thank my committee members Dr. Stanislav Emelianov (Stas), Dr. Keith Johnston, Dr. Haley Tucker, and Dr. Jeanne Stachowiak for their insightful discussions and providing guidance throughout the project.

I give special gratitude to the past and present members of the Biomedical Optics and Nano-Diagnostics lab: Maria, Frank, Albert, Justina, Tim, Leonid, Jesse, Nate, Kort, Veronika, Linda, Wendy, Ryna, Aris; members of the Ultrasound Imaging and Therapeutic Research laboratory: Soon Joon, Yun-Sheng, Seungsoo, Carolyn, Doug, Jason, Geoff, Mohammad, Pieter, Salavat, Andrei, Iulia, Srivalleesha, Bo, Jimmy, Alex, Seung Yun, Laura, Juili, Katie, Min, Kimberly; Avi, William and Bobby from Dr. Johnston's lab as well as David from Dr. Stachowiak's lab for having numerous useful discussions, giving helpful feedback to my research, and contributing to a conducive environment. I am also very grateful for having wonderful undergraduate researchers: Angel, Neil, Vincent, Priya, Vanessa, Lea, Alex, Stivaly, Angela, Austin, Ascher, and Jeja, who not only contributed many hours of research but also provided me with an excellent opportunity to become a better mentor. Apart from the names mentioned here, many other people have contributed to the success of this project and I am very thankful to them.

I would like to extend my special thanks to my previous supervisor at the University of Texas Health Science Center at Houston, Dr. Jodie Conyers (Jay), who had encouraged me to pursue my doctorate.

Last but certainly not the least, I am very fortunate to have a wonderful family. Special thanks to my husband (Paritosh) for contributing a tremendous amount of time, energy, and patience. His love and motivation is paramount to my success. I am especially indebted to my daughter (Hetva) for all the time she has supportively spent without her mother at such an early age. I am grateful for receiving continuous blessings and encouragements from my parents (Arvindbhai and Manglaben) and my mother-in-law (Shakuntalaben) who are also my role models.

Near-IR Plasmonic Contrast Agents for Molecular Imaging, Cell Tracking and Clinical Translation

Pratixa Paritosh Joshi, Ph.D.

The University of Texas at Austin, 2014

Supervisor: Konstantin Sokolov

Gold nanoparticles attain an intense focus in biomedical imaging applications due to their unique optical properties, facile conjugation with biomolecules, and biocompatibility. Although a considerable amount of work towards the development of gold nanoparticles has been completed, these promising contrast agents have not yet reached the clinic due to several challenges including efficient accumulation at the diseased site, sensitivity of detection *in vivo*, potential adverse effects, and clearance from the body. High signal-to-background ratio is required to enhance sensitivity of detection. Because near infrared (near-IR) light has the best tissue penetration, contrast agents designed to work in this range can significantly increase imaging sensitivity. Moreover, efficient targeting of the molecular biomarkers on diseased cells can decrease the required dosage, increase the site-specific accumulation, and enhance the imaging sensitivity. Molecular-specific contrast agents developed in this project use directional attachment of antibody molecules to the nanoparticle surface, enhancing the targeting efficacy. Additionally, cell-based delivery of diagnostic and therapeutic agents is gaining much interest due to the immune cells' special access to the avascular, diseased regions. The contrast agents developed in this project enable detection of just a few cells per unit of imaging volume, enable multiplex imaging, and open up a possibility for tracking different cell populations

with noninvasive photoacoustic and ultrasound imaging. Finally, the clearance of nanoparticles from the body dictates their clinical translation. The *in vivo* pharmacokinetics study along with the proposed *in vitro* model explored in this project will enable fast, reliable, and cost-efficient screening of promising agents and facilitate quick optimization of nanoparticles for their potential use in the clinic.

Table of Contents

List of Tables

List of Figures

Chapter 1: Introduction

1.1 Background

In the past century, medical imaging has made a revolutionary leap by creating six imaging modalities used in the clinic; namely, plain film x-ray and computed tomography (CT), magnetic resonance imaging (MRI), single-photon emission computed tomography (SPECT), positron emission tomography (PET), ultrasound (US) imaging, and optical imaging. [1] The first x-ray photograph, taken by Wilhelm Conrad Rontgen in 1895, marked the beginning of the revolution. All other current imaging techniques developed in the last century have facilitated the diagnosis and treatment of various anomalies. Inspired by x-ray technology, however, only in 1975 did Sir Godfrey Newbold Hounsfield introduce the whole-body CT scanner to medical practice. With the advent of the CT scanner, 3D whole-body imaging became feasible. Although the introduction of CT along with exogenous contrast agents enabled acquiring structural information, it did not necessarily provide any functional or disease-specific information.

In 1974, Raymond Vahan Damadian received the first patent on the concept of NMR to "scan" the human body to detect cancerous tissue. In 2003, Paul C Lauterbur and Peter Mansfield were awarded a Nobel Prize for the discovery of the MRI. This modality enabled detection of cancer based on differential relaxation times of normal and cancerous tissue without the use of ionizing radiation.

Dr. Karl Theodore Dussik published the first paper on medical ultrasonics in 1942. Later in 1950, Professor Ian Donald developed a technology and applications for ultrasound. The ultrasound technique is non-invasive imaging that uses high-frequency sound waves to generate images of soft tissue.

The invention of artificially produced radioisotopes by Frederic Joliot-Curie and Irene Joliot-Curie in 1934 inspired the commencement of nuclear imaging. Radioactive tracers are distributed differently throughout the body as the normal and diseased tissue process them differently. In 1961, James Robertson led the team that invented the first single-plane PET scanner at Brookhaven National Laboratory. Soon after, SPECT imaging was introduced. Both PET and SPECT show the distribution of radioisotopes and provides functional imaging of the tissue. However, none of these imaging techniques give anatomical/morphological information about the tissue. The integration of CT with PET and SPECT in 2001 and 1999, respectively, enabled combining metabolic sensitivity of PET and SPECT with the temporal and spatial resolution of CT.

Optical imaging uses tissue properties to absorb and scatter light to generate an image. Optical imaging involves different techniques including diffuse reflectance,[2] photon scattering, [3-5] multi-wavelength spectroscopy,[6] autofluorescence spectroscopy, [7] polarization spectroscopy, [8] and optical coherence tomography.[9, 10] This imaging modality offers safe, fast, high resolution and high sensitivity imaging with the use of molecular-specific contrast agents, although the *in vivo* imaging capabilities are limited due to scattering and absorption of visible light by the tissue. Diffuse optical imaging increases light penetration in tissue (up to 10 cm), albeit with reduced resolution. Near infrared light can penetrate deeper as body tissue does not scatter this light and the use of molecular-specific contrast agents enables highly sensitive high-resolution molecular-specific imaging.

Figure 1.1 illustrates the key imaging modalities used in the current clinical practice as well as in the pre-clinical setting. Because the need to diagnose different anomalies at an early stage to improve prognosis, optical and photoacoustic imaging modalities are

gaining much interest in these years. These modalities not only increase sensitivities but also reduce risks associated with the use of ionizing radiation.

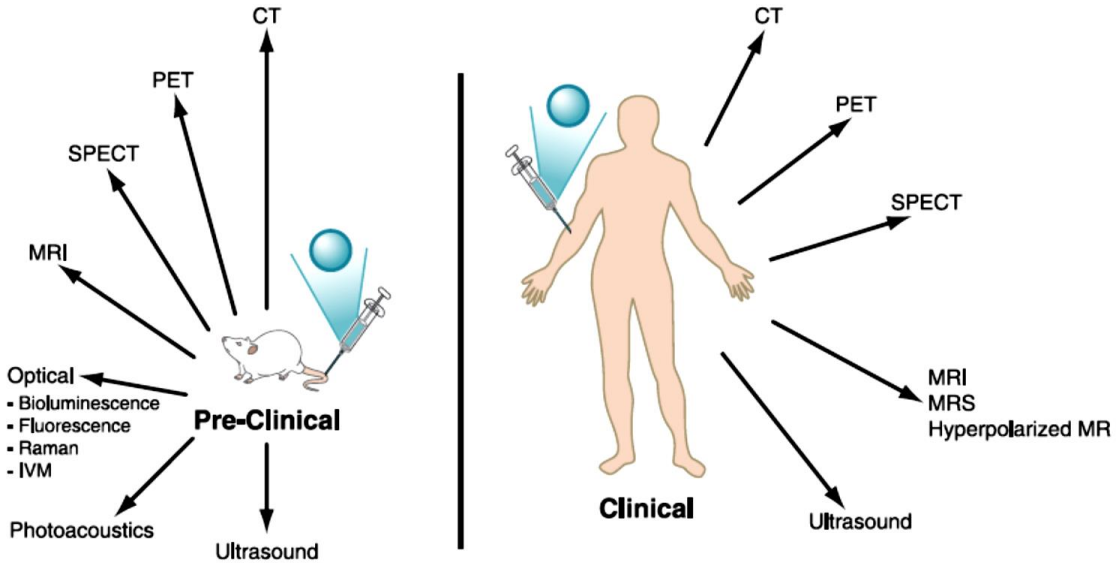

Figure 1.1 Key molecular imaging modalities used for preclinical and/or clinical applications. CT, computed tomography; PET, positron emission tomography; SPECT, single photon emission computed tomography, MRI, magnetic resonance imaging; MRS, magnetic resonance spectroscopy; IVM, intravital microscopy. Blue circle, appropriate contrast agent or molecular imaging agent. (Reprinted with permission from ref. [11]).

Of the current imaging techniques available to a clinician, x-rays, CT, PET, and SPECT use ionizing radiation and/or radioactive contrast agents to produce images. Ionizing radiation has long been known to have adverse side effects, including an increased risk of cancer. [12, 13] Additionally, PET and SPECT imaging offer low resolutions of 8x8x8 mm and 12x12x12 mm, respectively, and cannot facilitate early detection of diseases such as cancer or enable imaging of small metastasis. [14] MRI provides a safer alternative with a similar resolution as CT (1x1x1 mm), however, high cost and limited

molecular imaging capabilities necessitate further improvement for current clinical diagnosis problems.

Ultrasound imaging is cost-effective, does not use non-ionizing radiation or a radiotracer for generating contrast, and has a decent resolution of 1x1x1 mm, however it can only provide morphological information. For efficient diagnosis, functional information about the state of the disease along with anatomical details is very important. More recently, photoacoustic (PA) imaging has been developed where functional information can be obtained. Figure 1.2 exemplifies a potential use of PA imaging in a clinical setting to reveal disease-specific information. Additionally, molecular-specific details can be obtained by utilizing customized optical absorbers that can label diseased sites. Through a combination with ultrasound imaging, PA imaging reveals morphological and disease-specific information with high resolution. [15-21] PA imaging does not use ionizing radiation or require any radioactive tracers to generate images; hence, this modality provides a safer alternative to the currently used clinical imaging modalities. In photoacoustic imaging, short laser pulses irradiate tissue. Tissue absorbs optical energy of the laser and converts it into thermal energy, which causes thermal expansion of the tissue proportional to the amount of absorbed optical energy. An ultrasound transducer then records this thermal expansion to generate an image. As photoacoustic imaging offers safe, cost-effective, non-invasive, real-time and high resolution molecular-specific imaging,[22, 23] our project uses this imaging modality along with optical imaging.

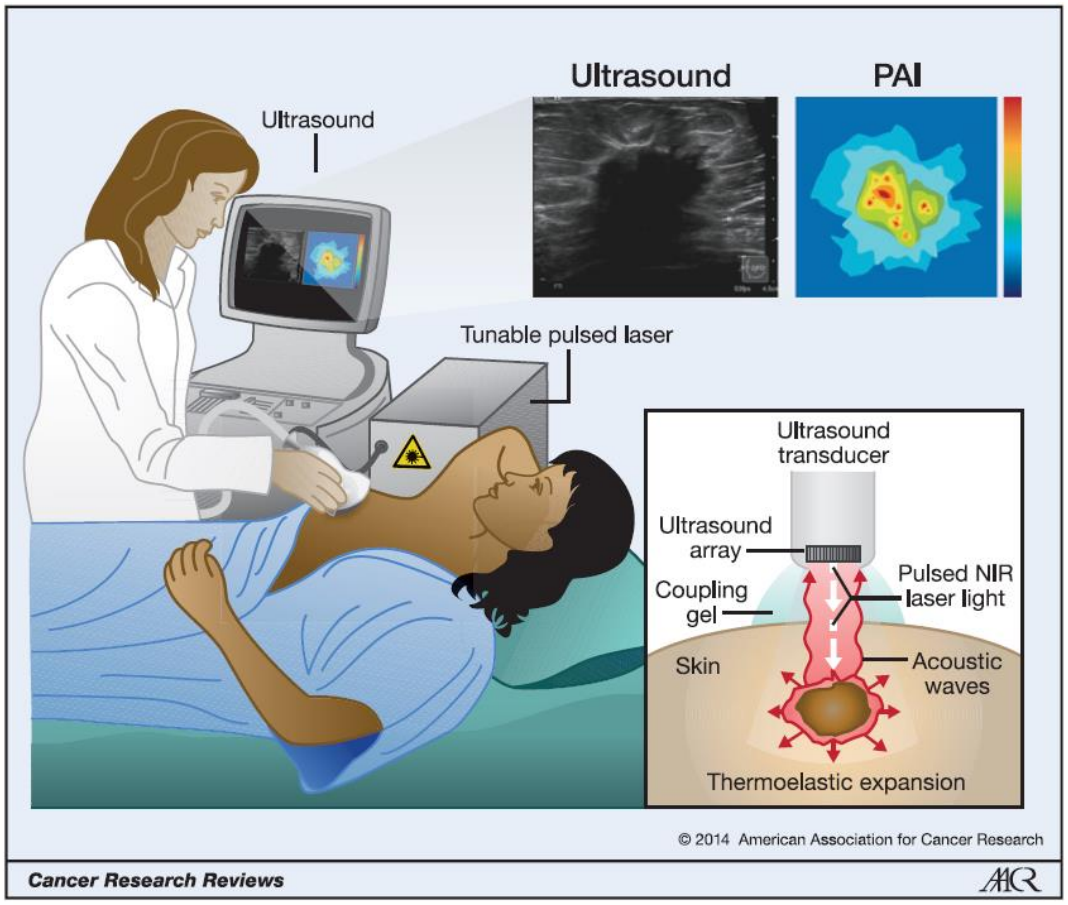

Figure 1.2 Principles of photoacoustic imaging (PAI) presented for a potential clinical application: diagnostic breast imaging by integrated real-time photoacoustic/ultrasound imaging. The laser sends nanosecond pulses of NIR light through the transducer into the tissue. This light is then absorbed inside the tissue (at different levels for each tissue type/component) causing a localized transient thermoelastic expansion. This expansion leads to the emission of pressure waves (ultrasound), which can be detected by the array in the transducer. Finally, a photoacoustic image is calculated and displayed in real-time. At the same time, the ultrasound system can be used in its b-mode to provide structural information about the tissue, in addition to the functional/molecular information obtained by PAI, and both images can be displayed on the viewing screen together (either next to each other or integrated). (Reprinted with permission from ref. [23]).

1.1.2 Nanoparticles as imaging agents

In past three decades, various nanomaterials gained attention for their use in biomedical imaging: carbon-based nanomaterials, semiconductor quantum dots and metallic nanoparticles. This section briefly discusses these materials and their importance in biomedical imaging along with the challenges associated with their potential uses in clinical settings.

Carbon nanoparticles gained specific interest from the biomedical community after the discovery of fullerenes[24] and single-walled carbon nanotubes[25] in 1985 and 1991, respectively. Fullerenes was explored as stable carrier of radioactive tracers for nuclear imaging[26] and Gadolinium for MR imaging[27] because of their resistance to metabolism. More recently single-walled carbon nanotubes (SWNTs) are gaining much interest in various imaging modalities because of their unique properties such as fluorescence emission in the near-IR range, strong Raman scattering, strong absorbance in near-IR region, and strong T2 weighted contrast when metal impurities are present. [28] Because of these properties, SWNTs can serve as contrast agents in multiple imaging modalities such as near-IR fluorescence imaging,[29, 30] Raman imaging,[31] MR imaging,[32-34] PET imaging,[35, 36] SPECT imaging[37, 38], and photoacoustic imaging. [39-44] These carbon nanomaterials show promise for facilitating multiple imaging techniques based on their physical properties. However, *in vivo* distribution of these carbon nanomaterials shows that they cannot be metabolized by the body, thereby staying in the RES organs for a long period of time and potentially causing long-term toxicity. [45-48] A study has also shown that long strands of carbon nanotubes can cause carcinogenic effects similar to asbestos.[49] Additionally, evidence suggests that these materials can cross the blood-brain barrier,[50] which may cause additional challenges if the intended purpose is not to use them for brain targeting and imaging.

Quantum dots are semiconductor crystalline solids with dimensions in the 1 to 10 nm range.[51] Following their discovery in the early 1980s,[52, 53] the first demonstration of their application in biological imaging occurred in 1998. [54, 55] Because of their stability against photobleaching, capacity for multiplex imaging, and high sensitivity, the use of fluorescent quantum dots in biological imaging has exploded in past decade.[56] However, the toxicity of quantum dots has restrained their use to *in vitro* diagnostic applications.

Metal nanoparticle's history dates back to around 300 A.D. as the Lycurgus cup (now housed in the British Museum) demonstrated unique optical effects due to the incorporation of gold nanoparticles in glass, although back then they lacked the knowledge of nanoparticles.[57] With invention of the electron microscope,[58] many different types of colloidal nanoparticles were investigated around the mid-20th century. [59] Currently there are multitudes of applications using different metallic nanoparticles including iron, silver, and gold.[60] These nanoparticles are reaching the clinic as the imaging and therapeutic agents (Table 1.1). Superparamagnetic iron oxide (SPIO) nanoparticles are FDA approved as MRI contrast agents since 1996. More recently, gold nanoparticles with various surface modifications are approved for their use in clinical trials to facilitate photothermal therapy and targeted delivery (Table 1.1). Plasmonic nanoparticles, including nanospheres,[61-65] nanoshells,[66-69] nanocages,[17, 70-72] and nanorods,[20, 73-77] are of increasing interest to biomedical engineers due to their biocompatibility, facile surface modification, and high optical cross section that can provide a high contrast for optical-absorption-based imaging techniques. The optical properties of plasmonic nanoparticles strongly depend on their size and shape. Spherical nanoparticles absorb visible light around the 520 nm wavelength; however, by increasing anisotropy or creating a core-shell structure the plasmonic nanoparticles can strongly absorb near-IR light. As the

rod-shaped gold nanoparticles have a higher absorption coefficient than that of core-shell particles or spherical particles,[78, 79] this project further develops gold nanorods for imaging applications.

Commercial name	Compound	Function	Target disease	Development stage
Feridex I.V.®	Dextran-coated SPIO	MRI contrast agent	Liver tumors	FDA approval in 1996
GastroMARK™	Silicone-coated SPIO	MRI contrast agent	Gastrointestinal forms of cancer	FDA approval in 1996
Resovist®	Carboxydextrane-coated SPIO	MRI contrast agent	Liver tumors	EU approval in 2001
Acticoat	Silver nanoparticles	Antimicrobial barrier dressing	Wound healing	FDA approval in 2005
NanoTherm	Aminosilane-coated SPIO	Magnetic thermotherapy	Brain tumors Prostate and pancreatic carcinoma	EU approval in 2010 Phase I
NBTXR3	Hafnium oxide nanoparticle	Radiation therapy	Soft-tissue sarcoma	Phase 1
-	Silica-gold nanoparticles	Photothermal ablation of atherosclerotic plaques	Atherosclerosis	Phase 1/phase 2
AuroShell®	Gold@silica nanoshells	Photothermal therapy	Refractory head and neck cancers Primary and metastatic tumors in the lung	Phase 1 Approved by FDA for clinical trials in 2012
Aurimmune	TNF-α-bound PEGylated colloidal gold particles	Targeted delivery of TNF-α	Solid tumors	Completed phase 1
Cornell dots	Silica nanoparticles embedded with fluorophores or radioactive iodine	Fluorescence/PET contrast agents	Cancer	Approved by FDA for clinical trials in 2011

Abbreviations: FDA, US Food and Drug Administration; PET, positron emission tomography; phase 1/2, clinical trial phases; SPIO, superparamagnetic iron oxide nanoparticle; TNF, tumor necrosis factor.

Table 1.1 Inorganic nanoparticles on the market and in clinical trials (Reprinted with permission from ref. [80])

Visible light is heavily absorbed and scattered by normal tissue; therefore it has a poor penetration depth. Near infrared (near-IR or NIR) light is least absorbed by typical tissue components like water, hemoglobin, melanin, fat and can be effectively delivered deeper in the tissue.[81] Hence, contrast agents that have high absorption in the near-IR region can dramatically enhance the signal-to-noise ratio and allow deeper imaging within tissue for optical-absorption-based imaging modalities,[77, 82, 83] including photoacoustic imaging. [16, 84] This project develops optimized near-IR contrast agents for photoacoustic and optical imaging.

Anisotropic gold nanorods provide a convenient combination of properties for biomedical applications.[85-87] Plasmon resonances of gold nanorods can be easily tuned in the red-to-NIR spectral region by changing the aspect ratio[78] that allows simultaneous imaging of multiple biomarkers. [76, 88] Strong near-IR extinction cross-sections of nanorods have been used for two-photon luminescence[74, 89] and photoacoustic[90-92] imaging of thick biological samples as well as for photothermal destruction of cancer cells. [93-95] Additionally, anisotropic arrangement of the epidermal growth factor receptor (EGFR)-targeted gold nanorods on the surface of cancer cells produces surface-enhanced Raman scattering that could be used as a marker of EGFR overexpressing cells.[96] Further success in biomedical applications has led to clinical trials with the use of gold nanoparticles in head and neck cancer[97] and for the treatment of atherosclerosis.[98, 99]

1.1.3 Molecular-specific imaging and targeting using NPs

In this section, molecular-specific imaging refers to imaging of contrast agents directed to particular molecular markers on diseased cells. This differs from molecular imaging [100] in nuclear medicine in which cancerous and normal cells metabolize a

radioactive tracer differently, facilitating the detection of tumors using one of the nuclear imaging modalities such as PET or SPECT. However, these imaging modalities can use molecular-specific targeting by using a molecular-specific radioactive tracer to label the cancer cells.[101]

Molecular-specific imaging offers earlier diagnosis of disease by labeling specific cell populations that are overexpressing certain molecular markers. Specifically, molecular imaging plays a pivotal role in the detection of a small number of cancer cells such as circulating tumor cells, facilitating early indication of cancer metastasis. In addition, molecular-specific imaging significantly reduces the dose of contrast agents and facilitates high signal-to-background ratio for sensitive and selective imaging. Reduction in exogenous contrast agents also reduces the potential dose-dependent side effects as well as the cost of imaging. Apparent benefits of molecular-specific imaging and treatment have encouraged the biomedical community in recent years to invest more in the development of targeted imaging and therapeutic agents. Nanoparticles-based platform offers a convenient way to incorporate targeting, therapeutic, and multimodal imaging capabilities by integration of different functional components to design multifunctional nanoparticles (Figure 1.3). Multifunctional nanoparticles can be designed by incorporation of the imaging and therapeutic agents within liposomes, micelles, or a silica matrix. Alternatively, nanoparticles such as gold or iron oxide providing primary imaging contrast can be conjugated with different targeting and function molecules, facilitating design of multifunctional nanoparticles.

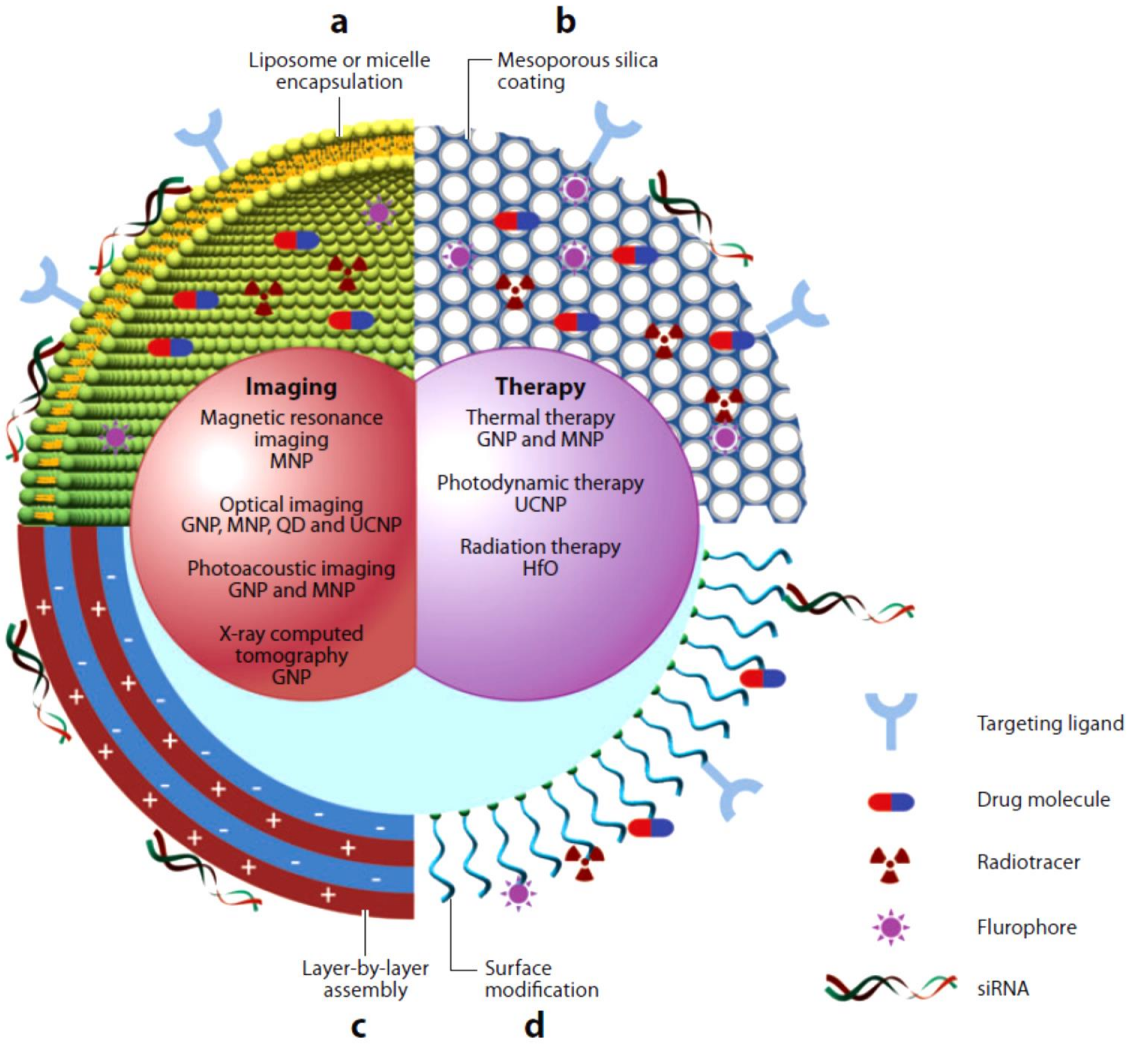

Figure 1.3 Schematic diagram of multifunctional nanoparticles. Multifunctional nanoparticles can be generated by either combining nanocrystals with different functionalities or combining nanocrystals with functional small-molecule cargos through different surface engineering strategies. Four typical coatings developed for inorganic nanocrystals are (*a*) liposome or micelle encapsulation, (*b*) mesoporous silica coating, (*c*) layer-by-layer assembly, and (*d*) surface modification. Abbreviations: GNP, gold nanoparticles; HfO, hafnium oxide nanoparticles; MNP, magnetic nanoparticles; QD, quantum dot; UCNP, upconversion nanoparticles. (Reprinted with permission from ref. [80]).

Although the multiple drugs based on nanoparticle platforms for cancer treatment have been approved for clinical use do not have targeting capacity yet, the importance of targeting for drug efficacy is revealed by multiple ongoing clinical trials that use transferrin,[102] antibody fragment,[103] or peptide as targeting ligands for cancer cell markers. [104] Multiple targeting moieties such as antibody, antibody fragments, peptide, aptamer, affibody, and small molecules targeting specific receptors can facilitate targeting of drugs or nanoparticles to the specific biomarker on the cancer cells or on the tumor vasculature. [105] Gold nanoparticles are explored as a contrast agents for CT, MRI, fluorescence, SERS, photoacoustic imaging, and optical imaging due to their x-ray attenuation capability, strong light absorption, intrinsic fluorescence, or incorporation of other contrast generating molecules in gold nanoparticles. [106-108] Apart from their use as multimodal contrast agents, various research groups perform molecular-specific imaging using gold nanoparticles. [109-115] The molecular-specificity translates to the clinic as revealed by the use of gold nanoparticles conjugated with recombinant human tumor necrosis factor (rhTNF) alpha, facilitating tumor targeting in recent clinical trials with no toxic effects at the highest dose tested, which was three-fold higher than the previously-established maximum tolerable dose (MTD) for rhTNF alone. [116]

1.1.4 Cell tracking with nanoparticles

Cell tracking plays a vital role in cell-based therapy, regenerative medicine, unfolding pathologies of different diseases, as well as in understanding trafficking of cells during different disease stages. Immune cells such as microphages play a dual role in specific diseases such as cancer. Tumor-associated macrophages can reach otherwise inaccessible areas of the necrotic core and play an essential role in tumor growth. Labeling immune cells with the contrast and therapeutic agents not only unfolds the mystery of how

these cells traffic within tumors but also provides a tool to deliver the therapeutic agents to eradicate the surviving cancer stem cells in the hypoxic tumor regions.

A surge in cell-based therapy in early stage clinical trials necessitates safe and reliable methodologies to track cells in order to predict their *in vivo* fate and therapeutic outcome. [117] Advances in the nanoparticles-based cell tracking involve use of iron oxide nanoparticles for MRI, [118, 119], gold nanoparticles for CT imaging, [120, 121], various radionucleotides for PET and SPECT imaging, [122] [123] and microbubbles for ultrasound imaging. [124, 125] Considering the risk of ionizing radiation for CT and nuclear imaging and the excessive cost of MRI imaging, this project does not investigate these modalities. Gold nanoparticles in this project are developed as multimodal contrast agents facilitating *in vivo* cell tracking using noninvasive photoacoustic and ultrasound imaging along with *ex vivo* validation capabilities using fluorescence imaging.

1.1.5 Clinical translational of nanoparticles

Clinical translation of nanoparticles as contrast agents depends on multiple factors including biocompatibility, blood half-life, signal-to-background ratio, and clearance of nanoparticles within a reasonable timeframe after imaging. Figure 1.4 illustrates the fate of nanoparticles after administration and the potential toxicity during their absorption, distribution, metabolism and excretion (ADME). Carefully tailored nanoparticles having desirable pharmacokinetics can facilitate clinical translation.

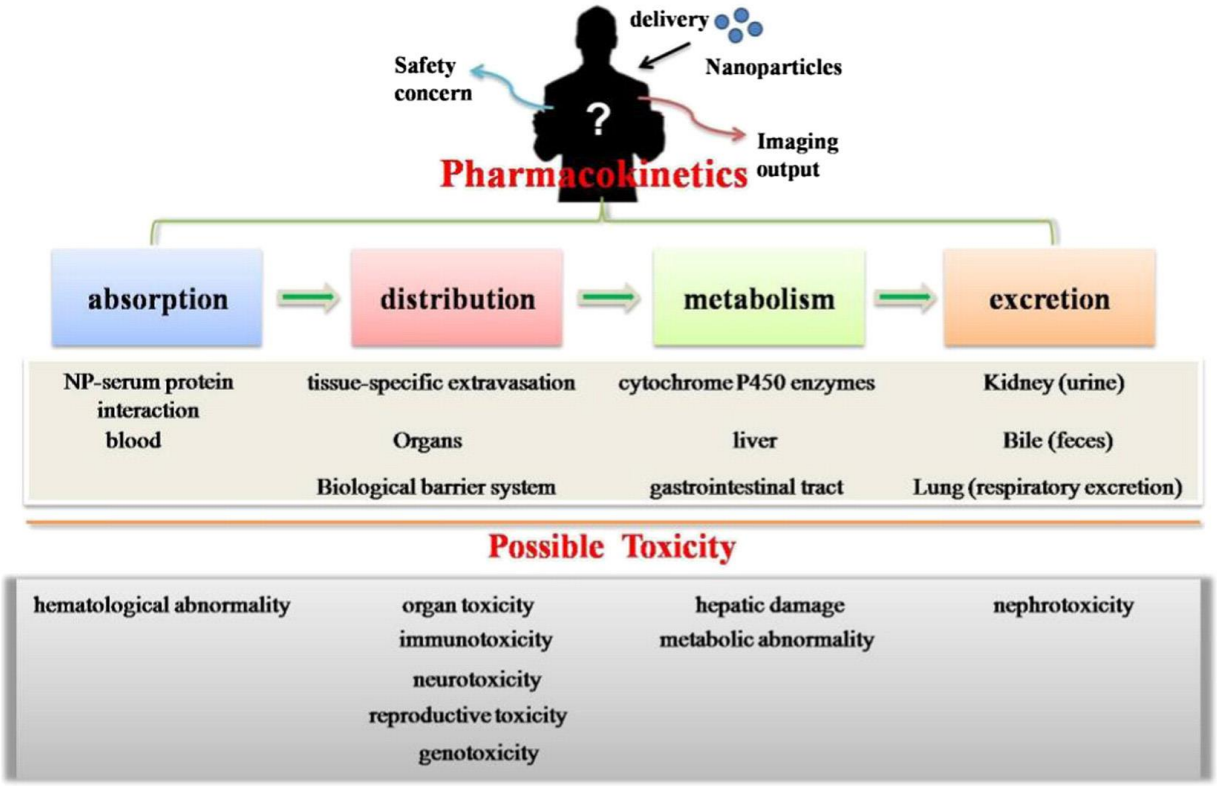

Figure 1.4 An illustrative scheme for the pharmacokinetics of extraneous nanoparticles in vivo and possible toxicities that may arise. Nanoparticles, after delivered into the body, undergo the process of pharmacokinetics. They are absorbed and brought into the bloodstream where nanoparticle–serum protein interactions frequently occur. Then they spread into tissues and organs via tissue-specific extravasation from the bloodstream. Afterwards, they may be metabolized in the liver by cytochrome P450 enzymes and some may start metabolic process early in the gastrointestinal tract. Finally, the remnant nanoparticles will be removed from the body via the kidney (urine) or bile (feces). At each step of this process, toxicity may arise. Among them, hematological abnormality, organ toxicity and immunotoxicity arise from the long-term retention of nanoparticles in the liver, lung, spleen and kidney. Moreover, nanoparticles may cross the biological barrier system (blood–brain barrier, placental barrier, etc.) and neurotoxicity, reproductive toxicity may be induced. Genotoxicity may also appear. In addition, nanoparticles probably disturb the normal metabolic functions and induce metabolic abnormality. (Reprinted with permission from ref. [126]).

Toxicity of the gold nanoparticles depends heavily on their size, surface coating, and surface charge. Well-investigated physical properties of these nanoparticles have led us to produce biocompatible formulations for biomedical imaging applications. [126-129] The nanoparticles less than 5-nm in size clear efficiently through RES; however, they do not have enough blood residence time to allow successful accumulation in the organ of interest. [130, 131] However, the larger nanoparticles with enough blood residence time after proper surface modifications tend to accumulate in the clearance organs. [132]

Recent clinical trials represent great potential for plasmonic nanoparticles to be clinically relevant, [97-99, 116] but widespread use of these agents is still questionable because of their long-term accumulation in RES (reticuloendothelial system). [132-134] Although the use of these nanoparticles does not cause acute toxicity after optimized design,[135, 136] the clearance of any foreign material is highly warranted for their successful translation to the clinic. A major determinant of the clearance of non-degradable nanoparticles is their exocytosis from the cells of different organ, facilitating their eventual renal clearance or clearance through the bile and reducing their long-term toxicity. Table 1.2 summarizes current literature on exocytosis of different types of nanoparticles from different cells. Vast body of the literature suggests that the size and surface characteristics of the nanoparticles along with the exocytosis environment and the type of cells play a crucial role in the excretion of nanoparticles. Biodegradable gold nanoclusters synthesized using 5-nm primary gold nanoparticles can impart enough blood residence time for imaging, and have the potential to clear through RES after biodegrading in the acidic environment of the cells. [137, 138] With strong near-IR absorbance, the gold nanoclusters can also be imaged using noninvasive photoacoustic imaging modality *in vivo*. [139] The final part of this dissertation evaluates gold nanoclusters for their clinical translation potential.

Table 1.2 Literature data on exocytosis of nanoparticles by different cells

Type NPs* (size)	Surface coating (Zeta)	Cell type£	Incubation conditions	Method€ to quantify	Exoc-ytosis time	Observations	Ref.
AuNSs (14, 30, 50, 74, 100 nm)	Transferrin	STO, HeLa, and SNB19	0.02nM in DMEM, 10% serum, up to 6 hours	ICP-AES	8 hours	STO (70%,60%, 50%, 43%, 30%); HeLa(38%, 30%, 18%, 12%, 8%); SNB19 (38%, 25%, 10%, 5%, 3%) of 14, 30, 50, 74, 100 nm AuNSs, respectively, exocytosed	[140]
AuNRs (20x30, 14x42, 7x42)	Transferrin	STO, HeLa, and SNB19	0.02nM in DMEM, 10% serum, up to 6 hours	ICP-AES	8 hours	STO (70%, 72%, 71%), HeLa (80%, 82%, 81%). SNB19(74%, 82%, 76%) of 20x30, 14x50, 7x42 nm AUNRs, respectively, exocytosed	[140]
MSN (130 nm)	Phosphonate	A549	40 µg/mL, 2 hours	FM, ICP-AES	6, 24, and 48 hours	65%, 82% and 95% decrease in NPs inside cells after 6, 24, and 48 hours, respectively	[141]
LEVs (3.2 µm disk shaped) loaded with Amine-SPIONs (15, or 30 nm)	Amine-SPION (+20.5 mV)	J774A.1	10 LEV per cell in media	TEM; Prussian blue assay	7 days	Release of 9% (15nm) and 6% (30 nm) of amine-SPIONs	[142]

Table 1.2 (continued)

Type NPs* (size)	Surface coating (Zeta)	Cell type£	Incubation conditions	Method€ to quantify	Exoc-ytosis time	Observations	Ref.
PLGA (97 ± 3 nm)	BSA (–20 ± 1 mV)	VSMCs	100 µg/mL in medium with or without serum, 1 hour	CFM, HPLC	30 mins	65% and 85% exocytosis after 30 mins and 6 hrs; exocytosis was inhibited without serum	[143]
Quantum dots (8 nm)	D-penicillamine (-40 mV)	Hela cells	10 nM, 1.5 hours	CFM	4 hours	50% exocytosed with exocytosis half-life 21 min reaching plateau at 2 h.	[144]
AuNSs (15 +- 2 nm)	OEG with inhibitor (-20 mV) or mutant (-17mV) peptide. Size after conjugation is 35 nm	HUVECs	8 nM in media with 20% serum, 4 hours	ICP-AES	2, 4, or 6 hours	40% exocytosis; Inh-NPs show linear exocytosis; Mut-NPs show 25%, 10% and 40% exocytosis at 2,4, and 6 hours, respectively	[145]
micelles of PMMA-b-P(PEGMEMA) without (20 nm) and with (25 nm) cross linking; LY	without (-5 mV) and with (+5 mV) cross linking	OVCAR-3	100 ug/mL, 1 hour	FS	2 hours	less than 3%, 25% and 40% exocytosis of micelle, cross-linked micelle and lucifer yellow (LY)	[146]
CuO NPs (TEM: 20-40 nm; DLS: in water 276 nm, in media with FBS 185 nm)	In water (-29.1 mV), in media with FBS (-7 mV).	A549	CuO NPs (5 and 15 mg/L), 24 hours	FAAS	Up to 24 hours	Exocytosis increased with time (12−24 h).	[147]

Table 1.2 (continued)

Type NPs* (size)	Surface coating (Zeta)	Cell type£	Incubation conditions	Method€ to quantify	Exocytosis time	Observations	Ref.
Silicon QDs (65 nm)	Allylamine (+32 mV)	HUVECs	25 - 400 ug/ml for 4 hours	CFM	3 hours	less than 60% exocytosed	[148]
CdSe-CdS core with silica shell (13 nm)	Protein coatings (-18 to -35 mV)	A549	5.0×10^{8} particles/ml in cell culture medium for 24 hours	ICP-MS	24 hours	No statistically significant decrease in NPs per cell	[149]
PS (30 nm), MSN (10 nm)	IRIS-3 on MSN (no charge); FITC on PS (negative charge)	RBL-2H3	10 ug MPS or 75 ug PS NPs for 15 minutes	FLA	1 hours	PS NPs were only faintly detectable in the cells whereas MSN do not show clearance from the cells	[150]
MSN	FITC	HUVECs, HeLa	50 and 100 μ g cm^{-3} for 3 hours	CFM	Up to 40 mins	HUVEC cells show higher transfer of NPs intercellularly than HeLa cells. Presence of serum in media favored exocytosis. No exocytosis for HeLa cells	[151]
Amorphous silica NPs (50 nm)	n/a	H1299, NE083	10 ug/ml in serum free media for 48 hours	TEM	1 or 3 hours	Normal cells (NE083) show significant exocytosis only after 3 hours but H1299 cells do after 1 hour.	[152]
Fluorescent nanodiamond (100 nm)	n/a	HeLa, 3T3-L1, and 489-2.1	80 µg /mL in serum-free media for 4 hours	FLA	6 days	Exocytosis: < 15% for HeLa and 489-2.1 cells; up to 30% for 3T3-L1	[153]

Table 1.2 (continued)

Type NPs* (size)	Surface coating (Zeta)	Cell type£	Incubation conditions	Method€ to quantify	Exoc-ytosis time	Observations	Ref.
FITC-SiO2 NPs (60 nm, 178 nm, 369 nm, 592 nm)	n/a	HepG2	80 µg/mL in culture media for 12 hours	FLA	12 hours	63%, 67%, 58% and 38% exocytosis for 60, 178, 369 and 592 nm NPs, respectively	[154]
HRP, FITC-dextrans (4.1 to 42 kDa).	n/a	CHO cells	16-20 hours	GPC	18-20 hours	Lower MW dextrans exocytosed while 42kDa FITC-dextran and HRP was not exocytosed significantly	[155]
Silver nanoparticles (6-20 nm)	n/a	IMR-90, U251	3 hours	ICP-AES	Up to 48 hours	66% and 10% of NPs were exocytosed by 48 and 2 hours, respectively	[156]

* AuNSs – gold nanospheres, AuNRs – gold nanorods; NPs – Nanoparticles, PS – polystyrene NPs, PLGA – poly(lactic-co-glycolic acid) NPs, BSA – bovine serum albumin, LEVs – logic-embedded vectors, OEG – monocarboxy (1-mercaptoundec-11-yl) hexaethylene glycol, MSNs – Mesoporous silica nanoparticles, LY – lucifer yellow, QDs – quantum dots

£ STO – fibroblast cells, HeLa – ovarian cancer cells, SNB19 – brain tumor cells, A549 – human lung cancer cells, VSMCs – human arterial vascular smooth muscle cells, OVCAR-3 – human ovarian cancer cells, HUVECs – human umbilical vein endothelial cells; H1299 – human lung cancer cells, NE083 – human esophageal epithelial cells, 3T3-L1 – pre-adipocytes, 489-2.1 – multipotent stromal cells, HepG2 – liver hepato carcinoma cells, IMR-90 – Normal human lung fibroblasts, U251 – Human glioblastoma cells

€ FM – Flurescent microscopy, GPC – gel permeation chromatography, FLA – Flow cytometric analysis, CFM – confocal microscopy, FS – fluorescence spectroscopy, FAAS – flame atomic absorption spectrometry, ICP-AES – Inductively coupled plasma atomic emission spectroscopy, ICP-MS – Inductively coupled plasma mass spectrometry, HPLC – High-performance liquid chromatography

1.2 DISSERTATION SUMMARY

A surge in the laboratory-based production of a variety of promising nanoparticles is not yet leading to their use in the clinic for two main reasons: 1) the sensitivity of detection *in vivo* and 2) toxicity and adverse side effects. By directly addressing these problems, this dissertation builds upon current literature and facilitates clinical translation of nanoparticles. First, the sensitivity of detection *in vivo* can be enhanced by obtaining a high signal-to-background ratio and ensuring effective accumulation of contrast agents to the disease site. Toxicity and adverse side effects caused by nanoparticle use can be taken care of by ensuring biocompatibility during systemic circulation, lowering dosage for imaging, and ensuring efficient clearance after the imaging procedure. Chapter 2 develops molecular-specific contrast agents with high specificity and contrast in photoacoustic imaging to ensure efficient targeting of diseased areas and increasing the signal-to-background ratio. Chapter 3 explores an alternate means of contrast agents' delivery and enables tracking of cells with very high sensitivity in a tissue-mimicking environment to detect just a few cells per unit imaging volume. Both chapters 2 and 3 further the translational research by providing molecular-specific contrast agents for targeted imaging as well as multiplex cell tracking capabilities with high sensitivities (Figure 1.5). Chapter 4 evaluates pharmacokinetics of biodegradable contrast agents and develops an *in vitro* model for high throughput screening of promising contrast agents to predict their *in vivo* fate, and thereby directly facilitating their clinical translation.

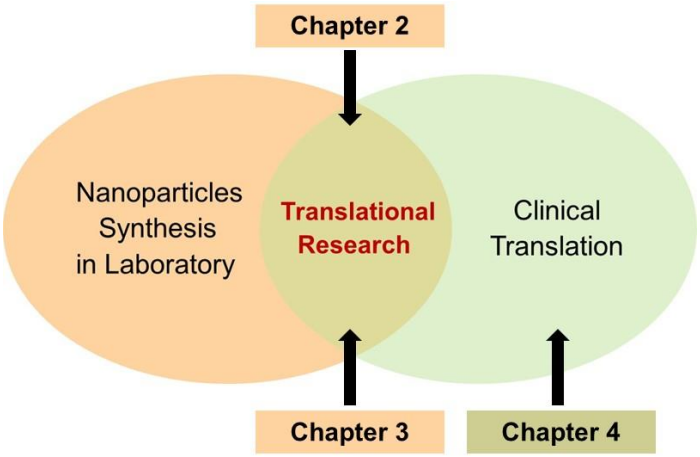

Figure 1.5 Schematic of relevance of different parts of this dissertation towards facilitating translation of the nanoparticles-based contrast agents from the laboratory to the clinic

Chapter 2 develops molecular-specific gold nanorods with tunable absorbance in near-IR range to facilitate *in vivo* imaging using noninvasive photoacoustic and ultrasound imaging. Current literature involves antibody attachment to nanorods with non-directional approaches involving electrostatic or covalent attachment where the antibodies can attach to the nanorod surface in any orientation leaving some of the attached antibodies unable to bind to their target because of the hidden antigen-binding regions. Additionally, characterization of nanorods after different conjugation procedures is not well documented, making it difficult to know if the nanorods are of good quality without significant aggregation after different modifications. Nanorods developed in this chapter maintain high quality after different modifications along with directional attachment to antibodies. The nanorods are conjugated by covalently attaching the Fc portion of the antibody to the nanorods' surface, leaving antigen-binding sites available for targeting. Moreover, by attaching the Fc portion to the nanorod surface, the molecular-specific nanorods can have prolonged blood residence time because they escape Fc receptors-mediated uptake by

macrophages, thereby increasing accumulation in the targeted site. These molecular-specific near-IR contrast agents are evaluated using optical and photoacoustic imaging in a tissue-mimicking environment.

Chapter 3 optimizes multi-modal near-IR contrast agents for immune cell tracking using noninvasive photoacoustic imaging. Upon cellular uptake, the gold nanoparticles plasmon couple due to aggregation in the cellular endosomes, thereby broadening the absorbance spectra of the nanoparticles. Gold nanorods with different aspect ratios have distinct longitudinal absorbance peaks in the near-IR range and therefore can facilitate multiplexing to track different cell populations. Plasmon coupling upon endosomal uptake hinders the feasibility of multiplexing. Moreover, current literature suggests low uptake of rod-shaped nanoparticles compared to spherical nanoparticles by macrophage cells that may again impede efficient tracking of labeled cells. In addition, the current limitation of imaging lies in the sensitivity of detection. This chapter develops a strategy for changing the shape of gold nanorods by coating them with silica to increase macrophage uptake. The silica-shell not only enhances cellular uptake of nanorods by changing their morphology, but also prevents plasmon coupling of gold nanorods after cell uptake, facilitating multiplexing. The silica matrix also incorporates fluorescent dye by covalent linking and provides added imaging capability for *ex vivo* validation. Moreover, this chapter demonstrates the feasibility of detecting only a few cells per unit imaging volume using photoacoustic imaging of a tissue-mimicking gelatin phantom encompassing different concentration of cells loaded with fluorescent silica-coated gold nanorods.

Chapter 4 evaluates biodegradable gold nanoclusters for their *in vivo* pharmacokinetics and develops an *in vitro* screening method for predicting the uptake of nanoparticles by the RES organs. A major limitation in clinical translation of plasmonic nanoparticles includes their clearance after systemic administration. Current literature

reveals that nanoparticles accumulate in the liver and spleen for long periods, potentially causing long-term toxicity. This chapter evaluates the clearance kinetics of biodegradable gold nanoclusters in normal mice. Furthermore, an *in vitro* screening model is developed where the clearance kinetics from the major phagocytic cells in the liver is investigated and compared with *in vivo* results to deduce the fate of novel nanoparticles after systemic administration using *in vitro* studies.

Chapter 2: Molecular-Specific Contrast Agents[†]

2.1 INTRODUCTION

Imaging of diseased region is better accomplished by using a contrast agent that is specifically designed to label the diseased cells.[157] This molecular specificity is obtained by attaching a biomarker-specific protein to the contrast agent. Upon injection of such contrast agent in the body, the molecular-specific contrast agent would only bind to the particular biomarker on diseased cells. The benefits of using molecular-specific contrast agents are high signal-to-background ratio for imaging a diseased region, low dosage necessary to achieve high imaging sensitivity, and reduced toxic effects due to lower dosage of injected agent. Furthermore, while performing therapy along with imaging, the molecular-specificity can reduce adverse side effects of therapy to healthy tissue.

Plasmonic gold nanoparticles have become an area of intense focus in biology and medicine due to their small size and intrinsic properties that offer the potential to solve otherwise intractable problems.[17, 63, 66, 67, 70, 93, 109, 158-178] In general, plasmonic nanoparticles are intrinsically multimodal contrast agents since they exhibit strong scattering and absorption cross sections as well as non-linear optical phenomena such as two-photon luminescence and second harmonic generation when excited at the plasmon resonance frequency. Gold nanoparticles provide high contrast in cellular and tissue imaging using confocal reflectance microscopy,[158, 179] dark-field imaging,[109, 179-182] two-photon luminescence[74, 89, 183] phase-sensitive OCT,[63] and photoacoustic imaging.[17, 18, 64, 166, 184-189] Furthermore, gold nanoparticles have been used to

[†] Adapted with permission from P. P. Joshi, S. J. Yoon, W. G. Hardin, S. Y. Emelianov, K.V. Sokolov Bioconjugate Chemistry, 2013, 24(6), 878-888. Copyright 2013 American Chemical Society. Contribution of the coauthors – S. J. Yoon performed photoacoustic imaging of the phantom, W. G. Hardin performed XPS on prepared samples, S. Y. Emelianov supervised imaging part of the paper, K. V. Sokolov provided overall supervision of the research.

transform light energy into heat in photothermal therapy of cancer either by using near-IR (NIR) absorbing gold nanoshells,[66-69] nanorods,[93] and nanocages[70, 72, 190] or by applying molecular-targeted spherical nanoparticles which undergo molecular-specific aggregation upon interaction with cancer cells that results in strong absorption in the red- to NIR-spectral region due to plasmon resonance coupling.[165, 191] The use of NIR irradiation is essential for *in vivo* applications because NIR light has the best tissue penetration depth.[192, 193] In recent developments, gold nanoparticles have been explored as carriers of nucleic acids such as siRNA or antisense DNA molecules that can be selectively activated or released using light irradiation, which results in remotely triggered gene silencing.[65, 194, 195]

Among all available nanoparticle geometries anisotropic gold nanorods provide a convenient combination of properties for biomedical applications.[85-87] Plasmon resonances of gold nanorods can be easily tuned in the red-NIR spectral region by changing the nanorod aspect ratio[78] that allows simultaneous imaging of multiple biomarkers.[76, 88] Strong NIR extinction cross-sections of nanorods have been used for two-photon luminescence[74, 89] and photoacoustic[90-92] imaging of thick biological samples as well as for photothermal destruction of cancer cells.[93-95] It was also observed that anisotropic arrangement of epidermal growth factor receptor (EGFR) targeted gold nanorods on the surface of cancer cells produces surface-enhanced Raman scattering that could be used as a marker of EGFR overexpressing cells.[96] Furthermore, the anisotropy property of nanorods has been explored for dynamic imaging of rotational motion in 3D space.[196]

We have evaluated feasibility of imaging gold nanorods using combined intravascular ultrasound (IVUS) and intravascular photoacoustic (IVPA) imaging in rabbit model (Figure 2.1). A balloon injured New Zealand white rabbit was injected with

PEGylated gold nanorods and the aorta was excised 26-hours post administration for *ex vivo* imaging.[197] Imaging was performed by Doug Yeager from Dr. Emelianov's lab and the PEGylated gold nanorods were prepared by Pratixa Joshi. Clearly, the nanorods, accumulated by the macrophages in the aorta, can be imaged using combined IVUS and IVPA imaging in either saline or blood environment. While this study demonstrated the feasibility of detecting gold nanorods imaging *in vivo* using photoacoustic imaging, molecular-specific contrast agents are required to enhance specificity and sensitivity of detection, facilitating early detection of a disease.

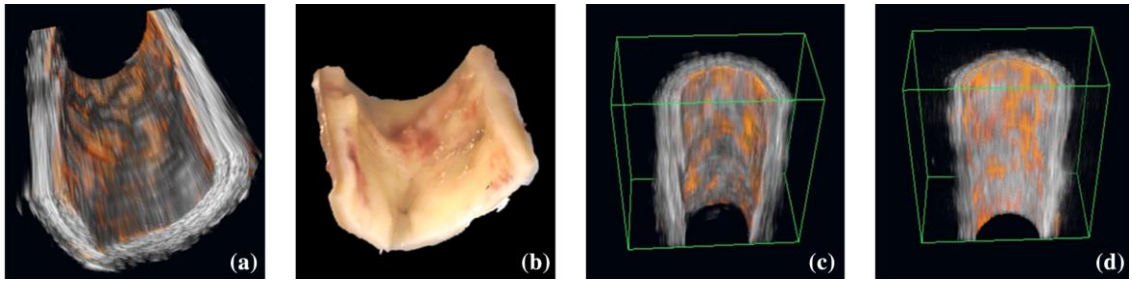

Figure 2.1 Three-dimensional integrated intravascular ultrasound and intravascular photoacoustic (IVUS/IVPA) renderings of gold nanorod (AUNR)-labeled atherosclerotic plaque (color online). (a) Combined IVUS/IVPA rendering of an 8-mm long section of atherosclerotic rabbit artery obtained through saline. (b) Photograph of the corresponding artery section revealing AUNR distribution at the luminal surface (red). Combined IVUS/IVPA images obtained through saline (c), and through blood (d) of aseparate 6-mm arterial section. Step size, 500 μm. (Reprinted with permissions from ref. [197])

Surface modification of nanoparticles is critical for both *in vitro* and *in vivo* applications, as uncoated nanoparticles are colloidally unstable and often cytotoxic in biological solutions.[75, 198-200] Conjugation of biomolecules to nanoparticles furnishes important properties needed for biomedical applications, such as molecular targeting, stealth properties and surface charge. Antibodies are the most widely used targeting moieties due to their high affinity and availability for a large number of established biomarkers.

Bioconjugation of gold nanorods is confounded by the presence of surface layer of cetyl trimethyl ammonium bromide (CTAB).[201] In commonly used synthesis of highly uniform gold nanorods, the CTAB molecules promote crystal growth in one direction resulting in rod-shaped particles.[202] CTAB is stabilized on gold surface as a bilayer by electrostatic interactions between gold and CTAB as well as by hydrophobic interactions within bilayer of CTAB molecules. A recent review by El Sayed's group[86] summarizes current methods of nanorods bioconjugation: 1) electrostatic adsorption of biomolecules directly to the CTAB layer; 2) coating of CTAB layer with one or more layers of charged polymers followed by physisorption or covalent attachment of targeting moieties; 3) bifunctional ligand attachment where CTAB is first replaced by bifunctional linker molecules followed by conjugation of biomolecules; and 4) ligand exchange where CTAB is replaced by small thiolated molecules (Figure 2.2). These conjugation methods have a number of major shortcomings that need to be addressed in order to further optimize gold nanorods for molecular-specific imaging and therapy. In first two approaches, the CTAB bilayer is still present on nanorods that can lead to long term cytotoxicity of the bioconjugates.[203] In addition, the physisorption approach requires a high concentration of antibodies for synthesis of nanoparticle conjugates, results in random orientation of antibodies at the gold surface, and can be prone to antibody replacement by other molecules

in biological samples.[204] In the third approach, the CTAB bilayer was first replaced by small bifunctional linkers with thiol functional groups for interaction with the gold surface and carboxyl groups for covalent attachment of antibodies using carbodiimide chemistry.[88, 205, 206] In this strategy, antibodies are attached through primary amine groups.[207, 208] Because the primary amine groups are present in different regions of antibody molecules, including antigen recognition sites in the Fab region, this approach does not provide control over antibody orientation on the nanoparticle surface, leading to reduced overall activity of the attached antibodies. In addition, this conjugation strategy is prone to aggregation because antibody molecules have both the primary amine and the carboxyl groups, which can act as crosslinking agents between gold nanoparticles. The fourth approach has been used to produce non-specific biocompatible nanorods by replacing the CTAB bilayer with biocompatible ligands such as PEG.[209]

Here we address the shortcomings of previously published conjugation protocols by developing directional attachment of antibodies to gold nanorods using a two-step method (Figure 2.2). First, the CTAB bilayer on nanorods is replaced with methoxy-poly(ethylene)glycol thiol (mPEG-SH). Then, thiolated antibody molecules are attached via Fc portion that does not have antibody binding sites using ligand exchange with mPEG-SH. The directional conjugation is achieved by specific reaction of the carbohydrate moiety located on the Fc portion of most antibodies with a heterofunctional cross-linker; this reaction results in antibodies with a dithiol group located in one specific location – the Fc region. The dithiol enables antibody conjugation directly to the gold surface. We showed that this method produces stable bioconjugates with no aggregation and no cytotoxicity. In addition, it requires significantly reduced amount of antibodies during the synthesis as compared to physisorption methods. We also demonstrated molecular-specific optical and

photoacoustic imaging of epidermal growth factor receptor (EGFR) molecules in cancer cell culture models using the synthesized gold nanorods conjugates.

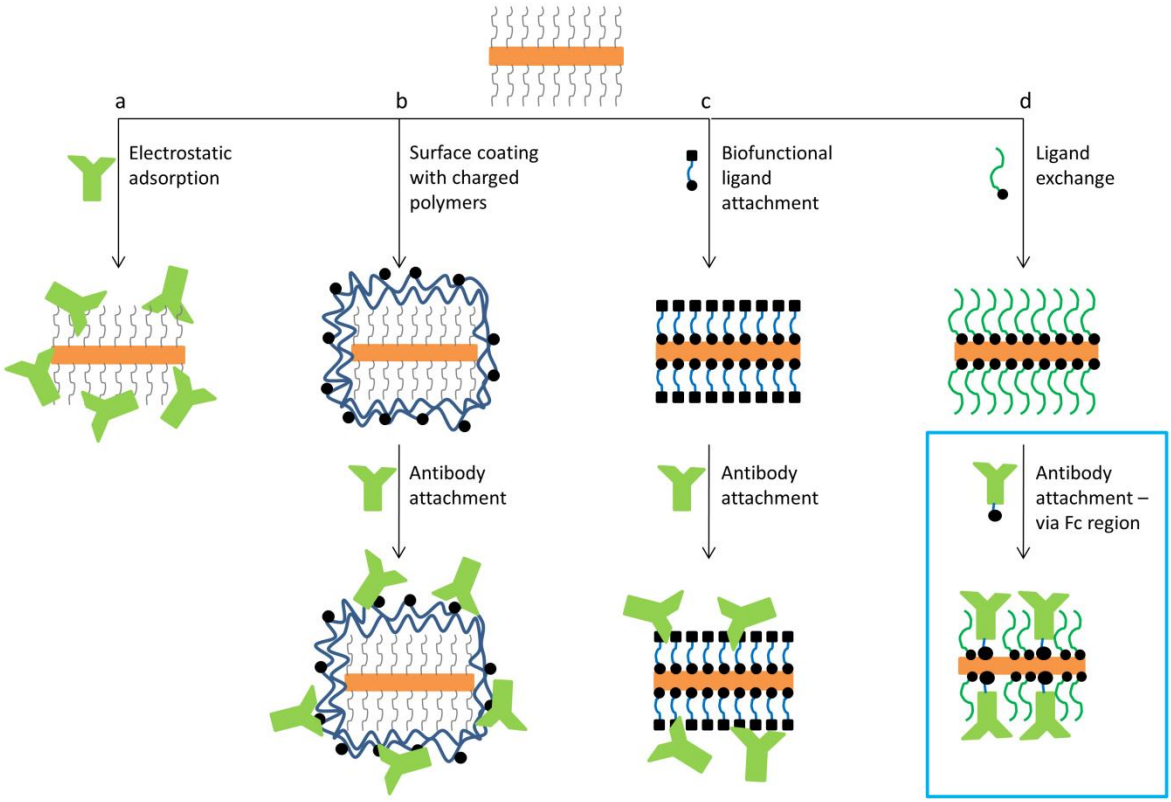

Figure 2.2 Schematic representation of gold nanorods bioconjugation procedures from left to right: electrostatic adsorption of antibodies to CTAB layer on gold nanorods; coating of CTAB nanorods by charged polymers followed by electrostatic adsorption of antibodies; replacement of the CTAB layer using bifunctional ligands followed by covalent attachment of antibodies; the directional conjugation method proposed here that consist of replacement of the CTAB layer with mPEG-thiol molecules followed by directional attachment of antibodies

2.2 RESEARCH APPROACH

2.2.1 Material and Methods

Gold nanorods synthesis: Gold nanorods were synthesized by seed mediated growth mechanism using the previously published protocol.[202] Briefly, 100 µL of 4 mM $AgNO_3$ (Acros Organics, 41936) was added to 10 mL of 0.5 mM $HAuCl_4$ (Sigma, 520918) dissolved in 0.1 M CTAB (Amresco, 0833) water solution. Then, 70 µL of 78.8 mM ascorbic acid (Acros Organics, 401471000) was added to the reaction mixture as a mild reducing agent; this constitutes the nanorod growth solution. In parallel, a seed solution was prepared by mixing 0.6 mL of 10 mM ice-cold $NaBH_4$ (Fisher, S678) to 10 mL of 0.25 mM $HAuCl_4$ dissolved in 0.1 M CTAB solution. To initialize the growth of nanorods, 12 µL of the seed solution was added to the nanorod growth solution within 30 minutes of making the seed solution. Then, the reaction mixture was kept at 30^{o}C for at least 2 hours for completion of nanorod synthesis. The nanorods were washed twice in water by centrifugation at 18000x g for 45 minutes. The final nanorod pellet was dispersed in water and stored at room temperature. Nanorods were 20-times concentrated compared to the as-prepared nanorods.

Gold nanorods bioconjugation: The nanorods were bioconjugated in two steps (Figure 2.3). The first step involved replacement of the CTAB layer on nanorod surface with methoxy-PEG-thiol (mPEG-SH). One hundred microliters of 0.5 mM mPEG-SH with molecular weight 2000 Da (Creative PEGworks, PLS-605) in water were mixed with 1 mL of CTAB-NRs (20-times concentrated compared to as-prepared nanorods) and sonicated using a water bath sonicator (Branson 1510R-MT) for 30 minutes at room temperature. After sonication, free CTAB and mPEG-SH molecules were removed by centrifugation using 100 KDa centrifugal filters at 2500xg for 15 minutes. Then, the nanorods were

washed one time with water to remove any residual mPEG and CTAB. The prepared mPEG-NRs were dispersed in 1 mL water and stored at room temperature.

In the second conjugation step, the carbohydrate moiety on Fc portion of anti-EGFR clone 225 (Sigma, E2156) or RG-16 (Sigma, I0138) antibodies were thiolated following previously published protocol developed by our research group.[210] Briefly, antibodies were concentrated using 50 kDa MWCO centrifugal filter and were dissolved in 100 mM Na_2HPO_4, pH 7.5 buffer at 1 mg/mL. Then, 10 µL of 100 mM $NaIO_4$ in water was added to 100 µL of antibody solution and the mixture was incubated in dark for 30 minutes. The reaction was quenched by adding 500 µL of 1x PBS. At this point the carbohydrate moieties on the Fc portion of the antibody were oxidized to aldehyde groups.[210, 211] Then, 140-times molar excess of heterofunctional linker dithiolaromatic PEG6-CONHNH2 (SensoPath Technologies, SPT-0014B) was added to the antibody solution. The linker has hydrazide and dithiol groups on opposing ends of the molecule. The hydrazide moiety interacts with aldehyde groups of the Fc portion of the modified antibody molecules. The reaction mixture was incubated at room temperature for 1 hour and then the thiolated antibodies were collected using centrifugal filters and resuspended in 0.1 M sodium phosphate buffer, pH 7.5. Two hundred microliters of the thiolated anti-EGFR antibodies at concentration of 1 mg/ml were mixed with 0.1 mL of mPEG-NRs and the suspension was incubated at room temperature for 24 hours under moderate shaking. Finally, the antibody-nanorod conjugates were washed twice in 0.1 M sodium phosphate buffer (pH 7.5) by centrifugation to remove unbound antibodies. After the final wash, the antibody-nanorod conjugates were redispersed in buffer or phenol free cell culture media.

For fluorescence imaging experiments, the antibodies with oxidized carbohydrate moieties were labeled with AlexaFlour dye (Invitrogen, A-20186) before attachment of the

heterofunctional linker. The labeling was carried out using antibody-labeling kit purchased from Invitrogen.

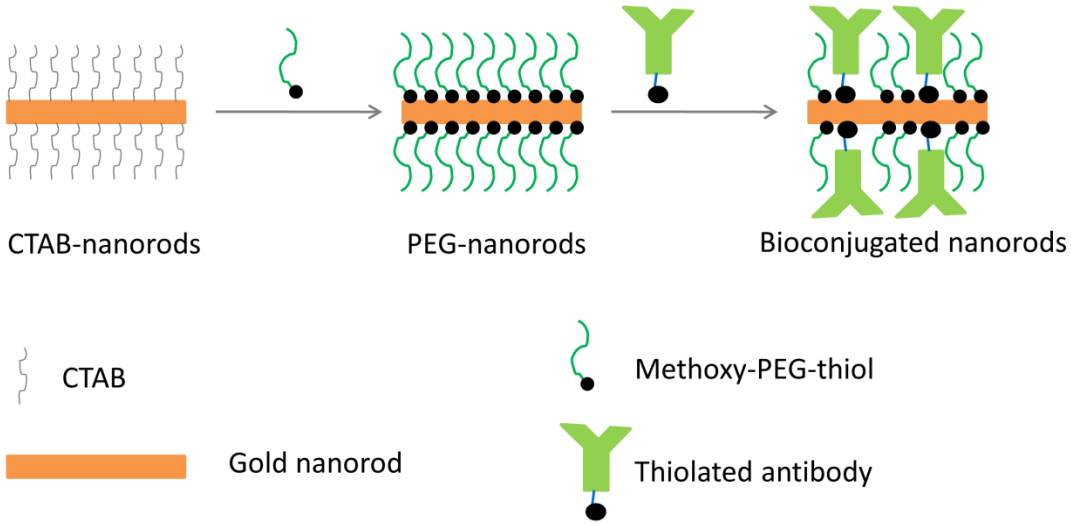

Figure 2.3 Schematic illustration of the directional conjugation synthesis proposed here.

Amount of antibodies per nanorod: Gold nanorods were conjugated with fluorescently labeled antibodies to quantify the number of antibodies per nanorod. First, a calibration curve was plotted by measuring fluorescent emission peak intensity as a function of known concentrations of fluorescently labeled antibodies mixed with PEGylated nanorods at optical density of 0.1 cm^{-1}. The calibration measurements were carried out in the presence of nanorods to account for a decrease in fluorescence signal due to absorbance by gold nanorods. Then, suspensions of nanorod conjugates with fluorescently labeled antibodies were thoroughly washed from any residual free antibody molecules and were diluted to the optical density of 0.1 cm^{-1} to match the calibration measurements. The fluorescence

emission of the conjugates was measured and the number of conjugated antibodies was determined using the calibration curve. To calculate the number of antibodies per nanorod, we carefully analyzed the average size of the nanoparticles using transmittance electron microscopy (TEM) and the gold concentration using inductively coupled plasma mass spectrometry on an Agilent ICP-MS system.

Specificity of molecular labeling: EGFR expressing human A431 cells and EGFR-negative human MDA-MB-435 cells were cultured in phenol-free DMEM (Invitrogen, 11039) and MEM (Invitrogen, 41061) culture media, respectively, supplemented with 10% fetal bovine serum (FBS) at 37ºC in a 5% CO2 environment. Antibody conjugated gold nanorods were incubated with either A431 cells or MDA-MB-435 cells for two hours at room temperature at a concentration of approximately $2x10^6$ cells per milliliter of conjugated nanorods (at the same nanorods concentration as as-prepared nanorods). Unbound gold conjugates were separated from cells by centrifugation at 200x g for 3 minutes followed by washing cells with fresh cell culture media. The labeled cells were characterized by UV-Vis spectroscopy (BioTek Synergy HT) and optical microscopy. Bright-field transmittance and fluorescence (Cy5 filter cube, ex/em – 649/670 nm) images were taken with Leica DM600 upright microscope, and hyperspectral images were acquired using a PARISS spectral imager (Lightform Inc.). For all imaging, 20x 0.5 NA objective and 100 W halogen light source were used. The hyperspectral system was calibrated using a standard low pressure Hg wavelength calibration lamp (Lightform, Inc.). The hyperspectral images obtained from cells were normalized by the lamp spectrum obtained from the part of the microscope slide that did not have cells. RGB images were taken using a 12-bit color mosaic CCD camera (SPOT Pursuit XS, Diagnostic Instruments).

Cell viability study: Biocompatibility of nanorods was characterized using MTS assay after incubation of A431, MDA-MB-435 and murine macrophage (J774A.1) cells with either 0.3 nM CTAB-NRs or PEG-NRs in phenol-free cell culture media supplemented with 10% FBS for 6 hours at 37°C. After removal of nanorods and washing once with PBS, the MTS reagent (mixture of MTS (3-(4,5-dimethylthiazol-2-yl)-5-(3-carboxymethoxyphenyl)-2-(4-sulfophenyl)-2H-tetrazolium) (Promega, G111B) and PMS (phenazine methosulfate) (Sigma, P9625) prepared in phenol free cell culture media) was added to the cells treated with nanorods and to untreated control cells. Absorbance at 490 nm wavelength is proportional to the number of metabolically active live cells in a sample. Background absorbance before adding MTS reagent was subtracted to calculate cell viability.

Tissue mimicking phantom preparation: Gelatin based tissue-mimicking phantoms with cell inclusions were fabricated for combined photoacoustic and ultrasound imaging. To simulate tissue background, 6 % gelatin solution with 0.1 wt% of 15 μm silica particles was used to prepare base and top layers which encapsulated cell inclusions. Specifically, suspension of A431 cells only and A431 cells labeled with anti-EGFR gold nanorods were prepared at concentration of 4×10^7 cells/mL. Each cell suspension was mixed with the same volume of 12 wt% gelatin solution containing 0.2 wt% 15 μm silica particles at 37°C. The mixture of cells and gelatin was placed on the base layer of 6 wt% gelatin with 0.1 wt% silica particles. Then, the top layer of gelatin/silica particles was added to complete the phantom.

Photoacoustic imaging set-up: The ultrasound and photoacoustic imaging system consisted of a microprocessor unit that utilized a custom-built LabVIEW program to allow synchronization between the ultrasound pulser/receiver, data acquisition unit, pulsed laser and 3D motion axis. Figure 2.4 depicts the imaging set-up used in this study. The images were taken using 25 MHz single element focused transducer (f/# = 4, focal length = 25.4 mm), and the excitation light was delivered by a 1.5 mm diameter optical fiber. A tunable OPO laser with 7 ns pulse duration and 10 Hz pulse repetition rate was used to generate photoacoustic signal. The 2D ultrasound and photoacoustic images were obtained by mechanically scanning over the region of interest with 100 μm lateral step. To improve signal-to-noise ratio, 10 photoacoustic A-lines were collected and averaged.

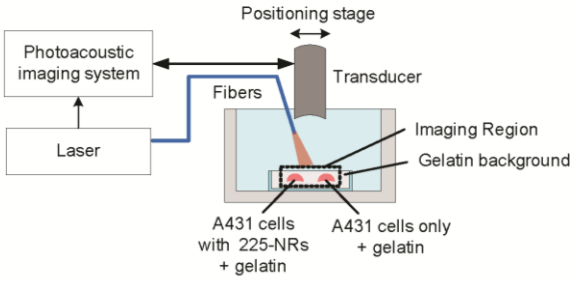

Figure 2.4 Schematic of the experimental set-up used to obtain combined ultrasound and photoacoustic images

X-ray Photoelectron Spectroscopy (XPS): XPS data was acquired using a Kratos AXIS Ultra DLD spectrometer equipped with a monochromatic Al X-ray source (Al α, 1.4866 keV). High resolution elemental analysis was performed on the O 1s, C 1s, N 1s, S 2p and Au 4f regions with a 40 eV pass energy, utilizing 0.1 eV steps, and dwell time of 4 sec per step. Charge compensation was used for the CTAB and PEG controls, in addition to CTAB

and PEG-coated nanorods. All absolute energies were calibrated relative to gold, and graphite. The peak positions and areas are calculated using a standard sum Gaussian-Lorentzian fit with a linear (O, C, N, S) or Shirley (Au) background correction.

Determination of CTAB/PEG ratio and CTAB surface coating by XPS: The CTAB to PEG ratio on the surface of PEG-coated gold nanorods was determined from the integration of the N 1s and O 1s peaks in the XPS spectrum. CTAB molecule contains one N and no O atoms, while 2 KDa mPEG-SH has no N and 46 O atoms. As a result we have the following relationship between molar fractions of N (y_N), O (y_O), CTAB (y_{CTAB}) and PEG (y_{PEG}) on the PEG-coated nanorods.

$$y_N = y_{CTAB} \quad \text{(I)}$$

$$y_O = 46 * y_{PEG} \quad \text{(II)}$$

Integration of the N 1s and O 1s peaks in XPS spectrum of PEG-nanorods yields N/O ratio (y_N / y_O) of 0.105. Using this ratio and the above relationships, we determined that the molar ratio of CTAB to PEG (y_{CTAB}/y_{PEG}) on the surface of PEG-coated nanorods is 4.8. Then, the following equation was used to find the number of surface ligands:

$$N_{CTAB} * f_{CTAB} + N_{PEG} * f_{PEG} = A * 0.9 \quad \text{(III)}$$

where, N_{CTAB} is the number of CTAB molecules on the nanorod surface divided by 2 because CTAB molecules are present on the surface as a bilayer; N_{PEG} is the number of PEG molecules on the nanorod surface; f_{CTAB} and f_{PEG} are footprints of CTAB and PEG molecules, respectively; and A is the surface area of a nanorod. Recent report showed that the footprint of CTAB on gold nanorods (f_{CTAB}) is *ca.* 0.27 nm^2.[212] It was shown that mPEG molecules can have a high density packing with f_{PEG} = 12 nm^2 and a low density packing with f_{PEG} = 38 nm^2.[213] The factor of 0.9 arises from the approximation of ligand attachment as close-packed circles on a planar surface.[214] Considering the 15nm x 40nm

gold nanorods used in this study, the calculated amount of residual CTAB on gold nanorods after replacement with PEG is 2.3% for low density PEG and 7.1% for high density PEG; the CTAB coverage on initial CTAB nanorods is considered to be 100%.

2.3 RESULTS

Schematic of the conjugation process is shown in Figure 2.3. CTAB-coated gold nanorods have high positive surface charge due to presence of the cationic surfactant (Table 2.1). After replacement of CTAB with mPEG-SH the surface potential decreases from 50 mV for CTAB-coated nanorods to approximately 8 mV for mPEG-coated nanorods. These values correlate well with previously published literature [209] showing the same decrease in zeta potential after modification of nanorods with mPEG-thiol molecules. TEM images of CTAB-coated and PEG-coated nanorods show no change in morphology of nanorods after removal of CTAB layer (Figure 2.5, A).

Type of nanorods	**Zeta potential, mV**
CTAB-NRs	50.34 ± 0.8
PEG-NRs	8.33 ± 0.46
225-NRs	-16.26 ± 1.55
RG16-NRs	-24.34 ± 0.54

Table 2.1 Changes in surface charge of gold nanorods after modifications with mPEG-thiol molecules and with antibodies.

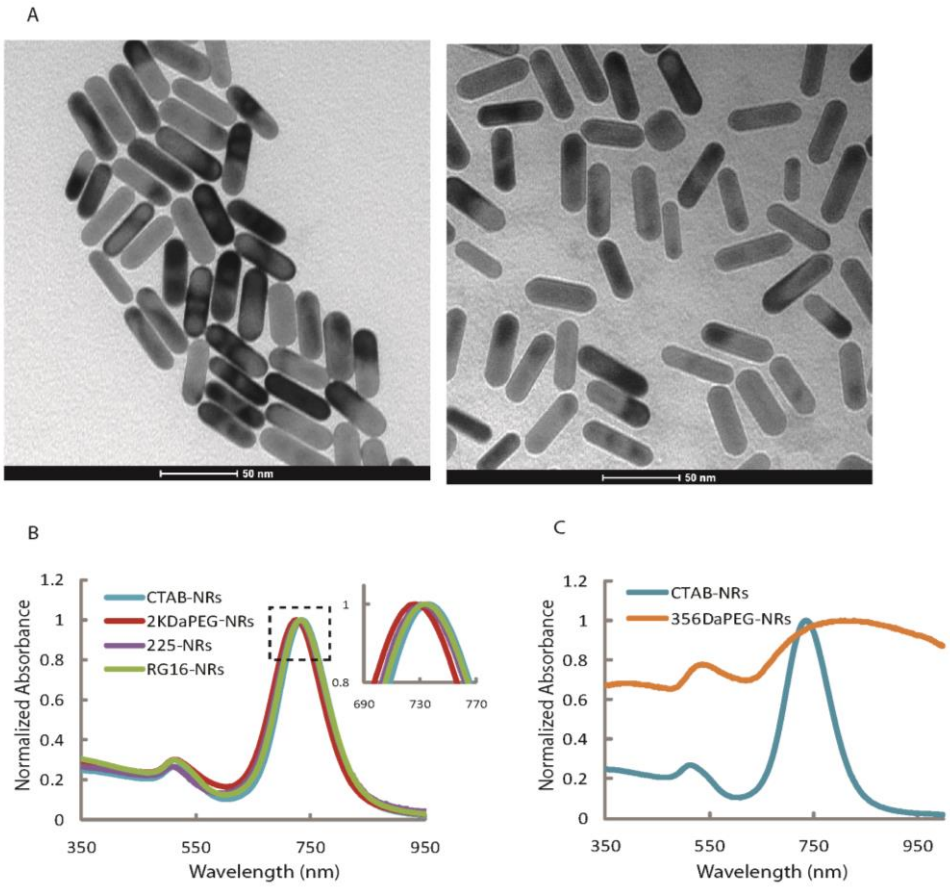

Figure 2.5 A) Transmittance electron microscopy images of as-prepared CTAB-coated gold nanorods (left) and the nanorods after modification with mPEG-thiol molecules (right). B) Extinction spectra of as-prepared gold nanorods (blue) and the nanorods after modification with 2 kDa mPEG-thiol (red), clone c225 (purple) and RG16 (green) antibodies. c) Comparison of extinction spectra of as-prepared gold nanorods (blue) and nanorods after ligand exchange using small molecular weight, 356 Da MW, mPEG-thiol molecules (orange). Aggregation of nanorods is evident from profound spectral changes (orange spectrum).

To confirm that CTAB was replaced by PEG, high resolution X-ray photoelectron spectroscopy (XPS) was performed on CTAB-coated and PEG-coated nanorods. A similar analytical analyses was recently reported by Griesser et al.[215] The C 1s, O 1s, N 1s, S 2p and Au 4f core level spectra from nanorod samples and from pure CTAB and PEG were collected and analyzed. The spectra for CTAB-coated nanorods showed four core level regions: O 1s (1.5 rel. at.%), C 1s (92.5 rel. at.%), N 1s (4 rel. at.%) and Au (2 rel. at.%) (Figure 2.6). The C 1s spectrum consisted principally of $(-CH_2-CH_2-)_n$ functionality (285 eV), but displayed slight asymmetry. The very low signal from Au is most likely due photoelectron scattering in the dense CTAB bilayer. The spectra of PEG-coated nanorods revealed five core levels: O 1s (19 rel. at.%), C 1s (65 rel. at.%), N 1s (2 rel. at. %), S 2p (1 rel. at. %) and Au 4f (13 rel. at.%). The C 1s spectrum of PEG-coated nanorods differed greatly from that of CTAB-coated particles. The spectrum showed two peaks corresponding to two chemical states (Figure 2.6). The deconvolution of these two peaks revealed PEG functionality ($(-CH_2-CH_2-O_2-)_n$ 286.5 eV, 60 rel. at.% of C 1s) and CTAB functionality ($(-CH_2-CH_2-)_n$, 285 eV, 40 rel. at.%) (Figure 2.6). Additionally, an order of magnitude increase in O 1s signal at 532.8 eV, interpreted as a C-O functionality, clearly demonstrates the presence of $(-CH_2-CH_2-O-)_n$ repeat units of PEG molecules.[216] Furthermore, the increase in Au signal indicates that the Au 4f core level photoelectrons experience less scattering events. This is consistent with the exchange of the CTAB bilayer for a less-dense PEG layer.

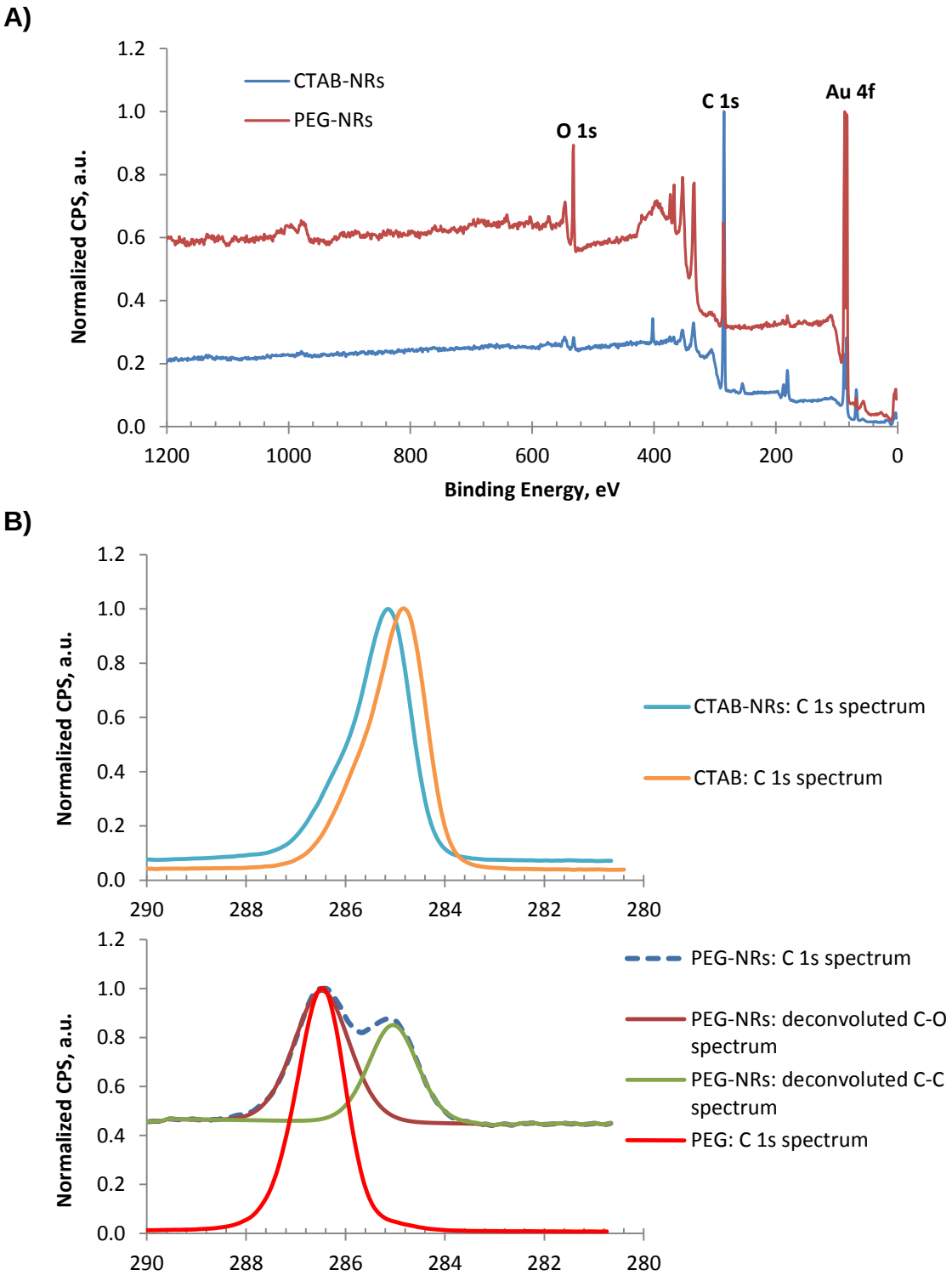
A)
CTAB-NRs
PEG-NRs
O 1s
C 1s
Au 4f
Normalized CPS, a.u.
Binding Energy, eV
B)
Normalized CPS, a.u.
CTAB-NRs: C 1s spectrum
CTAB: C 1s spectrum
PEG-NRs: C 1s spectrum
PEG-NRs: deconvoluted C-O spectrum
PEG-NRs: deconvoluted C-C spectrum
PEG: C 1s spectrum

Figure 2.6

C)

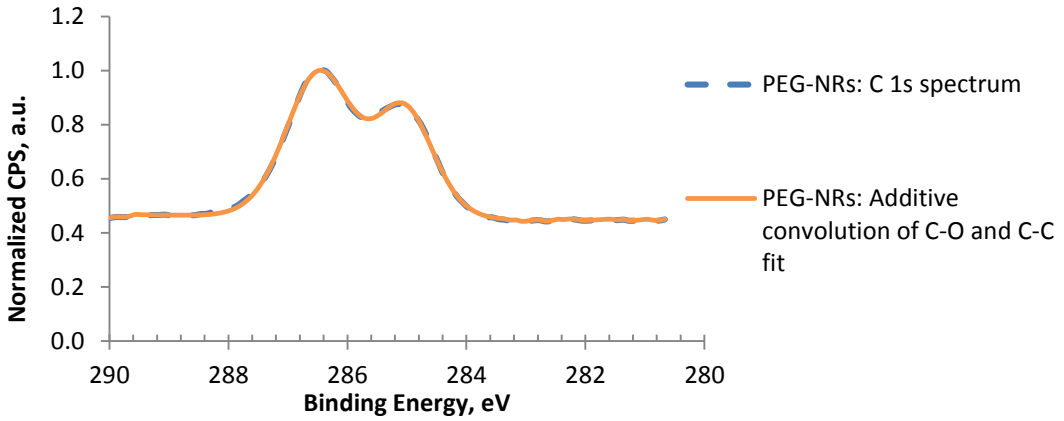

Figure 2.6 A) Survey scans of CTAB-NRs and PEG-NRs from XPS measurements; B) C 1s core spectra for CTAB, CTAB-NRs, PEG-SH and PEG-NRs. The PEG-NR spectrum shows contributions of C-O and C-C bonds. Electronic shift observed for CTAB-NRs as compared to pure CTAB is likely due to interactions between Au and CTAB whereby gold is more electron withdrawing. Such shifts are characteristic of oxidation, indicating that the CTAB ligand on the nanorods is partially oxidized. C) Overlay of C 1s spectrum for PEG-NRs and additive convolution of C-O and C-C spectrum to show the degree of agreement between the XPS collected spectra and the deconvolution.

The percentage of residual CTAB molecules after replacement with PEG was calculated using the XPS data and previously reported footprints of mPEG polymers[213] and CTAB molecules.[212] Because mPEG molecules can attach to surfaces at a high (brush conformation) or a low (mushroom conformation)[213] densities, the residual amount of CTAB on nanorod surface can vary from ca. 2.3% to 7.1% as compared to the initial CTAB surface coating for low and high PEG density, respectively (see Methods section for detailed calculations). The corresponding changes in zeta potential from ca. +50 mV for CTAB nanorods to ca. +8 mV for PEG nanorods suggest a high-density confirmation of PEG molecules on the surface of nanorods (Table 2.1). Zeta potential

measurements indicate approximately 16% of residual positive charge on the surface of PEG-coated nanorods as compared to CTAB nanorods while XPS measurements show 7.1% of residual CTAB surface coverage for a high density PEG confirmation. This discrepancy might be due to an increased contribution to positive zeta potential by the CTAB molecules adjacent to the gold surface in a CTAB bilayer that is disrupted by PEG molecules.

After completion of CTAB replacement with mPEG-SH, dithiol-linked antibodies were added to the PEGylated nanorods. The linker was attached to the Fc antibody moiety to achieve directional conjugation on the gold surface. Two types of antibodies were used in this study: EGFR specific clone 225 and non-specific anti-rabbit IgG clone RG-16. Conjugation of antibodies decreases zeta potential to -16 and -24 mV in the case of clone 225 and clone RG-16, respectively (Table 2.1). The observed negative zeta potential after modification with antibodies correlate well with literature[217] and provide indirect evidence of antibody conjugation. We achieved 6.5 ± 1.8 antibodies conjugated per nanorod based on fluorescence emission spectra of nanorod-conjugates prepared with fluorescently labeled antibodies.

Extinction spectra show ca. 8 nm blue shift in the longitudinal peak of PEGylated nanorods as compared to CTAB-nanorods with no peak broadening (Figure 2.5, B). Attachment of antibodies results in approximately 6 nm red shift of the longitudinal peak relative to the PEGylated nanoparticles for both 225 and RG-16 modified nanorods. The observed spectral shifts can be attributed to changes in the refractive index of the local environment surrounding the nanorods. This effect has been well documented in the literature.[218, 219] The spectral characterization also provides an important and simple way to monitor possible aggregation of plasmonic nanoparticles during a conjugation procedure. This process can be easily monitored using characteristic spectral changes

associated with nanorod aggregation that include three major features: significant broadening, strong red shift of the longitudinal peak and increase in transverse to longitudinal (T-to-L) peak ratio (Figure 2.5, C). Molecular-specific nanorods synthesized here using proposed conjugation strategy show mean value of T-to-L peak ratio increase less than 9 % (Table 2.2). In addition, the full-width at half maximum of the longitudinal peak does not increase with the PEGylation or antibody conjugation as evident from Figure 2.5 (B) and Table 2.2. These spectroscopic data confirm that nanorods do not aggregate during conjugation with antibodies.

	FW at HM, nm	**% increase in transverse to longitudinal peak ratio**
CTAB-Nanorods	109.7 ± 7.4	
mPEG(2K Da)-Nanorods	100.5 ± 7.5	8.1 ± 2.1
225Ab-Nanorods	107 ± 4.6	8.9 ± 2.8
mPEG(356 Da)-Nanorods	337.3 ± 66.1	277.4 ± 44.0

Table 2.2 Spectral characteristics of plain gold nanorods and conjugates of gold nanorods.

It is important to note that the molecular weight of mPEG-SH molecules used to replace CTAB layer during the first conjugation step is very important. In this study, 2 KDa mPEG-SH was used to produce stable molecular-specific nanorods. The use of lower molecular weight (356 Da) mPEG-SH led to nanoparticle aggregation as evident from significant broadening and a more than 100 nm red-shift in the longitudinal peak with more than 250% increase in the T-to-L peak ratio (Figure 2.5, C and Table 2.2). The use of higher

molecular weight (5 kDa) mPEG-SH resulted in stable nanorod suspensions. However, attempts to conjugate antibodies to these nanorods failed as they did not label EGFR expressing cells. This can be attributed to a steric hindrance effect that did not allow antibodies to replace high molecular weight PEG molecules from nanorod surface.

CTAB-coated gold nanorods are known to have cytotoxic effects.[220, 221] Therefore, we characterized cellular toxicity of nanorods after replacement of CTAB with mPEG-SH molecules. The cell viability study was performed using two different cancer cell lines (EGFR expressing A431 and EGFR negative MDA-MB-435) and a macrophage cell line (J774A.1). As expected, the CTAB-coated nanorods were highly toxic in all cell lines (Figure 2.7). Replacement of CTAB with mPEG-SH resulted in biocompatible nanorods, which did not exhibit any cytotoxic effects in any of the cell lines studied (Figure 2.7).

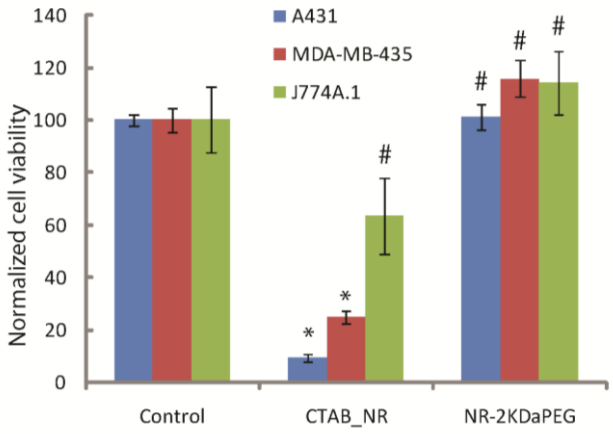

Figure 2.7 Cytotoxicity of as-prepared CTAB-coated and 2 kDa mPEG-thiol coated nanorods in different cell lines. The y-axis shows normalized cell viability. The viability of control samples is normalized to 100. Values statistically different ($p < 0.05$) from controls are labeled by *; values that do not show statistically significant difference from controls ($p > 0.05$) are labeled by #.

Molecular specificity of the antibody-conjugated nanorods was evaluated in two cell lines: EGFR-positive A431 and EGFR-negative MDA-MB-435 cells. Molecular-specific nanorods were conjugated with anti-EGFR clone 225 antibodies. Nanorods conjugated with non-specific clone RG-16 antibodies were used as control. Figure 2.8 shows dark-field and transmittance hyperspectral images of labeled cells and controls. Only EGFR-positive A431 cells labeled with anti-EGFR nanorods show distinct spectral signatures in the 500-800 nm range, which corresponds to gold nanorods. There is no detectable difference between unlabeled cells and both the EGFR-positive A431 cells labeled with non-targeted RG-16 conjugated nanorods and the EGFR-negative MDA-MD-435 cells labeled with anti-EGFR nanorods. Conjugates of nanorods with fluorescently labeled anti-EGFR antibodies were also used to label both EGFR-positive and EGFR-negative cell lines; strong fluorescent signal was observed only from labeled EGFR-positive A431 cells (Figure 2.9). These results demonstrate molecular specificity of gold nanorods conjugated with anti-EGFR antibodies.

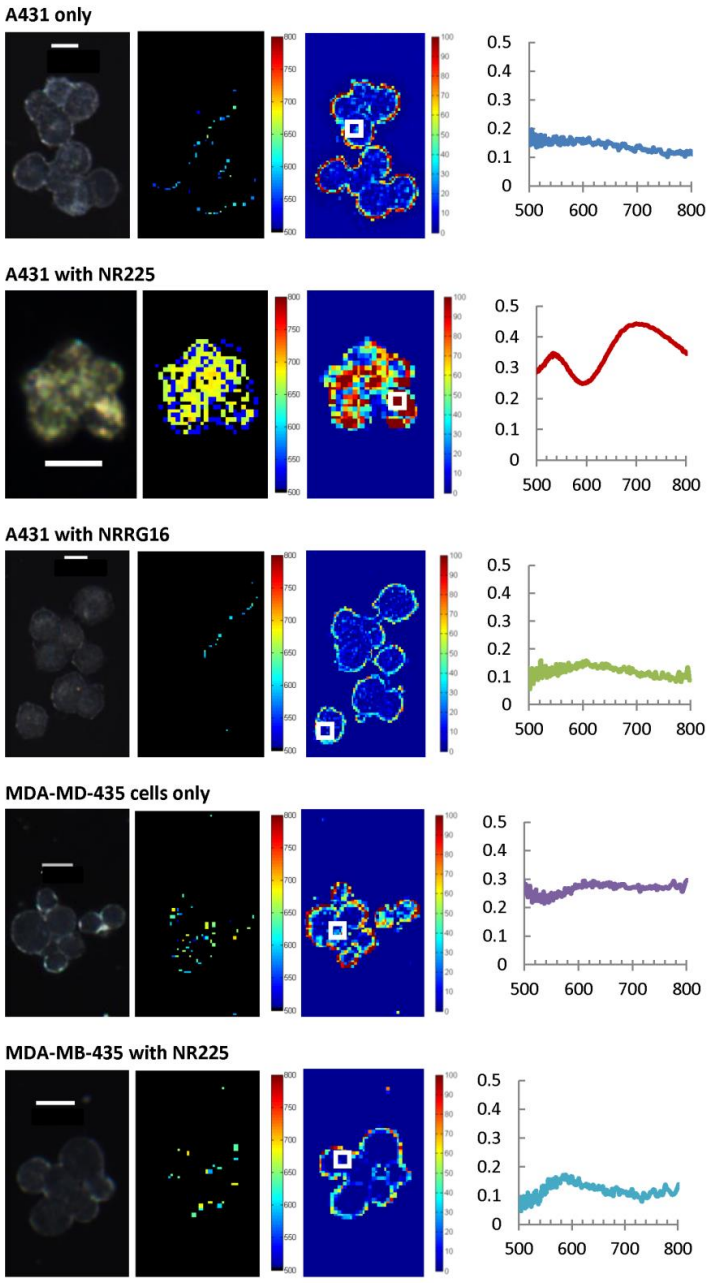

Figure 2.8 Optical characterization of molecular specificity of antibody conjugated gold nanorods in cell cultures. Columns from left to right: dark-field transmittance images; transmittance hyperspectral images with color-coded peak wavelength in 500 - 800 nm spectral region; transmittance hyperspectral images with color-coded integrated absorbance in the 500 - 800 nm region; absorbance spectra integrated over the regions highlighted by white squares in the previous column.

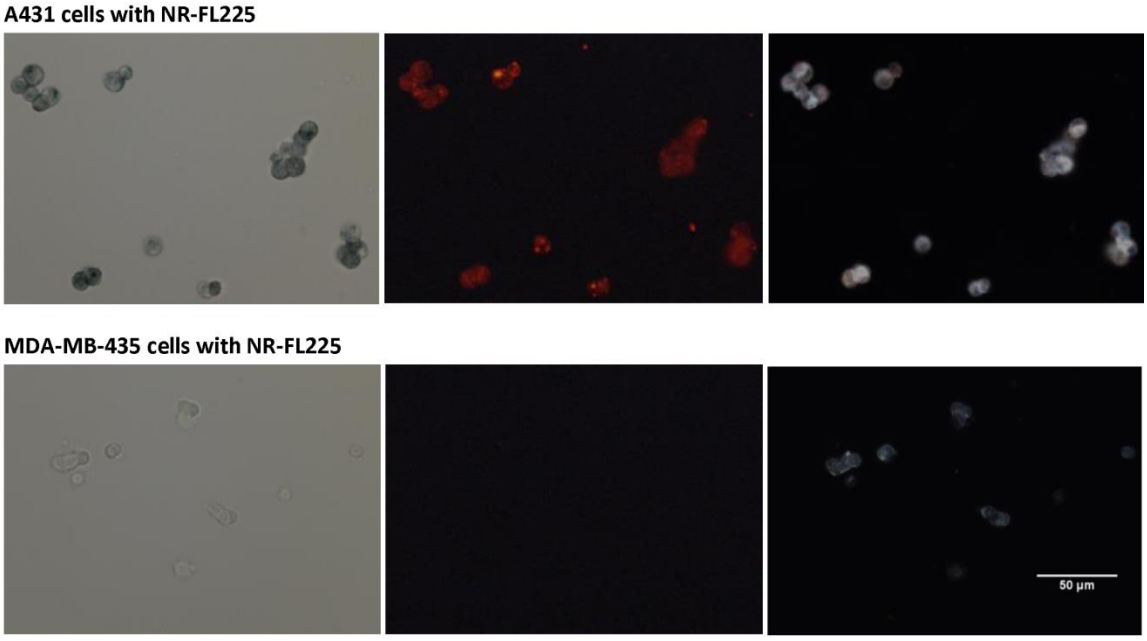

Figure 2.9 Right – Bright field images; middle – fluorescent images; left – dark-field images of A431 EGFR(+) (top row) and MDA-MB-435 EGFR(-) (bottom row) cells labeled using nanorods conjugated with fluorescently labeled clone 225 (anti-EGFR) antibody. Scale bar = 50 µm.

Bright-field transmittance images of A431 cells labeled with molecular-specific nanorods appear dark compared to unlabeled cells due to light absorption by gold nanorods (Figure 2.9). Analysis of dark-field transmittance and hyperspectral transmittance images revealed strong absorbance around 700 nm throughout labeled cells. The absorbance spectra of nanorods-labeled cells is broadened with the full width at half maximum of 150 ± 7.6 nm compared to 107 ± 4.6 nm for conjugated nanorods in suspension. In addition, the T-to-L peak ratio increases by 52 ± 21.31 % relative to isolated nanorods. These optical changes can be attributed to EGF receptor mediated aggregation of nanorods. The same effect has been observed and thoroughly characterized by our group in the case of EGFR targeted spherical plasmonic nanoparticles. [158, 179, 222]

It is of interest to note that there is a perception of an increased absorption at cellular boundaries in hyperspectral transmittance images (Figure 2.8). This effect is due to light diffraction at the interface between cells and the surrounding medium. However, these boundary regions in control samples do not exhibit spectral signatures of gold nanorods.

EGFR-positive A431 cells labeled with anti-EGFR nanorods exhibit strong contrast in photoacoustic imaging (Figure 2.10). Multi wavelength photoacoustic imaging was used to obtain spectral characteristics of the labeled cell. The intensity of the photoacoustic signal decreases as a function of wavelength in the 700-800 nm wavelength region; this behavior is in good agreement with extinction spectra of the labeled cells (Figure 2.8, second row, and Figure 2.10). Note that gold nanorods with extinction maximum at 700 nm were used in these imaging experiments. As expected, the unlabeled A431 cells did not produce any photoacoustic signal.

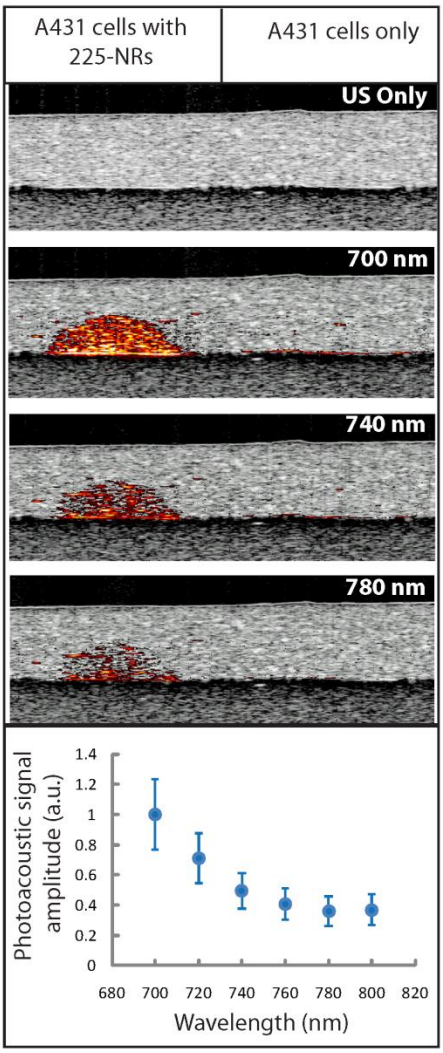

Figure 2.10 Combined ultrasound (US) and photoacoustic (PA) images of tissue-mimicking cell phantoms. The phantom on the left consists of A431 cells labeled with anti-EGFR gold nanorods and the phantom on the right has unlabeled A431 cells. The plot at the bottom shows PA signal intensity integrated over the phantom area as a function of excitation wavelength.

2.4 DISCUSSION

Directional conjugation involves obtaining a high level of control over an orientation of a biomolecule on nanoparticle surface. Orientation is particularly important in the conjugation of antibodies to the particle surface as many potential orientations of the antibody lead to a loss of antibody binding function, but in general, orientation is also quite important for other proteins and molecules. Directional conjugation can be accomplished for molecules that have uniquely accessible functional groups. In the case of antibodies, one such functional group is the carbohydrate moiety located on the heavy chain of most antibodies. It was previously demonstrated that periodate-mediated oxidation of the carbohydrate group located on the Fc- region of an antibody to an aldehyde can be used for oriented conjugation of monoclonal antibodies to an immunopurification matrix containing hydrazide functional groups; the resulting matrix yielded the antigen-binding activity close to the theoretical value of 2 moles of bound antigens per one mole of a conjugated antibody. [211] In this study, a heterofunctional linker with hydrazide and dithiol groups on opposing ends of the molecule was used to achieve directional conjugation of antibodies to gold nanorods. The hydrazide moiety interacts with the aldehyde on the antibody and the dithiol enables conjugation directly to the gold surface.[210] It is important to note that linkers with two adjacent sulfhydryl groups such as thioctic acid provide greater stability as compared to a single sulfhydryl group.[217] It has been shown that molecules conjugated using single sulfhydryl-containing linkers can be replaced in biological environment by an excess of naturally present sulfhydryl-containing biomolecules such as glutathione.[194]

Previously published methods of synthesis of gold nanorod bioconjugates have several downsides including lower *in vivo* stability of bioconjugates produced by electrostatic interactions, cytotoxicity due to presence of CTAB in final nanorods conjugates and lack of control over antibody orientation during conjugation. In addition,

most literature reports provide insufficient characterization of prepared conjugates that renders assessment of the quality of nanorod conjugate difficult.

Important information pertaining to the aggregation state and stability of nanorod conjugates can be obtained from nanorods extinction spectra before and after conjugation. For example, percentage change in the transverse to longitudinal (T-to-L) peak ratio is one spectral parameter that can be used in evaluation and comparison of nanorod conjugation approaches; other parameters include spectral shift and full-width at half maximum of the longitudinal peak. In addition, zeta potential measurements can provide insight into changes of surface composition during conjugation reaction steps. Unfortunately, most previously published reports do not include analyses of nanorod extinction spectra before and after conjugation with antibodies. The importance of this characterization can be illustrated using an example from a recently published conjugation approach where bioconjugated nanorods were prepared by, first, replacing the CTAB layer with 11-mercapto undecanoic acid (MUDA) and then attaching antibody fragments through primary amino groups to the carboxylic acid groups of MUDA using EDC chemistry. [88] Nanorods with geometrical aspect ratios 2.3 and 3.5 showed approximately 64.7% and 23.5% increase in the T-to-L peak ratio after CTAB replacement with MUDA, respectively, as calculated from the published spectra. These changes indicate potential aggregation of nanorods during the conjugation procedure. In contrast, molecular-specific nanorods synthesized using the technique reported here undergo increase in the mean value of T-to-L peak ratio of less than 9 % (Table 2). In addition, there are no changes in full-width at half maximum of the longitudinal peak during conjugation procedure or after antibody conjugation.

2.5 SUMMARY

In this study, we have developed a robust conjugation technique for reproducible synthesis of molecular-specific gold nanorods and have fully characterized conjugates using zeta potential, extinction spectra, electron microscopy and hyperspectral optical imaging. Furthermore, the nanorod bioconjugates were prepared by attaching the Fc portion of antibodies to the nanorod surface that has two important advantages: first, directional attachment of antibodies through non-binding Fc moieties provides maximum possible binding efficiency of the conjugates; second, since the Fc moieties in the conjugates are oriented towards nanorod surface, they are not available for interaction with Fc receptors that are present in some human cells including macrophages, providing longer residence time and diminishing potential immunogenicity during *in vivo* applications. Molecular-specific gold nanorods synthetized here could be used to image cancer cells using optical and photoacoustic imaging. Additionally, we observed characteristic changes in optical spectra of molecular targeted nanorods after their uptake by cancer cells; the observed spectral signatures can be explored for sensitive detection of interactions between molecular-specific nanoparticles and cells.

Chapter 3: Near-IR Contrast Agents for Immune Cell Tracking‡

3.1 INTRODUCTION

Tracking of immune cells is essential to understand the regulatory role of immune cells in pathological conditions such as cancer and cardiovascular diseases[223] that can lead to development of novel therapeutic approaches. [224, 225] Moreover, using immune cells as transport vehicles for imaging and therapeutic agents can facilitate imaging and treatment of cancer cells in vasculature inaccessible areas. Indeed, one of major barriers in cancer treatment is inaccessibility of avascular necrotic core of a tumor by traditional drugs. Cancer cells from these hypoxic regions can survive therapy and migrate to secondary sites causing cancer metastasis.[226, 227] Immune cells can penetrate the tumor necrotic core by following chemokines released by cancer cells that can be used as a strategy to deliver a therapeutic payload.[228, 229] Optimization of these new approaches to treatment of cancer and other diseases requires development of sensitive imaging methods for *in vivo* tracking of immune cells.

A direct approach to immune cell tracking is to load cells with contrast agents that are suitable for *in vivo* imaging. Recently, we have demonstrated that loading gold nanoparticles into endosomal compartments of stem cells does not alter cellular functions including cell viability and differentiation. [230] Furthermore, we have demonstrated that stem cells labeled with gold nanoparticles can be tracked *in vivo* using combined photoacoustic (PA) and ultrasound (US) imaging with penetration depth of several centimeters.[231] In PA imaging, the tissue is irradiated with nanosecond pulses of low energy laser light. Then, through the processes of optical absorption followed by thermal

‡ Adapted with permission from P. P. Joshi, S. J. Yoon, Y.-S. Chen, S. Y. Emelianov, K.V. Sokolov Biomed. Opt. Express, 2013, 4(11), 2609-18. Copyright 2013 The Optical Society. Contribution of the coauthors – S. J. Yoon performed photoacoustic imaging of the phantom, Y.-S. Chen helped in optimizing silica coating procedure of the nanorods, S.Y. Emelianov supervised imaging part of the paper, K. V. Sokolov provided overall supervision of the research.

expansion, broadband acoustic waves are generated within the irradiated volume. Using an ultrasound detector, these waves can be detected and spatially resolved to provide an image. Furthermore, the PA imaging can be augmented by US imaging – these systems are complementary since both PA and US imaging systems can utilize the same ultrasound sensor and associated receiver electronics.[92, 232, 233]

Gold nanoparticles, including nanospheres,[63, 64, 158, 166, 181, 234-236] nanoshells,[66-69] nanocages,[17, 70-72] and nanorods[20, 74-77, 89, 115, 217, 237] are of increasing interest to biomedical engineers due to their biocompatibility, facile surface modification and high optical cross sections that can provide strong signal in imaging modalities based on optical contrast. The optical properties of gold nanoparticles can be modulated by changing their size and shape. For example, plasmon resonance of gold nanorods is easily tuned in the red to near infrared (NIR) spectral region by changing their aspect ratio,[78] facilitating simultaneous imaging of multiple biomarkers. [76, 88] Strong NIR extinction cross-sections of nanorods have been used for two-photon luminescence [74, 89] and photoacoustic [90, 91, 92 , 238] imaging of thick biological samples as well as for photothermal destruction of cancer cells. [93-95, 239] Thus, anisotropic gold nanorods provide a convenient combination of properties for biomedical applications including the possibility of cell tracking using PA imaging.[85-87] However, the optical absorbance spectra of gold nanorods broaden when they interact with live cells.[115] This effect is due to plasmon resonance coupling of closely spaced nanoparticles upon cellular uptake and it diminishes the ability to simultaneously image multiple cell populations labeled with different nanorods. In addition, recent reports showed that cells more readily uptake spherical nanoparticles as compared to rod-shaped particles.[240] As spherical nanoparticles do not have the desired near infrared absorption necessary for *in vivo* imaging, increasing cellular uptake of nanorods is desirable.

Here we synthetized silica-coated gold nanorods to address challenges associated with the use of rod-shaped gold nanoparticles in cell tracking. Silica coating changes shape of the gold nanorods from cylindrical to spheroidal. We demonstrated that the silica-shell reduces plasmon resonance coupling between nanorods upon uptake by cells and, thus, can facilitate multiplex imaging using nanorods. In addition, the silica shell was doped with fluorescent dyes to enable multimodal imaging with fluorescence and PA imaging modalities. This combination enables in-depth *in vivo* imaging of labeled cells using photoacoustics followed by high-resolution *ex vivo* fluorescence imaging for validation and detailed characterization of *in vivo* imaging data.

3.2 Research Approach

3.2.1 Materials and Methods

Chemicals: $AgNO_3$ (Acros Organics, 41936), $HAuCl_4$ (Sigma, 520918), CTAB (Amresco, 0833), ascorbic acid (Acros Organics, 401471000), $NaBH_4$ (Fisher, S678), methoxy-PEG-thiol (5 KDa, Creative PEGworks, PLS-605), Rhodamine B isothiocyanate (Aldrich, 283924), [3-(2-Aminoethylamino)propyl]trimethoxysilane (AEAPTMS, Aldrich, 104884), tetraethylorthosilicate (TEOS, Aldrich, 333859), ammonium hydroxide (NH_4OH, Fisher, A669S), Oxazine 725 (Exciton, 07250), Polystyrene sulfonate Na salt (18 KDa, Polysciences, 16250), Poly(allylamine hydrochloride) (15 KDa, Aldrich, 283215), 3-(4,5-dimethylthiazol-2-yl)-5-(3-carboxymethoxyphenyl)-2-(4-sulfophenyl)-2H-tetrazolium (MTS, Promega, G111B) and phenazine methosulfate (PMS, Sigma, P9625) were used as received.

Synthesis of PEG-coated gold nanorods (mPEG-NRs): Gold nanorods (NRs) were synthesized by seed-mediated growth mechanism using the previously published protocol [202]. As-prepared nanorods were washed twice in water by centrifugation at 18000g for 45 minutes. The final NRs pellet was dispersed in water and stored at room temperature at optical density (OD) of 15. Before silica-coating, the cetyl trimethyl ammonium bromide (CTAB) layers on NRs were replaced with methoxy-PEG-thiol (mPEG-SH). One milliliter of 1 mg/mL mPEG-SH (5kDa) in water was mixed with 1 mL of CTAB-NRs (OD 15) and sonicated using a water bath sonicator (Branson 1510R-MT) for 1 minute at room temperature. After sonication, the NRs were stirred overnight in the presence of mPEG-SH to complete replacement of CTAB with mPEG-SH. Free CTAB and mPEG-SH molecules were removed by centrifugation through 100kDa centrifugal filters at 2500g for 15 minutes. Then, the NRs were washed one more time in water to remove any residual free mPEG-SH and CTAB. mPEG-NRs were dispersed in 1 mL water and stored at room temperature.

Synthesis of silica-coated gold nanorods: We used two approaches to synthesize fluorescent silica-coated gold nanorods: 1) encapsulation of a fluorescent dye within silica matrix, and 2) covalent attachment of a fluorescent dye to the silica matrix (Figure 3.1). Silica shell of a controlled thickness was deposited on PEG-coated nanorods using a modified Stöber method[241]. One milliliter of mPEG-NRs (OD 15) was mixed with 1.5 mL of isopropanol. The solution was continuously stirred while adding 0.6 mL of 3 vol % tetraethylorthosilicate (TEOS) and 0.625 mL of 3.84 vol % ammonium hydroxide (NH_4OH). To the reaction mixture, 40 µL of fluorescent dye, Oxazine 725, solution (11.5 mg/mL) was directly added to synthesize Oxazine-doped silica-coated nanorods (OxSilicaNRs)[242]. Rhodamine (Rh) dye-doped silica-coated nanorods (RhSilicaNRs)

were synthesized by first covalently attaching Rh isothiocyanate dye to [3-(2-Aminoethylamino)propyl]trimethoxysilane (AEAPTMS)[243]. Briefly, 15 µL of AEAPTMS was stirred with 10 mg Rhodamine B isothiocyanate in 2.5 mL of anhydrous isopropanol (IPA) for 48 hours under nitrogen. This solution was five times diluted in anhydrous IPA before adding to the nanorods. One milliliter of mPEG-NRs (OD 15) was mixed with 1.5 mL of isopropanol. The solution was continuously stirred while adding 0.6 mL of 3 vol % TEOS and 0.625 mL of 3.84 vol % NH_4OH. After 30 minutes, four aliquots (12.5 µL each) of the diluted Rhodamine-AEAPTMS solution were added to the reaction mixture (TEOS:Rh-AEAPTMS molar ratio 1080:1). The aliquots were separated by 10 minutes time interval. After 2 hours of stirring at room temperature, the silica-coated nanorods were collected by centrifugation at 700g for 15 minutes using 100 kDa MWCO centrifugal filters. Both OxSilicaNRs and RhSilicaNRs were washed three times with water before use.

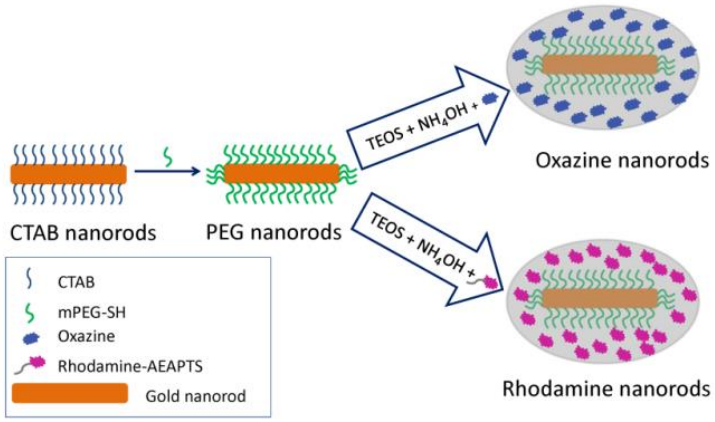

Figure 3.1 Schematic of two approaches used to synthesize fluorescent silica-coated nanorods.

Synthesis of polymer-coated nanorods*:* Polymer-coated nanorods were synthesized by mixing 1 mL of CTAB-coated gold nanorods (OD 10) with 1 mL of polystyrene sulfonate (PSS) solution (10 mg PSS per 1 mL of 1 mM NaCl) [89, 220]. The solution was kept on a shaker for 30 minutes and then centrifuged at 18000g for 15 minutes. The nanorods containing pellet was redispersed in 1 mL of 1 mM NaCl solution and was mixed with 1 mL of PSS solution. The solution was placed on a shaker for 30 minutes and then centrifuged to collect the nanorods coated with PSS. The PSS-nanorods were coated with Poly(allylamine hydrochloride) (PAH) using the same procedure. PSS-nanorods pellet was dispersed in a 1 mL NaCl solution (1 mM) and mixed with 1 mL of PAH solution (10 mg PAH per mL of 1 mM NaCl). After 30 minutes of shaking, the nanorods pellet was collected using centrifugation and dispersed in a salt solution. The PAH coating procedure was repeated once more to obtain PAH-PSS-nanorods. The final nanorods pellet was dispersed in 1 mM NaCl solution.

Cell viability study*:* The viability test of monocyte/macrophage (RAW 264.7) cells was performed after incubating the cells with OXSilicaNRs or RhSilicaNRs at a given concentration in phenol-free DMEM cell culture media for 18 hours at 37°C. As the nanorods-loaded cells need to be viable for a long period for successful cell tracking application, extended cell viability tests were performed by culturing cells in regular cell culture media for an additional 24 to 48 hours after incubation of cells with silica-coated nanorods. To perform cell viability study, the cells were washed once with PBS and a background absorbance was measured at 490 nm using BioTek Synergy HT UV-Vis spectrophotometer. Then MTS reagent (mixture of MTS and PMS prepared in phenol free cell culture media) was added to the cells. After 3 hours of incubation with MTS reagent

solution, absorbance at 490 nm was measured again. Background absorbance was subtracted in order to determine the number of metabolically active live cells in a sample.

Two mouse-macrophage cell lines, RAW 264.7 and P388D1, were used for cell labeling and characterization throughout this study. While RAW 264.7 cells are highly phagocytic macrophage cells, P388D1 cells have an inferior phagocytic activity [244, 245]. In order to achieve comparable loading of nanorods in both cell lines, we used higher dosage of nanorods for P388D1 cells ($1x10^7$ NRs/cell) compared to RAW 264.7 cells ($7x10^4$ NRs/cell). The cells were incubated with nanorods for 18 hours at 37°C in cell culture media. Labeled cells were washed with cell culture media to remove any unbound nanorods and re-suspended in phenol free media to measure absorbance. Absorbance spectra of unlabeled cells were subtracted from the spectra of nanorod-loaded cells to obtain the contribution from nanorods. Before the measurements, cells were counted using a standard hemocytometer in the presence of trypan blue. Trypan blue is a vital stain that selectively colors dead and lysed cells. More than 95% of cells were vital during the absorption measurements based on trypan blue staining.

Tissue mimicking phantom preparation*:* Gelatin based tissue-mimicking phantoms with cell inclusions were fabricated for combined photoacoustic and ultrasound imaging. To simulate tissue background, 8wt% gelatin solution with 0.2wt% of 15 μm silica particles was used to prepare the base and the top layers which encapsulated the cell inclusions. Suspensions of P388D1 cells only and P388D1 cells loaded with RhSilicaNRs were mixed with the same volume of 16wt% gelatin solution at 37^{o}C. Specifically, five inclusions of P388D1 cells loaded with RhSilicaNRs were prepared with cells concentrations 5×10^6, 2.5×10^6, 1.25×10^6, 2.5×10^5, and 1.25×10^5 cells/mL. For the inclusion with only cells, 5×10^6 cells/mL cell concentration was used. The phantoms with only silica-coated

nanorods were prepared using the given concentration of nanorods per inclusion. For phantom preparation, suspension of silica particles in gelatin at 37^{o}C was poured in a petri dish and was cooled down at 4^{o}C. During the cool down step, some silica particles settle down resulting in reduced ultrasound contrast in the top part of the phantom. Then, suspensions of cells in gelatin were placed on the solidified base layer and were allowed cool down. Finally, the top layer of gelatin/silica particles was added to complete the phantom.

Animal studies: All animal work performed for this study was approved under IACUC protocol AUP-2009-00090. Mice were subcutaneously inoculated with A431 cells and the tumor was allowed to grow to about seven millimeter in size. The mice were then imaged before the injection of control cells or cells loaded with either gold nanospheres or RhSilicaNRs. Noninvasive longitudinal imaging was performed up to 48 hours post-injection using combined ultrasound and photoacoustic imaging.

Photoacoustic imaging set-up*:* Photoacoustic imaging of the tissue-mimicking phatom was performed using a Vevo® 2100 LAZR imaging system (VisualSonics, Inc., Toronto, Canada) and an array ultrasound transducer (LZ250, VisualSonics, Inc.) operating at 20 MHz center frequency. A laser beam with 5 ns pulses and 20 Hz repetition rate was generated by a tunable OPO laser system pumped by Nd:YAG laser. The wavelength of the laser in the phantom imaging experiment was matched to the peak optical absorption wavelength of the silica-coated nanorods, which is 780 nm. The laser beam was delivered through an optical fiber bundle integrated with the ultrasound array transducer. A mechanical system was used to translate the transducer in steps of 114 μm to allow for collecting multiple cross-sectional images of the inclusions using combined US and PA

imaging. In order to perform a quantitative photoacoustic signal comparision between each inclusion, fluence of the laser was maintained at 10 mJ/cm^2, which is below the damage threshold for silica-coated nanorods [241]. To compensate the PA signal amplitude for laser fluctuations, laser fluence was recorded by the VEVO 2100 LAZR imaging system during PA imaging and PA signals were normalized by laser fluence in post-processing. PA signal intensity of each inclusion was measured by averaging PA signals from 11 different cross-sectional images of the inclusion.

3.3 Results and Discussion

The RhSilicaNRs and OXSilicaNRs were characterized using TEM and fluorescence emission. Transmission electron microscopy shows a uniform silica layer on the silica-coated nanorods after both syntheses (Figure 3.2). Fluorescence emission spectra of RhSilicaNRs and OXSilicaNRs indicate successful encapsulation of fluorescent dyes in the silica-coated nanorods (Figure 3.2).

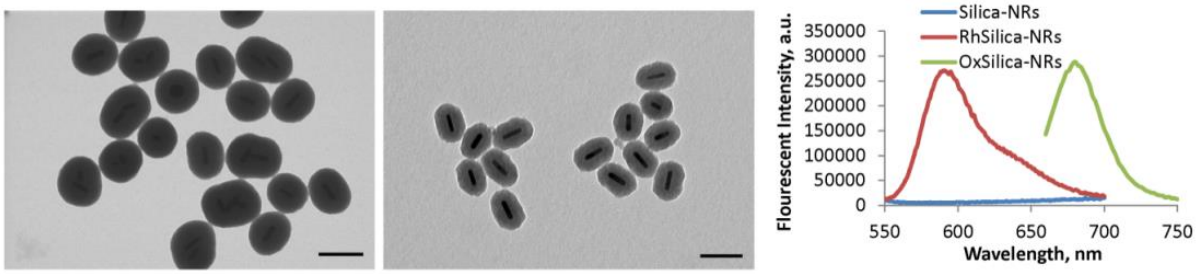

Figure 3.2 Transmission Electron Microscopy of Oxazine silica-coated nanorods (OxSilicaNRs) (left) and Rhodamine silica-coated nanorods (RhSilicaNRs) (middle), scale bar: 100 nm; fluorescence emission spectra of OxSilicaNRs (ex 645 nm), RhSilicaNRs (ex 540 nm) and plain silica coated nanorods (SilicaNRs) (right).

Cellular tracking requires long-term viability of the nanoparticle-loaded cells. Here we used monocyte macrophage cell line (Raw 264.7) to evaluate extended viability of cells loaded with silica-coated flourescent nanorods following an 18 hours incubation (Figure 3.3). The nanorod-loaded macrophages were grown in fresh cell cuture media for 24 and 48 hours before testing cell viability. OxSilicaNRs showed no toxicity right after the incubation step; however, significant cell death was observed during subsequent cell culture (Figure 3.3 (a)). In contrast, RhSilicaNRs did not cause any post-incubation long-term toxicity (Figure 3.3 (b)). The toxicity of OxSilicaNRs can be attributed to non-covalent attachment of the Oxazine dye to the silica matrix that may result in leakage of the dye within the cells over a long period of time leading to the long-term toxicity. A slight decrease in viability of cells loaded with mPEG-NRs after 24 hours culture can be attributed to a small amount of residual CTAB molecules which are present after ligand exchange with mPEG-SH [115]. Because of the lack of cytotoxicity, RhSilicaNRs were used to characterize cellular uptake and to perform fluorescence and photoacoustic imaging experiments.

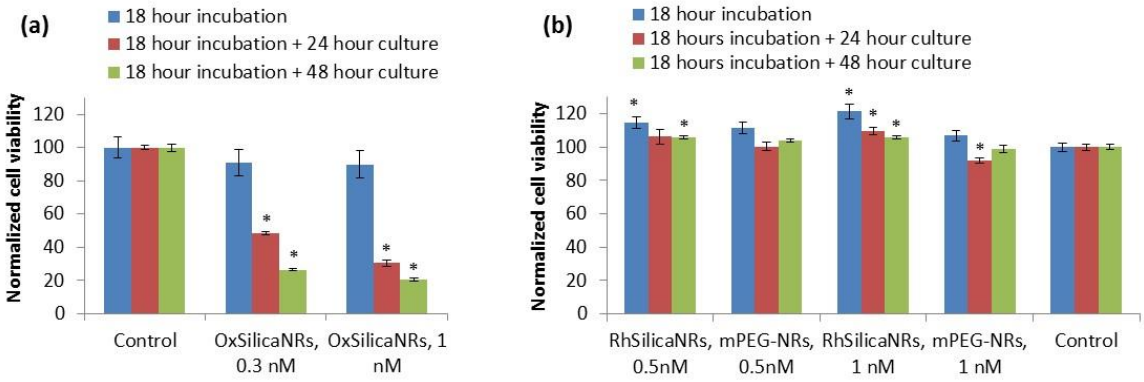

Figure 3.3 Viability of mouse monocyte macrophage cell line (Raw 264.7) loaded with either OxSilicaNRs (a) or mPEG-NRs and RhSilicaNRs (b) immediately after 18 hrs of incubation with nanoparticles and 24 or 48 hours of cell culture in fresh media after nanorod-loading. RhilicaNRs show no toxicity during extended cell culture of labeled cells, whereas OxSilicaNRs exhibit significant cytotoxicity. Statistically different results compared to controls using student t-test (p-value < 0.01) are identified by *.

Silica-coated nanorods exhibit negligible changes in the longitudinal peak position and the full-width at half-maximum (FWHM) values after uptake by two macrophage cells lines - RAW 264.7 and P388D1 (Figure 3.4 (a), (b) and Table 3.1). In contrast, nanorods coated using layer-by-layer deposition of polystyrene sulfonate (PSS) and poly(allylamine hydrochloride) (PAH) polymers [246] show significant change in the optical absorption upon cellular uptake (Figure 3.4 (c), Table 3.1). Note that RhSilicaNRs, SilicaNRs and PAH-PSS-NRs have different longitudinal peak maxima. These results demonstrate that silica coating of *ca.* 30 nm provides sufficient spacing to prevent plasmon resonance coupling of nanorods after they are uptaken by live cells. Since silica-coated gold nanorods do not change optical spectra inside cells, we used extinction coefficients of the nanorods in suspension to determine nanorod loading of cells. RAW 264.7 and P388D1 cells accumulated *ca.* 10^4 and $2x10^4$ silica-coated nanorods per cell, respectively. Cells loaded

with RhSilicaNRs can be readily viasualized using fluorescence imaging (Figure 3.5 (e), (f)). Negligible nanorod-specific contrast was observed in the dark-field images of RhSilicaNRs-loaded cells due to low sensitivity of our optical microscope to NIR logitudinal resonances of the nanorods used in this study (Figure 3.5 (b), (c)). Thus, fluorescence imaging provides a convenient way of identifying cells labeled with dye-dopped silica-coated gold nanorods.

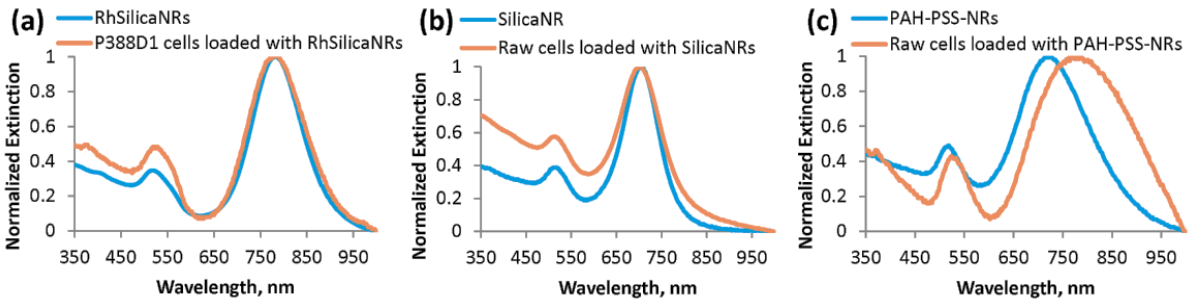

Figure 3.4 Extinction spectra of: (a) RhSilicaNRs in suspension and P388D1 cells loaded with RhSilicaNRs; (b) SilicaNRs in suspension and RAW 264.7 cells loaded with SilicaNRs; (c) polymer-coated nanorods (PAH-PSS-NRs) in suspension and RAW 264.7 cells loaded with PAH-PSS-NRs. Longitudinal peak position and extinction spectra of silica-coated nanorods do not undergo significant changes after cell uptake in contrast to polymer-coated NRs.

	FWHM, nm	% Increase in FWHM	Longitudinal Peak Wavelength, nm
RhSilicaNRs	120		782
P388D1 cells with RhSilicaNRs	138	15.00%	778
SilicaNRs	83		704
RAW 264.7 cells with SilicaNRs	87	4.82%	700
PAH-PSS-NRs	139		725
RAW 264.7 cells with PAH-PSS-NRs	222	59.71%	800

Table 3.1 Characterization of the absorbance spectra of nanorods and cells-loaded with nanorods; FMHM – full-width at half maximum.

Previous literature reports have shown good contrast in dark-field imaging of gold nanorods with a longitudinal peak in the visible range [247, 248]. It has been also reported by us [115] and other groups [93, 199, 249] that cells loaded or labeled with gold nanorods coated by a thin layer of organic ligands and targeting biomolecules produce detectable contrast in dark-field images as compared to unlabeled cells. We attribute this contrast to plasmon resonance coupling between closely spaced nanoparticles in the cellular endosomes that results in an overall increase in scattering in the visible region. In the present study, silica coating around nanorods significantly diminishes the effect of plasmon resonance coupling as described above and, therefore, silica-coated nanorods do not provide significant contrast in the presence of endogenous scattering background from the cells.

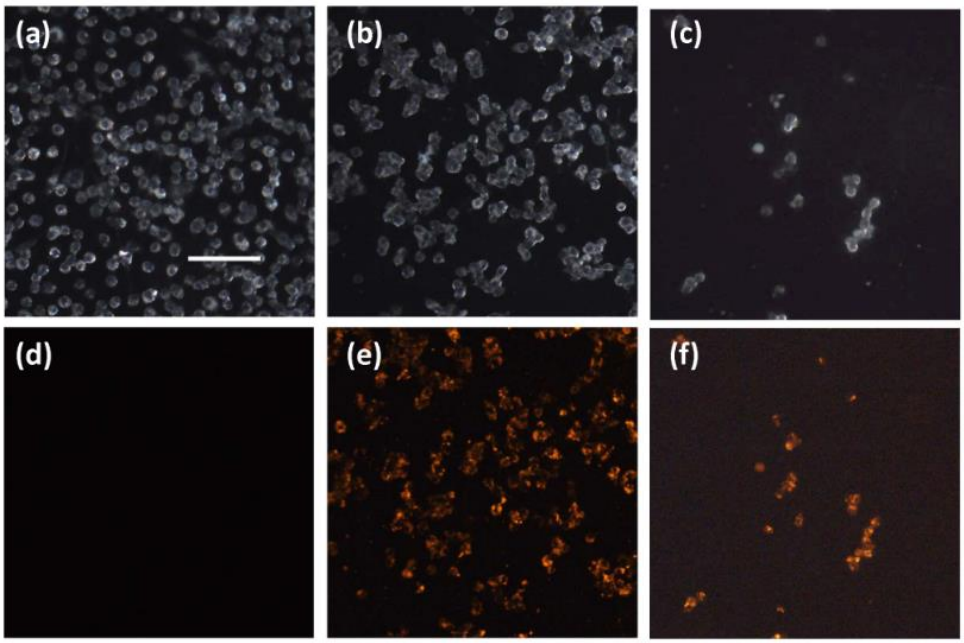

Figure 3.5 Dark-field (a, b, c) and fluorescence (d, e, f) images of RAW 264.7 cells alone (a, d), RAW 264.7 cells loaded with RhSilicaNRs (b, e), and P388D1 cells loaded with RhSilicaNRs (c, f). Scale bar = 50 μm. Images were acquired with Leica DM600 upright microscope using 20x 0.5 NA objective. Fluorescence imaging was performed using Cy3 filter cube, ex/em 555/590 nm.

Having successfully loaded cells with the silica-coated nanorods, the next step was to evaluate feasibility of sensitive detection of the nanorod-loaded cells using PA imaging. To this end, inclusions containing different concentrations of P388D1 cells loaded with RhSilicaNRs were incorporated in the tissue-mimicking phantoms and multiple cross-sectional PA images of each inclusion were collected at 780 nm wavelength, which corresponds to the longitudinal plasmon resonance peak of the nanorods (Figure 3.6). Although the same matrix was used to prepare the top and bottom layers of the phantom, settlement of silica particles in the bottom layer of the phantom results in a decreased US contrast at the boundary between the top and the bottom layers (approximately in the

middle of the images on Figure 3.6 (a). PA signal intenstiy showed linear behaviour as a function of concentration of labeled cells (the R^2 value for the linear regression fit is 0.9753). From the linear regression fit in Figure 3.6 (b), we determined that the PA imaging can detect *ca.* 1.25 x 10^6 cells evenly dispersed in a 1 cm^3 volume. After taking into account the imaging kernel size of the photoacoustic system (approximately 160 μm x 110 μm x 220 μm), we calculated that PA imaging could detect as few as five nanorod-loaded cells per imaging kernel. Because the current threshold for clinical detection is about 10^9 cells growing as a single mass as depicted in the Figure 3.7, the enhancement in the detection limit offered by the use of silica-coated gold nanorods in photoacoustic imaging is noteworthy.

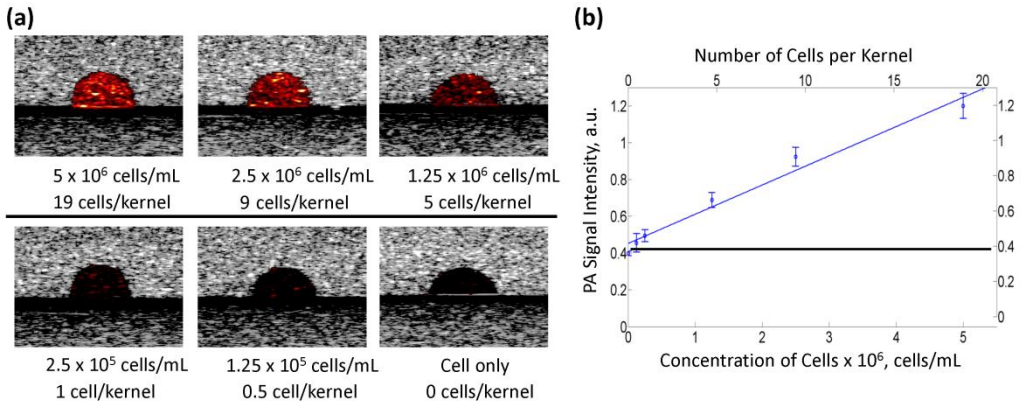

Figure 3.6 Photoacoustic images of tissue-mimicking phantoms prepared with different concentrations of P388D1 cells loaded with Rh-Silica-NRs (a). Each image covers a 6.3 x 8.8 mm field of view. Dependence of the PA signal amplitudes on the concentration of nanorod-loaded cells at 780 nm excitation wavelength (b); the top horizontal axis shows a number of cells per imaging kernel of the photoacoustic system used. The solid blue line represents the linear regression fit of the data and the black line shows the noise level in the PA imaging (b).

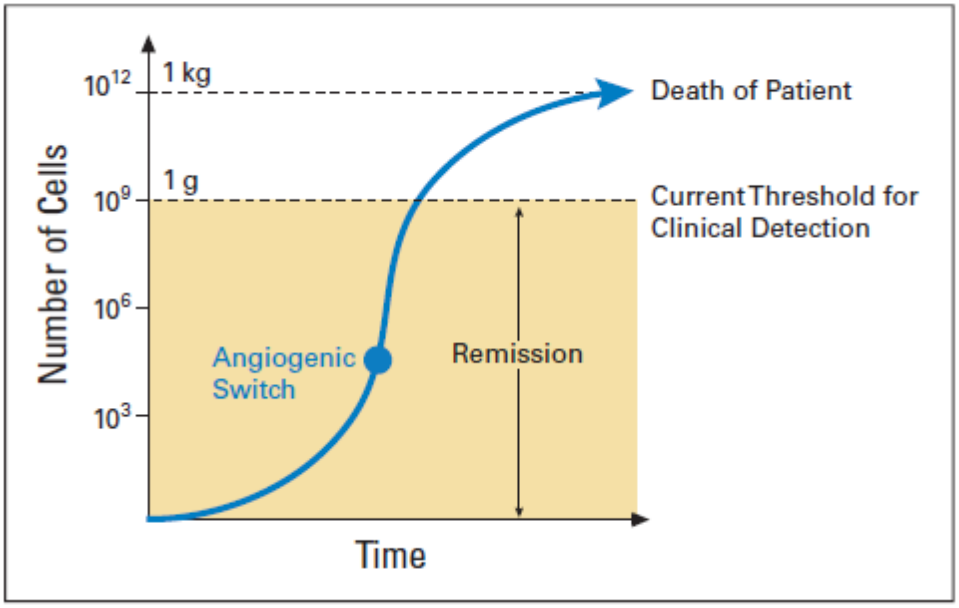

Figure 3.7 Gompertzian growth curve of a solid tumor and its relationship to cancer detection and imaging. Number of malignant cells (ordinate) as a function of time (abscissa). The transition from first lag to log phase of growth, associated with the transition from diffusion-limited nutrition to neovascularization, is labeled "angiogenic switch." Remission is shown as the uncertainty of cell number ranging from zero to the current clinical threshold for cancer detection (approximately 10^9 cells growing as a single mass). Reprinted with permission from ref [14].

One of the concerns while using cells labeled with exogenous contrast agents as described in this study is the possibility of imaging the label –gold nanorods – instead of tracking the cells labeled with gold nanorods. To this end, we have prepared tissue-mimicking phantoms with different concentrations of RhSilicaNRs to evaluate the sensitivity of detecting nanorods by themselves (Figure 3.8). We found that even with very high concentrations of RhSilicaNRs (10^{13} NRs/mL), we cannot obtain much contrast using PA imaging. This concentration corresponds to $2x10^7$ RhSilicaNRs per imaging kernel compared to the detection limit of 10^5 RhSilicaNRs when they are within the cells. The

effect of PA signal enahncement upon aggregation of silica-coated nanoparticles is also previously observed by our group.[250] Clearly, we have not only achieved high sensitivity for cell tracking, but also significantly reduced the potential background signal arising from the nanoparticles outside the cells.

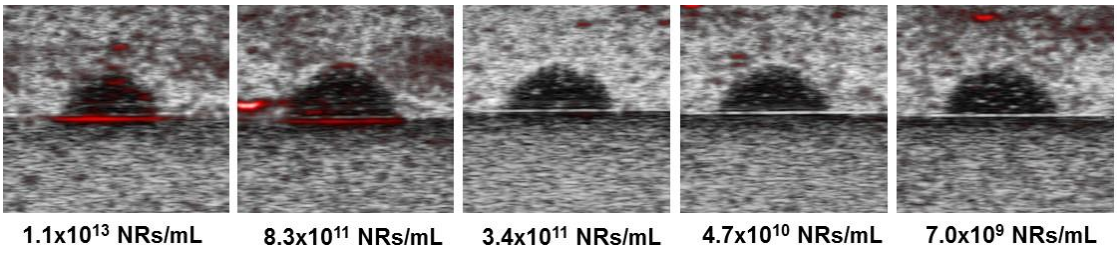

Figure 3.8 Photoacoustic images of tissue-mimicking phantoms prepared with different concentrations of RhSilicaNRs. Imaging was performed at the longitudinal peak wavelength of nanorods.

An exploratory *in vivo* study was performed to image infiltration of gold nanoparticles-loaded macrophages in a solid tumor using photoacoustic imaging. First, RAW264.7 cells loaded with gold nanospheres were injected in a tumor-bearing mouse. The tumor was imaged before injection and after 6 or 24 hours of administration of gold nanospheres-loaded RAW264.7 cells. The distribution of hemoglobin, deoxy hemoglobin and nanoparticles was obtained as shown in Figure 3.9 using spectroscopic PA image analysis considering the individual spectra of the absorbers (Figure 3.9, d). As the extinction spectra of the cells loaded with spherical gold nanoparticles was similar to the deoxy hemoglobin spectra, the spectroscopic analysis could not distinguish nanoparticle contrast from that of the deoxy hemoglobin.

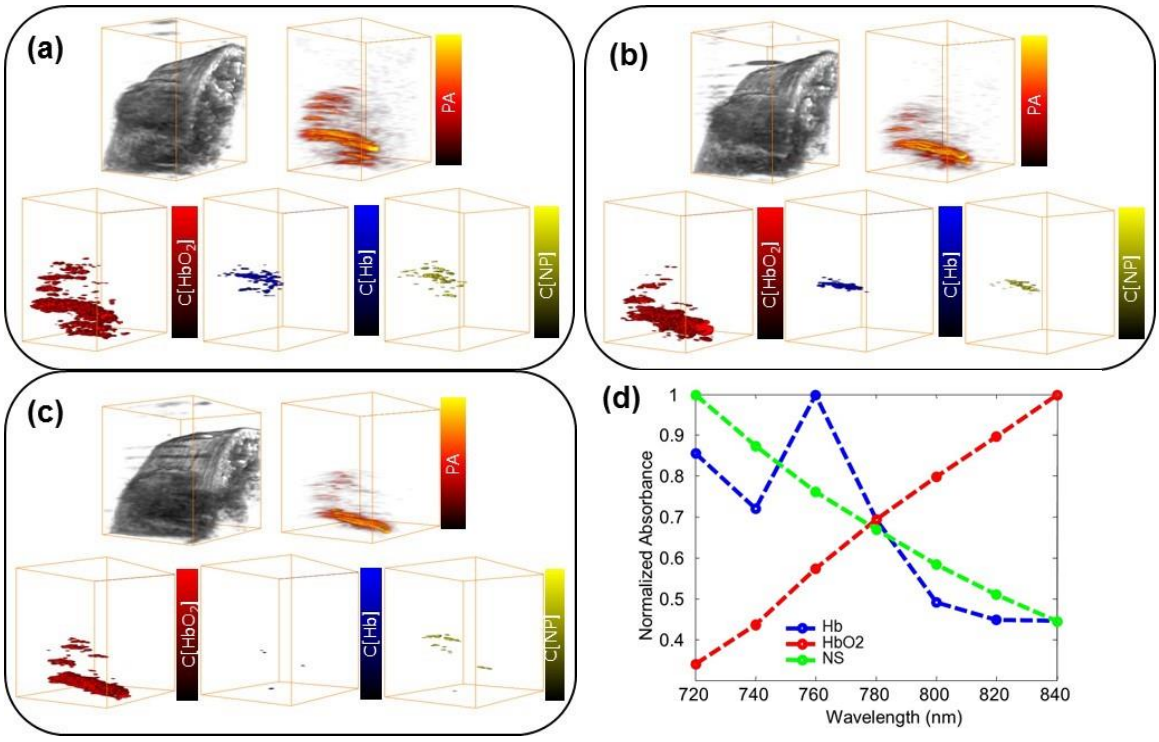

Figure 3.9 *In vivo* longitudinal spectroscopic photoacoustic imaging of A431 tumor in mouse before (a) injection of RAW267.4 cells loaded with gold nanospheres and after 6 hours (b) or 24 hours (c) of injection of gold nanospheres-loaded RAW267.4 cells. Images in each panel includes ultrasound image (gray), photoacoustic image (orange), distribution of hemoglobin (red), deoxy hemoglobin (blue) and gold nanospheres-loaded RAW264.7 cells from spectroscopic PA imaging. Normalized absorption spectra (d) of the three absorbers used in spectroscopic PA image analysis.

We then performed the similar study with RhSilicaNRs-loaded RAW264.7 cells injected in tumor-bearing mice. The normalized spectra for the three absorbers differed significantly as seen in Figure 3.10. As a result, when only cells without any nanorods were administered, the spectroscopic analysis of PA images did not show any contrast related to the nanorods (Figure 3.11, a). However, when RhSilicaNRs-loaded RAW264.7 cells were injected, the signal correlated to gold nanorods increased with time (Figure 3.11, b). This

preliminary study revealed the feasibility of *in vivo* tracking of cells labeled with silica-coated gold nanorods using spectroscopic photoacoustic imaging. For this study, we observed significant enhancement of signal related to gold nanorods only for one out of three mice imaged. For the future studies, enhancing the tumor-homing properties of the immune cells before injecting them in mice may increase the accumulation of labeled cells within the tumor. Additionally, an *in vitro* tumor model of spheroid can greatly facilitate understanding of immune cells' infiltration within tumor.[251] Three-dimensional spheroids of cancer cells can be readily prepared and grown to an appropriate size to mimic necrotic core similar to the solid tumor *in vivo*. [252]

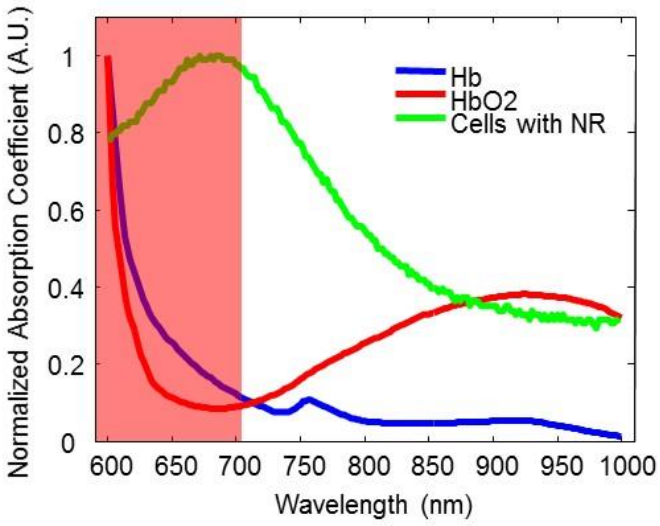

Figure 3.10 Normalized absorption spectra (red-color shaded portion) used for spectroscopic image analysis for Figure 3.11

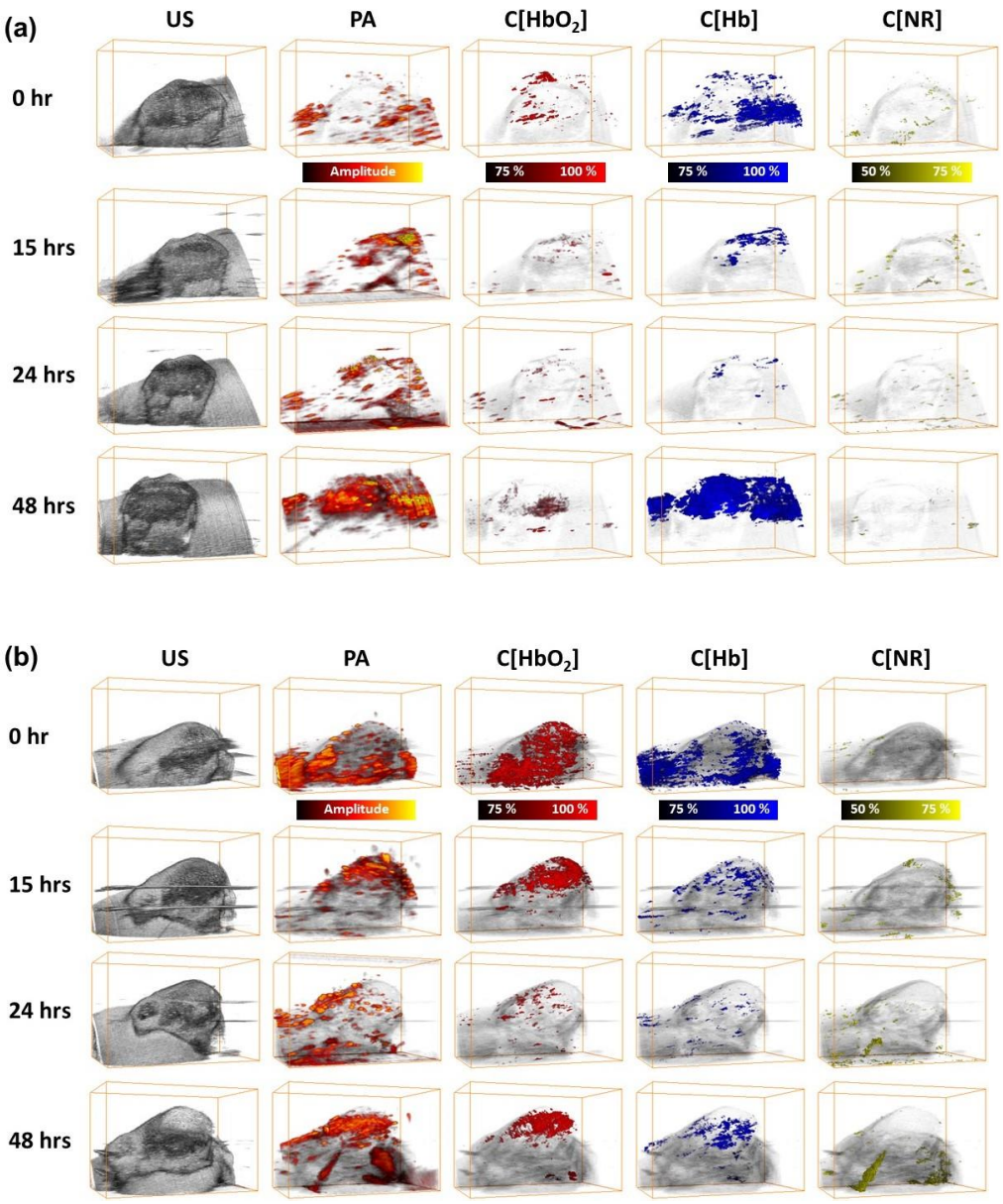

Figure 3.11 *In vivo* longitudinal spectroscopic photoacoustic imaging of A431 tumor in mice after injection of either RAW264.7 cells only (a) or RAW264.7 cells loaded with RhSilicaNRs (b).

3.4 SUMMARY

In summary, we systematically addressed challenges associated with applications of gold nanorods in cell imaging. First, we demonstrated long-term biocompatibility of fluorescent silica-coated nanorods for cell tracking experiments. Then, we showed that silica-coated nanorods do not alter optical properties upon cellular uptake that can facilitate multiplex imaging and tracking of various cell populations. Furthermore, our previous studies demonstrated that silica coating increases stability [241] and signal strength [253] of gold nanorods in PA imaging. The combination of these properties that are afforded by silica coating results in the detection limit of just few labeled cells in tissue mimicking phantoms. These promising results provide the foundation for applications of silica-coated gold nanorods and PA imaging in tracking of cells in studies ranging from the mechanistic understanding of immune responses in cancer and cardiovascular diseases to the cell mediated delivery of therapy.

Chapter 4: Biodistribution and Clearance of Near-IR Contrast Agents

4.1 Introduction

The clinical use of any contrast or therapeutic agent necessitates thorough investigation about its biodistribution and clearance. An ideal contrast agent would have sufficient blood circulation time to allow accumulation in the diseased area, and then would be able to excrete from the body within a reasonable timeframe to avoid long-term accumulation and adverse side effects. The abundant literature on *in vivo* circulation and clearance of nanoparticles provides insight into the size and surface chemistry of nanoparticles that can be optimal for enough circulation time in blood facilitating imaging and therapy. [126-129, 132] Renal excretion of nanoparticles with a size less than 5-nm is efficient; however, larger nanoparticles that cannot degrade in a biological environment become sequestered in the mononuclear phagocytic system (MPS) organs, mostly the liver and spleen.[130, 131, 254, 255] Quick excretion of small nanoparticles, however, does not allow enough circulation time in the blood to facilitate accumulation in the diseased site. The contrast agents for cancer imaging need to have enough circulation time in the blood to accumulate at the tumor site via enhanced permeability and retention (EPR) effect. Although, larger nanoparticles with optimized surface stay longer in blood circulation, but they also accumulate in MPS organs.[254] Clinically acceptable contrast agents should satisfy both criteria: 1) long enough blood residence time for accumulation in the diseased site and 2) clearance from the body within a reasonable time after imaging.

Gold nanorods optimized earlier in this dissertation are excellent near infrared contrast agents suitable for *in vitro*, *ex vivo*, or preclinical research using small animals. Prolonged accumulation of gold nanorods in the liver and spleen, however, renders them

poor candidates for clinical applications. [132, 256, 257] Although their bigger size imparts sufficient blood residence time, efficient renal clearance requires nanoparticles with smaller size (5-nm or less).[130] Recently, biodegradable nanoclusters from small gold nanoparticles (5-nm) and block-co-polymer of polylactic acid (PLA) and polyethylene glycol (PEG), PLA (1k)-PEG(10k)-PLA(1k) are synthesized. By varying polymer/Au ratio, the gold nanoclusters of various size were formed. The equilibrium size the nanoclusters was governed by the balance of short-ranged attractive forces with longer-ranged electrostatic repulsive forces between the charges particles.[138] Although the primary gold nanoparticles used for the synthesis of the nanoclusters possess overall negative charge, they have shown to resist protein absorbance even in undiluted serum. [258] Moreover, the biodegradable nanoclusters can be degraded to their original size in acidic environments of the cellular endosomes,[137] and the degraded nanoparticle also retain their protein repelling abilities. As the degraded nanoparticles do not absorb any proteins and retain their sub 5-nm size ideal for renal excretion, the biodegradable gold nanoclusters make perfect candidate for clinical applications having optimum blood-residence time and good renal clearance.

Apart from the physical characteristics suitable for *in vivo* application, these clusters also have a strong near infrared absorption necessary for *in vivo* imaging. [139] Because the biodegradable clusters possess all the characteristics of an ideal clinical contrast agent, this study evaluates these promising nanoparticles in terms of their biodistribution and clearance using *in vitro* as well as *in vivo* studies.

4.2 RESEARCH APPROACH

4.2.1 Materials and Methods

Synthesis of biodegradable clusters: The biodegradable nanoclusters were synthesized with little modification of the published procedure. [137, 138] Briefly, citrate-capped gold nanospheres with a size less than 5-nm were coated with lysine by adding 20 µL of freshly prepared aqueous solution of 5% w/v (50 mg/mL) lysine to a 1.2 mL of citrate-capped nanospheres (3 mg Au/mL) solution. Nanoclusters were formed by adding aqueous solution of PLA (poly-lactic acid)(1k)-b-PEG (polyethylene glycol)(10k)-b-PLA(1k) polymer to the nanospheres' dispersion and evaporating 50% of the solution under air flow for 40 min. The nanoclusters were diluted to 0.05 mg Au/mL in water and filter sterilized using 0.45 µm filter before concentrating to 2.7 mg Au/mL using centrifugation. PEGylated nanoclusters were prepared by adding 5-kDa mPEG-SH to the diluted clusters and letting them react for 20-minutes at room temperature before filter sterilization and centrifugation.

Animal studies: All animal studies performed for this chapter were approved under IACUC protocol AUP-2012-00020. The *in vivo* clearance study was conducted with an intravenous injection of normal Balb/c female mice (2-4 months old) with 200 µL of gold nanoclusters solution (2 mg Au/mL). Before injection, 2.7 mg Au/mL nanoclusters were diluted to 2 mg/mL using phenol-free DMEM media with serum. After the injection of the nanoclusters, each mouse was housed in a separate metabolic cage for collection of urine and feces. The mice were sacrificed after 1, 7, or 14 days. Immediately after euthanasia, blood was collected to perform an alanine aminotransferase (ALT) test using a kit purchased from Abcam (ab105134). Five mice at each time point were injected with gold nanoclusters. For each time point, one mouse was injected with diluted DMEM media (the

same dilution used for the nanoclusters) to use as a control. Various organs including liver, spleen, and kidneys were collected, digested using microwave digestion system in concentrated acid solution (10 mL conc. HNO_3 + 1 mL conc. HCl) and analyzed for their accumulation of gold using ICP-MS. A portion of these tissues was fixed in formalin for histopathological analysis.

In vitro **Clearance Study**: Clearance of biodegradable nanoclusters from mouse macrophage cells (J774A.1, ATCC) and mouse hepatic sinusoidal endothelial cells (T0102, Applied Biological Materials, Inc., referred as LSECs in this report) over a period of one week was performed. Phenol free DMEM with 1% penicillin-streptomycin supplemented with either 10% FBS (for J774A.1 cells) or 5% FBS (for LSECs) was used for this study. Cells were plated (1000 cells per cm^2) in tissue culture flasks/dishes and allowed to adhere overnight. Gold nanoclusters were preincubated in fetal bovine serum (FBS, 50%) for 2 hours before exposing to cells. Cells were incubated with nanoclusters (0.2 mg Au per mL of phenol free DMEM media with 1% penicillin-streptomycin and 7% FBS) for 4 hours. At the end of incubation time, the nanoclusters were removed and the cells were washed with PBS (without calcium and magnesium) twice before a fresh cell culture media was added and they were allowed to grow for 0, 1, 4 or 7 days. The media was changed once on day 4. All of the experiments were done at least in triplicates. At a specified time, the cells were harvested (LSECs by trypsin and J774A.1 by scrapping), counted, and their extinction measured using UV-Vis. Cells were recovered from UV-Vis measurement and analyzed with ICP-MS for gold quantification after digestion in concentrated aqua regia (3:1 HCl:HNO_3 by volume). The cell viability was compared to control cells using Calcein AM staining of live cells.

4.3 Results and Discussion

One of the major concerns regarding the use of metallic contrast agents in the clinic is their sequestration in the MPS organs. The inability of the contrast agent to be cleared from the body after imaging can cause long-term toxicity due to prolonged accumulation. [126] Nanoparticle size, along with surface functionality, plays an important role in renal clearance. Nanoparticles less than 5-nm can be effectively cleared though the kidneys [130, 255] and the larger nanoparticles accumulate in the liver and spleen with no indication of clearance over time. [132, 256] However, the downside of quick clearance is that there is not enough time for systemic circulation to effectively label the organs of interest and facilitate imaging. Furthermore, gold nanoparticles less than 5-nm do not have near-IR absorbance and hence are not suitable for *in vivo* imaging.

The perfect clinical contrast agent would have good near-IR absorbance with size and surface properties ensuring long enough circulation to serve imaging needs and achieve clearance from the body within a reasonable time post-imaging. In this study, we have evaluated biodegradable nanoclusters synthesized from 5-nm gold nanospheres and biodegradable polymer. Nanoclusters' size is tunable to achieve necessary circulation time, however the biodegradable polymer degrades within the acidic endosomal compartments of cells and results in smaller primary particles that can potentially be excreted by the kidneys.[138] The biodegradable clusters are synthesized using poly-lactic-acid and poly-ethylene glycol co-polymer and less than 5-nm diameter spherical gold nanoparticles. The primary particles that form after degradation of the clusters do not absorb serum protein even in 100% serum and thereby keeping their size small enough for renal clearance.[258] Although the individual primary nanoparticles do not have any near-IR absorbance, the biodegradable clusters have high near-IR extinction due to plasmon coupling between the primary nanospheres (Figure 4.1). Here we evaluate biodistribution and clearance of

biodegradable nanoclusters in mice to reveal the feasibility of using these contrast agents in the clinic. The excretion characteristics of these nanoparticles from major cells types in the RES system is established using an *in vitro* cell clearance study in hopes of developing a cell-based screening model to predict the outcome of *in vivo* excretion of novel nanoparticle formulations.

Biodegradable nanoclusters with optical and physical characteristics shown in Figure 4.1 were used in this study. The nanoclusters with 20 nm size showed high near-IR absorbance. The zeta potential of these nanoclusters at pH 7 in water was -13 mV.

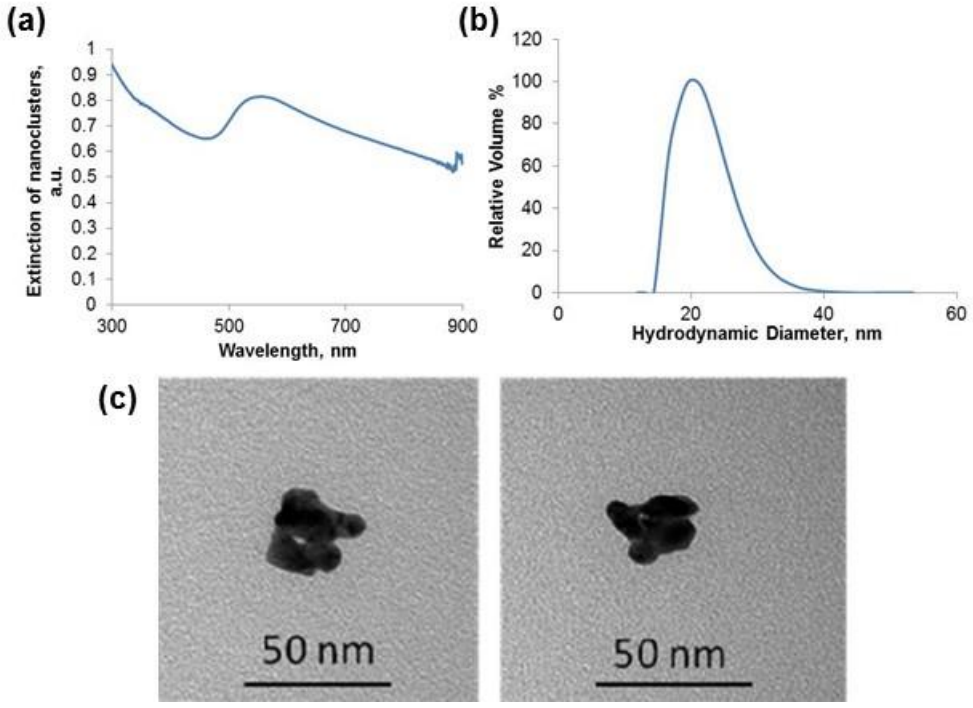

Figure 4.1 UV-Vis extinction spectra (a) and dynamic light scattering (DLS) based size distribution (b), and TEM images (c) of gold nanoclusters. (Nanoclusters are synthesized and characterized by Prof. Keith Johnston's lab). Gold nanoclusters of size 20 nm show good near-IR extinction.

The animal study design for this project is depicted in Figure 4.2. Normal Balb/C mice were injected with nanoclusters, PEGylated nanoclusters or just a diluted media via tail vein. The mice were then housed in the metabolic cages to facilitate collection of feces and urine (Figure 4.3). After a specific time, the mice were euthanized and the blood and organs were harvested for further analysis.

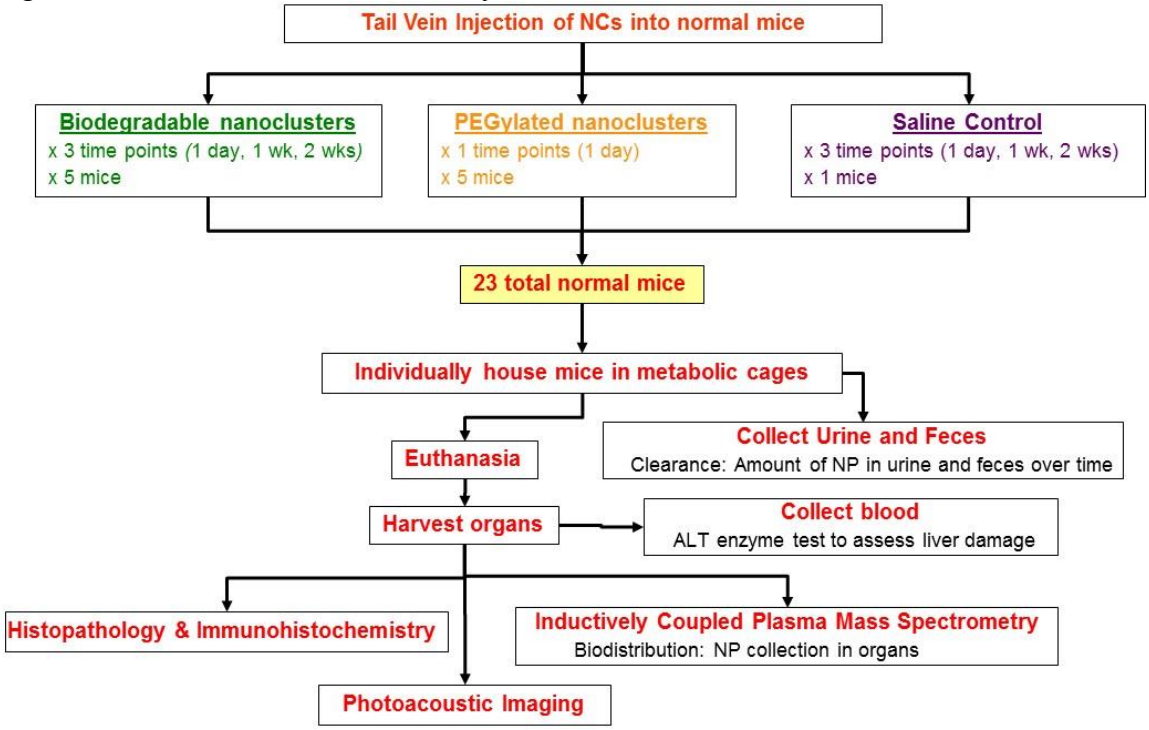

Figure 4.2 Flow chart of biodistribution and clearance study of biodegradable nanoclusters in normal mice

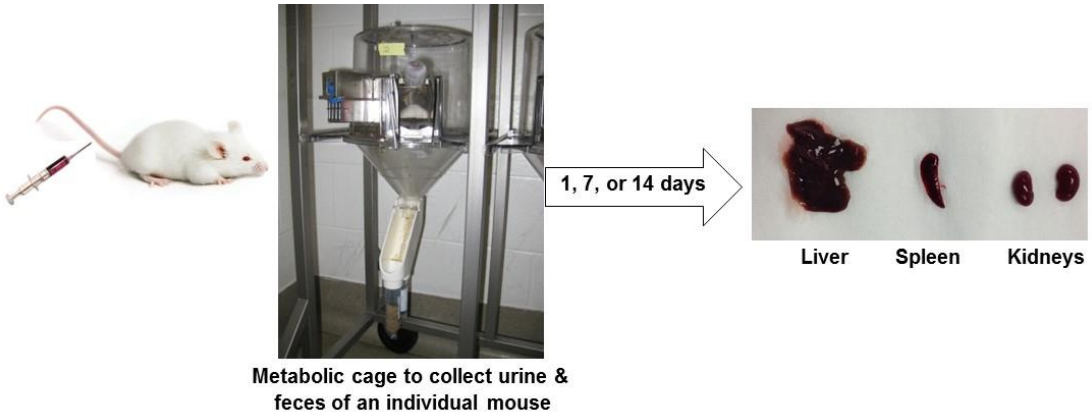

Figure 4.3 Visualization figure for biodistribution and clearance study performed for this project

The mice were sacrificed on 1, 7, or 14-days post injection of nanoclusters; biodistribution of gold in MPS organs was determined using ICP-MS (Figure 4.4). After one day of systemic circulation, no gold was detected in the blood with the majority of the injected dose having accumulated in the liver. Interestingly, only within the first week, 25% of the accumulated gold per gram of liver was cleared (statistically significant difference). The significant clearance of gold only within one-week period is encouraging, as the prior study done using higher dosage (1.2 mg Au per mice) of gold nanoclusters (size 40 nm) did not show any statistically significant clearance of gold from liver until 3-month time point. [259] The slow clearance observed for that study may be due to using very high dosage of gold that may have overwhelmed the clearance system. Fast clearance of gold nanoclusters is very promising, however, the continued clearance of gold was not observed after the first week. Gold accumulation in the liver at the two-week time point was statistically the same as at the one-week time point. Initial clearance of nanoclusters followed by a stagnant phase lead to an interesting revelation about the complex biological system with the interplay of different cells in MPS organs facilitating clearance.

Figure 4.4 Biodistribution of gold nanoclusters in mice with respect to time. Number given by n represents the number of animals used per time point. Statistically different results compared to day 1 based on student t-test (p-value < 0.05) are identified by *.

The macrophages of the liver and spleen are considered to be the main role players in clearing systemically injected foreign materials. [260] Here we processed the liver fixed in formalin with a silver stain to highlight gold nanoparticles and with a F4/80 stain to label macrophages. Figure 4.5 shows the liver images of mice after one day of nanoclusters' injection. In the microphage-stained image, the gold nanoparticles are also visible due to a high contrast in bright field imaging. Although nanoparticles were associated with macrophages (highlighted by the black arrow), a considerable amount of nanoparticles were also present in the non-parenchymal non-macrophage cells (denoted by red stars). Apart from the macrophage cells, the main scavenger cell type of the liver, multiple research groups highlight the role of the liver sinusoidal endothelial cells (LSECs) in clearing pathogens and toxins. [261-265] The presence of gold nanoparticles in non-macrophage cell types can be due to the involvement of LSECs in nanoparticle clearance.

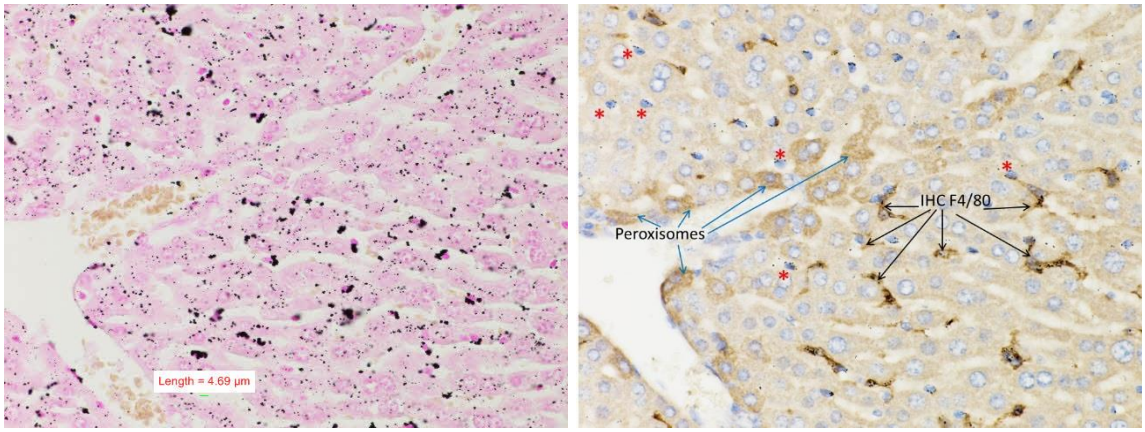

Figure 4.5 Silver stain (left) and mouse macrophage F4/80 stain (right) images of the mouse liver after one day of intravenous injection of nanoclusters. Scale bar = 4.69 µm. Blue arrows point to peroxisomes in the cells that are stained lightly. Black arrows point to the liver macrophages. Nanoparticles in non-macrophage cells are marked by a red asterisk (*)

Analysis of silver-stained and F4/80-stained liver images using ImageJ and Matlab from mice euthanized on 1, 7 or 14-days after nanoclusters' injection reveals that the percentage of pixels with nanoparticles overlapping with macrophages are small for day 1 and day 7. However, the overlap of nanoparticles with macrophages increased 4-times within the second week after the nanoclusters injection (Figure 4.6). The increase in the percentage of nanoparticles overlapping with macrophages during the second week can be due to: 1) clearance of nanoparticles from the non-macrophage cells resulting in more nanoparticles per image associated with the macrophage cells or 2) transfer of nanoparticles from the non-macrophage cells to the macrophages within the second week. Because ICP-MS results (Figure 4.4) do not show clearance within second week, the first option of net clearance of nanoparticles from the liver would not hold true. However, the nanoparticles can be transferred from the other cells to macrophage cells via intercellular transfer or by phagocytosis of nanoclusters-loaded dying cells by the macrophages.

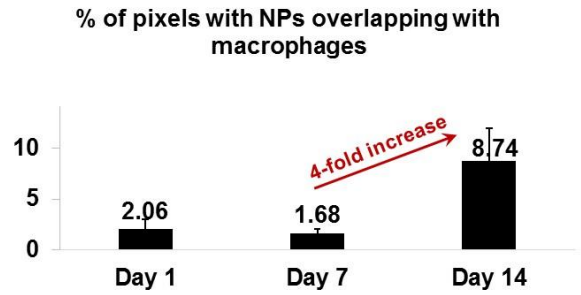

Figure 4.6 Results from the image analysis of the silver-stained and macrophage (F4/80)-stained images of the liver performed using ImageJ and Matlab

Liver sinusoidal endothelial cells (LSECs) clear 90% of the adenovirus from blood circulation within minutes. [264] Fast clearance of the small size pathogen from circulation can be due to efficient endocytosis by LSECs. Endocytosis observed in LSECs is mainly clathrin-dependent, with LSECs having twice as many clathrin-coated pits per unit membrane compared to Kupffer cells. [266] Apart from the fast uptake kinetics of LSECs, the degradation products of the ligands for scavenger receptors and mannose receptors on LSECs appear in circulation within minutes. [265] The recent *in vitro* study by Detzel, et al. reveals that 60-70% of gold nanoparticles are cleared from both the hepatocytes and liver sinusoidal endothelial cells within seven days. [267] Alternatively, Kupffer cells show a slow clearance of phagocytosed material. [268, 269] Combining these traits of LSECs and Kupffer cells, clearance of gold from the liver during the first week, as observed by ICP-MS analysis (Figure 4.4), can be due to the fast clearance from LSECs. An increase in the percentage of nanoparticles overlapping with macrophages from histology image analysis (Figure 4.6) can be due to the transfer of remaining NPs from LSECs to the

macrophages during the second week either by phagocytosis of LSECs containing gold NPs by macrophages or by an alternate intercellular transfer mechanism.

Blood concentration of the liver enzyme – Alanine transaminase (ALT) – normally increases during liver damage.[270] For all mice injected with nanoclusters, the ALT concentrations were similar to the control mouse, suggesting that the nanoclusters do not have any adverse effect on liver functions (Figure 4.7).

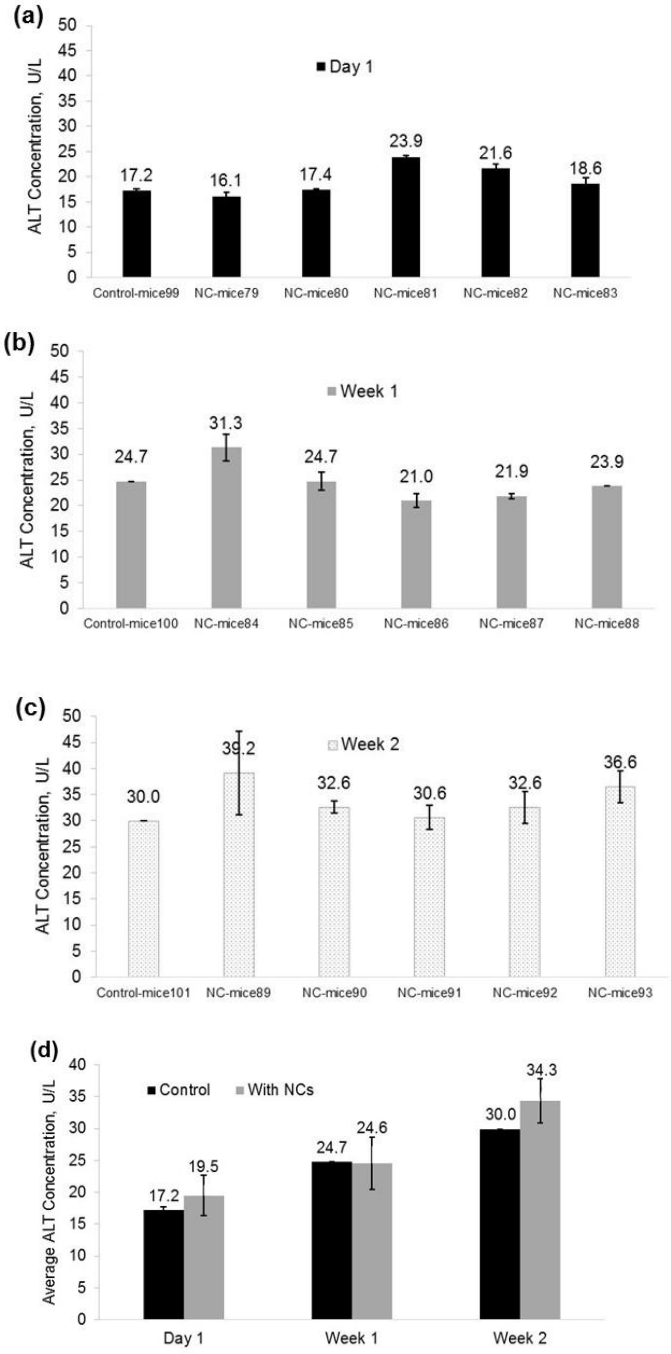

Figure 4.7 Concentration of ALT enzyme in the blood of individual mouse at day 1 (a), week 1 (b), week 2 (c). Average concentration of ALT enzyme in control and nanoclusters-injected mice after different time points (d). Normal level of the liver enzyme, ALT, suggests no changes in liver function after injection of gold nanoclusters in mice.

Combined photoacoustic and ultrasound imaging was performed on the excised livers of the control mouse and mice injected with nanoclusters at different time point after nanoclusters' administration (Figure 4.8). Strong PA contrast was observed from livers of mice injected with nanoclusters with no significant contrast from the liver of control mouse. This observation suggests the feasibility of detecting nanoclusters distribution *in vivo* using noninvasive photoacoustic imaging combined with ultrasound imaging.

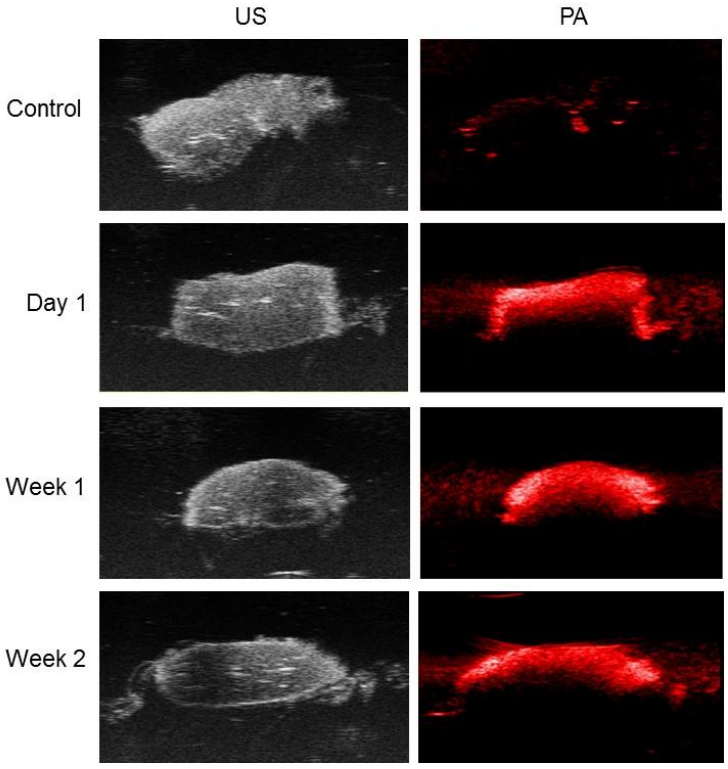

Figure 4.8 Ultrasound (US) and photoacoustic (PA) images of the excised livers of the control mouse and mice after one, seven and fourteen days of gold nanoclusters' injection. PA imaging performed at 700 nm. Each image covers 8 x 14 mm field of view.

The effect of PEGylation on biodistribution of nanoclusters was studied by intravenously injecting PEGylated clusters into mice. Figure 4.9 shows the distribution of NPs in RES organs and blood for mice injected with nanoclusters and PEGylated-nanoclusters after one day of nanoparticles administration. The distribution of nanoclusters with and without PEG changed drastically between the liver and spleen. The spleen took up PEGylated nanoclusters about 7-times more compared to regular nanoclusters, with consequent decrease in uptake by the liver for the PEGylated nanoclusters. One explanation for the difference in biodistribution can be the increased blood residence time of the nanoparticles due to PEG-coating, which in turn results in a greater accumulation of PEGylated nanoparticles in the spleen. [271, 272]

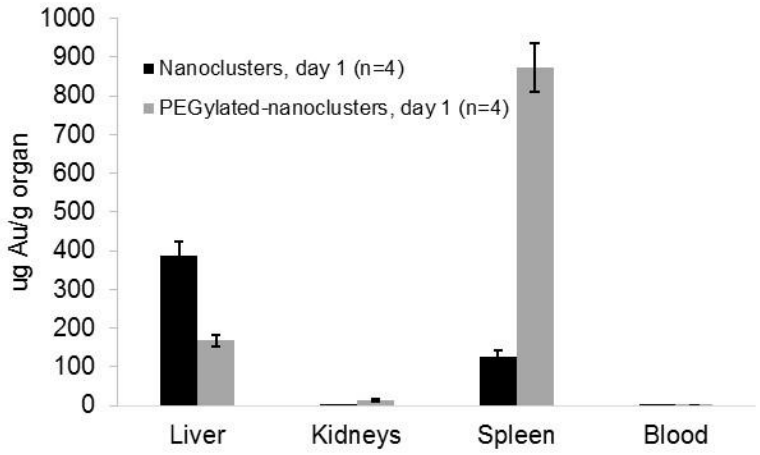

Figure 4.9 Distribution of nanoclusters and PEGylated nanoclusters in RES organs in normal Balb/c mice after one day of intravenously injection. Number denoted by n is the number of animals used.

Clearance of nanoparticles from systemic circulation depends on opsonization of the nanoparticles in blood. Although the biodegradable nanoclusters used in this project do have some surface coverage of PEG, further PEGylation of nanoclusters increases PEG density, changing the kinetics of nanoclusters' opsonization in blood, and thereby changing the uptake kinetics by hepatic phagocytes. [236, 273] Additionally, the spleen clears foreign materials by non-phagocytic filtration mechanisms and thereby does not depend on opsonization kinetics. [274, 275] It was shown that the nanoparticles with a size greater than 100 nm are cleared more efficiently by the spleen than the smaller nanoparticles. Clearance mediated by the spleen also depends on the surface coating of polymeric nanoparticles with particles coated with hydrophilic polymers cleared by the spleen in greater amounts than uncoated particles for all sizes. [275] When tested for *in vitro* uptake of nanoparticles by splenic white cells in the presence or absence of serum, the uptake of coated nanoparticles was significantly lower compared to the uncoated ones, suggesting that the increased splenic clearance of nanoparticles with hydrophilic polymer coating is not due to the phagocytic activity of the spleen. Additionally, cell uptake was higher for any size or coating of the particles studied in the absence of serum, indicating that specific opsonization by serum proteins cannot account for higher clearance of coated nanoparticles by the spleen. Furthermore, for all nanoparticles' sizes studied, approximately 50% of the coated particles cleared by the spleen after 24 hours of injection were not associated with splenic cells, validating the *in vitro* uptake results by splenic white cells and indicating non-phagocytic clearance by the spleen. [275]

The spleens of the mice injected with nanoclusters and PEGylated nanoclusters were stained with H&E, F4/80 macrophage stain and silver stain (Figure 4.10 and Figure 4.11). In the images on the right hand side, the white pulp area is marked by the black circles. For the mice injected with nanoclusters, silver-stained images revealed scant

presence of nanoparticles in the marginal zone area between the white pulp and red pulp (Figure 4.10). Conversely, PEGylated nanoclusters accumulated heavily in the red pulp one day post injection (Figure 4.11). The marginal zone of the spleen is equipped with specialized subsets of macrophages, B-cells and dendritic cells, whereas the red pulp section of the spleen is dedicated to the filtering of blood. [276] The evidence that only a scant amount of nanoclusters were present in marginal zone for the mice injected with nanoclusters supports the previous literature that the major role of the spleen in clearance is not dependent on phagocytosis. Considerably high accumulation of PEGylated nanoclusters in the red pulp further supports the clearance by filtering mechanism rather than phagocytosis. [275]

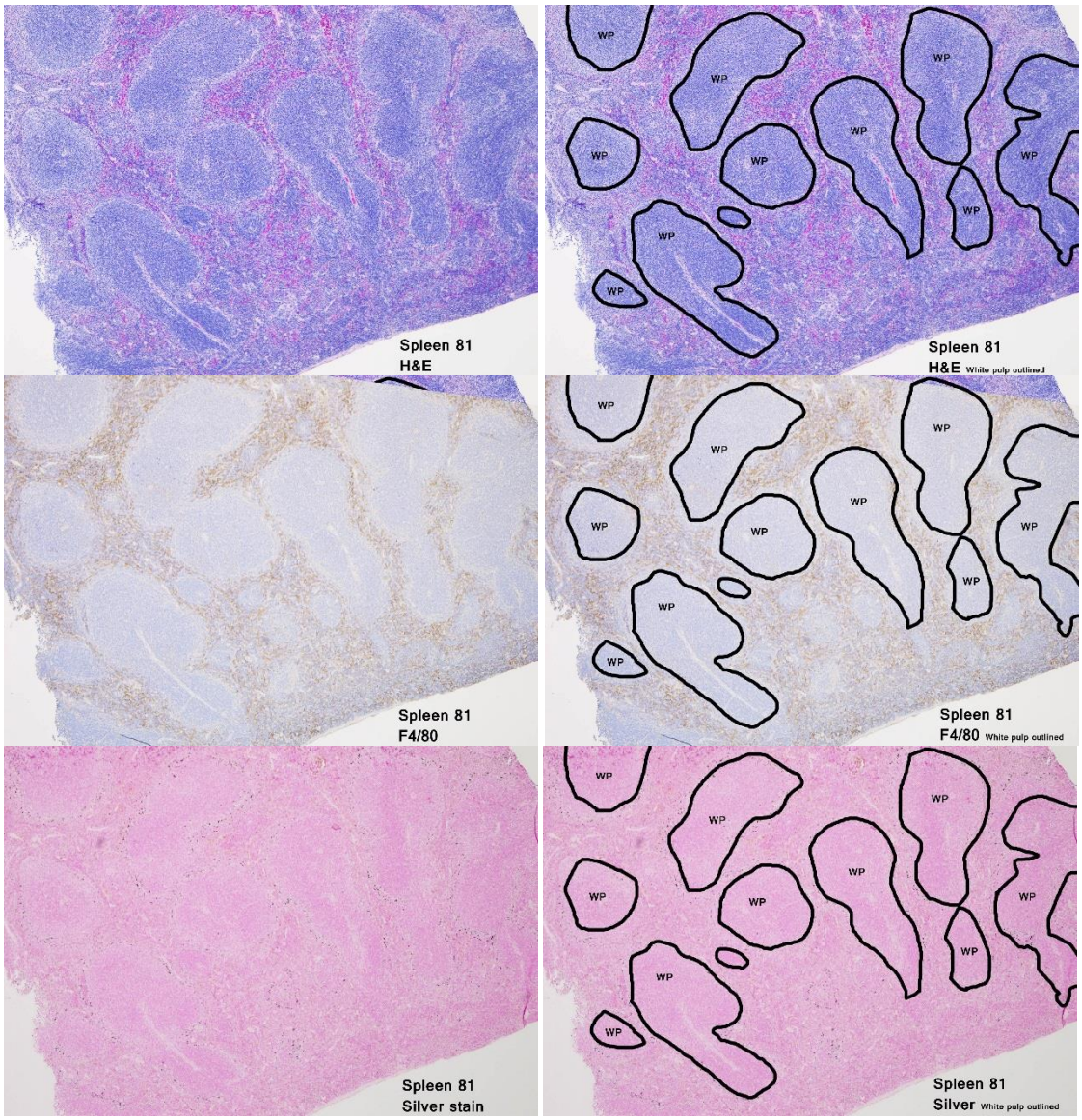

Figure 4.10 H&E (top panel), mouse macrophage (F4/80) stain (middle panel) and silver stain (bottom panel) images of the mouse spleen one day after intravenous injection of nanoclusters. Black lines in the images at right highlight white pulp (WP). Unstained area right outside WP is marginal zone.

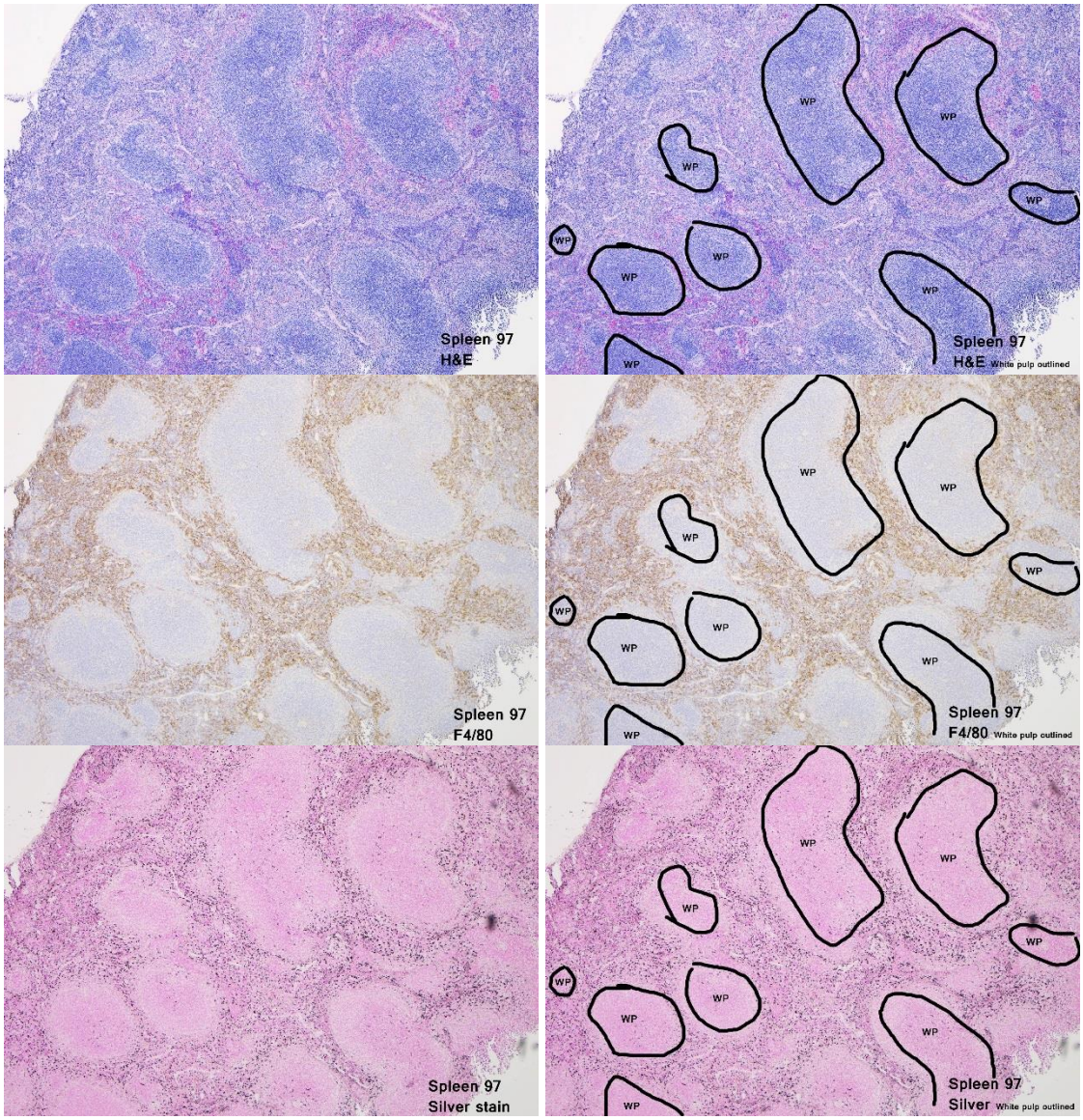

Figure 4.11 H&E (top panel), mouse macrophage (F4/80) stain (middle panel) and silver stain (bottom panel) images of the mouse spleen one day after intravenous injection of PEGylated nanoclusters. Black lines in the images at right highlight white pulp (WP). Unstained area right outside WP is marginal zone.

To test the hypothesis that clearance of nanoclusters observed from the liver within the first week is due to fast clearance from LSECs, *in vitro* cell clearance studies using main hepatic phagocytes – mouse macrophage cells (J774A.1) and mouse liver sinusoidal endothelial cells (LSECs) – was performed. Small number of either type of cells were plated and loaded with nanoclusters before observing clearance of nanoclusters over a period of 7 days. The exocytosis of nanoparticles depends on many factors including size,[140, 154, 155, 277] surface coating,[142, 145, 150, 278-280] incubation concentration[148, 156] and incubation time[154, 281-283] of nanoparticles along with cell type,[151], [152, 153] and presence or absence of serum during exocytosis[143, 151]. To mimic *in vivo* exposure of nanoclusters, LSECs and J774A.1 cells were incubated with 0.2 mg Au/mL of nanoclusters (0.4 mg Au being diluted with @ 2 mL blood in mice circulation resulting in 0.2 mg Au/mL being exposed to RES cells). Additionally, the nanoclusters would be in contact with 100% serum after intravenous injection and being coated with serum proteins. To ensure the serum coating of nanoclusters for *in vitro* study, the nanoclusters were preincubated with FBS before adding to cells. Exocytosis of the nanoclusters from cells was observed after 4 hours of incubation as the circulation of nanoparticles *in vivo* is in the order of a few hours. [132]

Clearance of nanoparticles from LSECs was confirmed by statistically significant decrease in the area under the curve (AUC) of the extinction spectra for nanoclusters-loaded cells on fourth and seventh day of clearance compared to the cells loaded with nanoparticle before any exocytosis (day 0) (Figure 4.12). Interestingly, no decrease in AUC values was observed during seven-day clearance period for J774A.1 cells ((Figure 4.12). Instead, there was an increase in AUC on day 4 compared to any other time point, which may be because of phagocytosis of nanoparticles non-specifically attached to the petri dish

by the proliferating macrophages. On day 7, the AUC again decreased suggesting the ongoing exocytosis from macrophages, however, not statistically significant compared to day 0. These findings suggests that although the macrophages do exocytose the nanoparticles during the first week, the net effect of gold clearance observed for the *in vivo* study (Figure 4.4) is not due to exocytosis from macrophages as the macrophages would also actively phagocytose other dying cells loaded with nanoparticles. On the other hand, not active in phagocytosis, LSECs uptake nanoclusters based on clathrin-mediated endocytosis followed by quick exocytosis resulting in significant clearance in gold from the liver during the first week.

Furthermore, macrophages engulf more than two-times the amount of nanoclusters compared to LSECs as seen by AUC for these cells right after the incubation with nanoclusters. This suggests that macrophages are still the main phagocytes in clearing up bulk of injected nanoclusters and the absence of clearance during second week post administration of nanoclusters in mice is likely due to majority of gold being sequestered in slow clearing Kupffer cells.

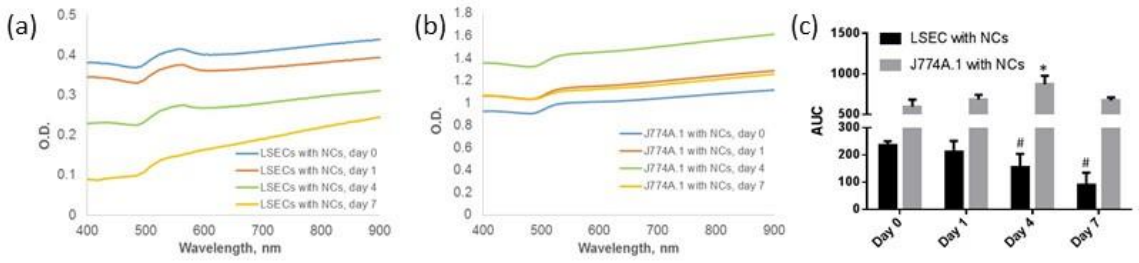

Figure 4.12 Average spectrum of LSECs (a) and J774A.1 (b) cells loaded with gold nanoclusters at different time points. (c) Area under the extinction curves for LSECs and J774A.1 cells with nanoclusters at different time points. Statistically different data (p-value < 0.05 in t-test) is marked by * (different compared to all the time point) or # (different compared to day 0)

An interesting pattern was observed in the proliferation of LSECs and macrophages during the clearance study. Macrophage (J774A.1) cells showed initial increase in proliferation during the incubation of nanoparticles (day 0) compared to control cells, however, at day 1 the number of cells-loaded with nanoclusters were less compared to control cells possibly resulting from the death of few macrophages due to engulfing large number of nanoclusters. On day 4 however the macrophage cells loaded with nanoclusters catch up with control cells and there is no difference in proliferation compared to control cells from thereon.

Proliferation pattern of LSECs loaded with nanoclusters was quite different compared to macrophages. No significant change in the number of cells loaded with nanoclusters compared to control cells was observed during nanoclusters incubation (day 0) or the day after. However, LSECs loaded with nanoclusters show statistically significant increase compared to control cells on day 4 and day 7. This observation is in accordance with the natural role of the liver endothelial cells. It is well known that LSECs facilitates liver regeneration after partial hepatectomy or liver injury due to toxins. [284] The treatment of nanoclusters is probably triggering the same response of LSECs to increase proliferation in response to the potential “toxin attack” and thereby showing two-fold increase in cell numbers at day 7 compared to control cells.

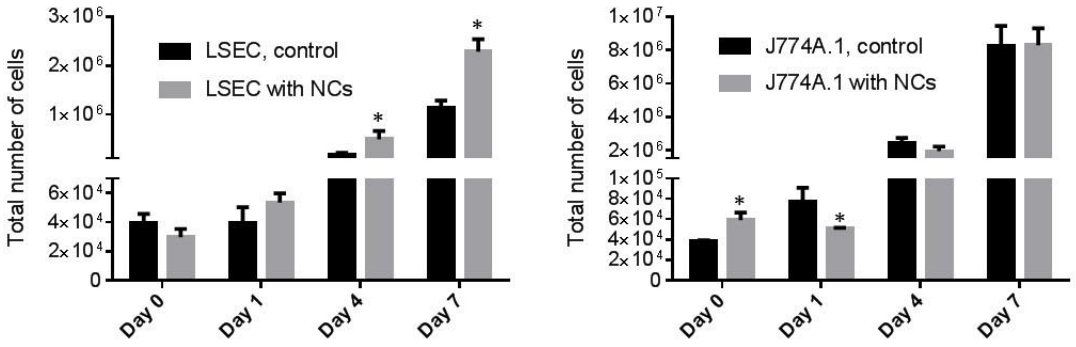

Figure 4.13 Total number of LSECs or J774A.1 cells during clearance the study. Statistically different data compared to control (t-test, p-value < 0.05) is marked by *.

The cell viability of nanoclusters-loaded cells was comparable with the control cells as revealed by fluorescence images of cells stained with Calcein AM (Figure 4.14, Figure 4.15, Figure 4.16, and Figure 4.17). As J774A.1 cells are harvested by scrapping, gold nanoclusters non-specifically attached to the petri dish is seen in the background of the bright-field and dark-field images along with the cells for day 0 and day1 images. The nanoparticles in the background disappear for day 4 as the proliferating macrophages are probably engulfing the non-specifically attached nanoparticles in the culture plate. This also supports the finding that at day 4, AUC for extinction spectra is higher compared to other time points (Figure 4.12).

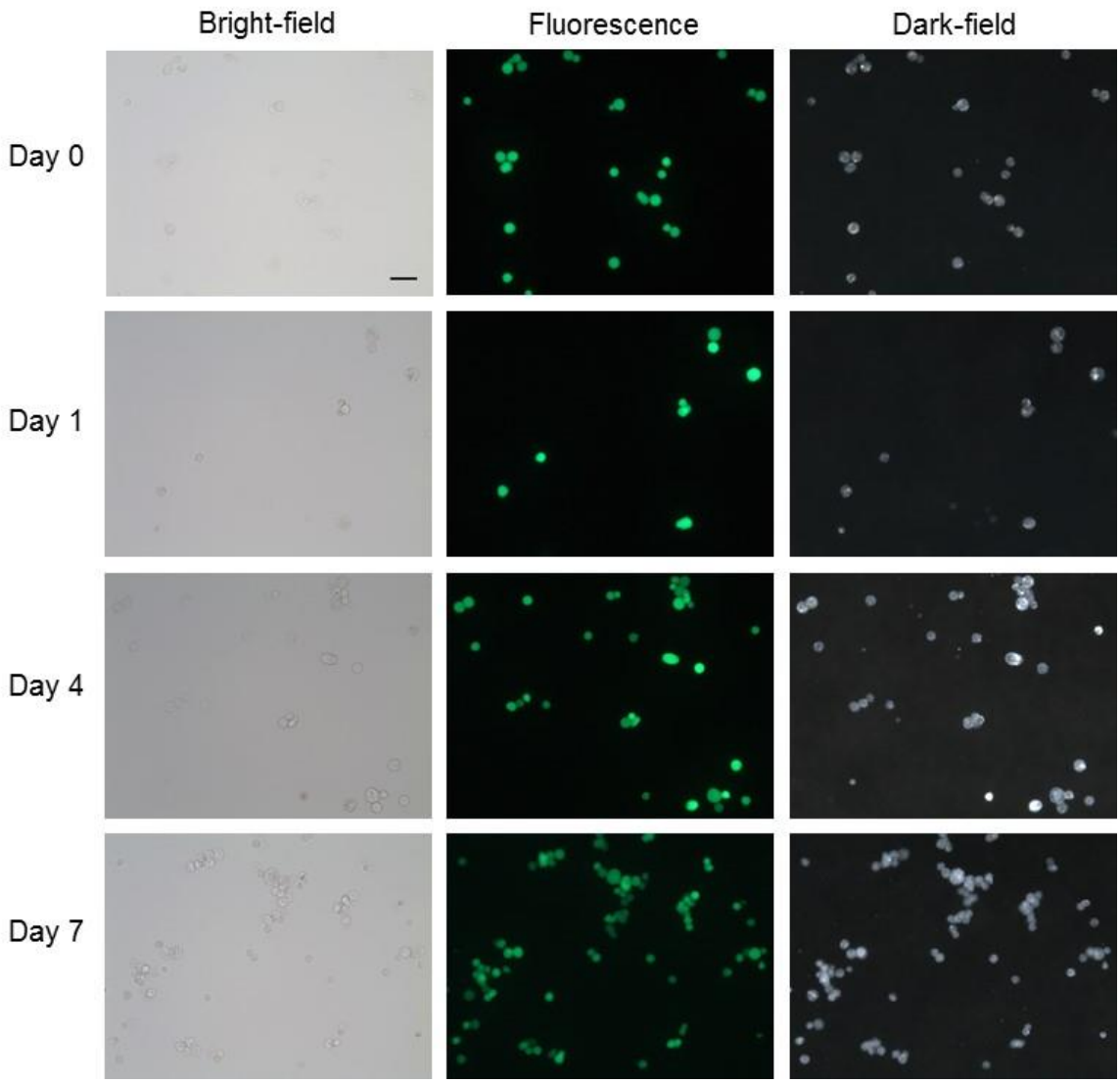

Figure 4.14 Control LSECs during the clearance study. Images in the middle show fluorescence due to Calcein AM staining reflecting cell viability. Scale bar = 50 μm

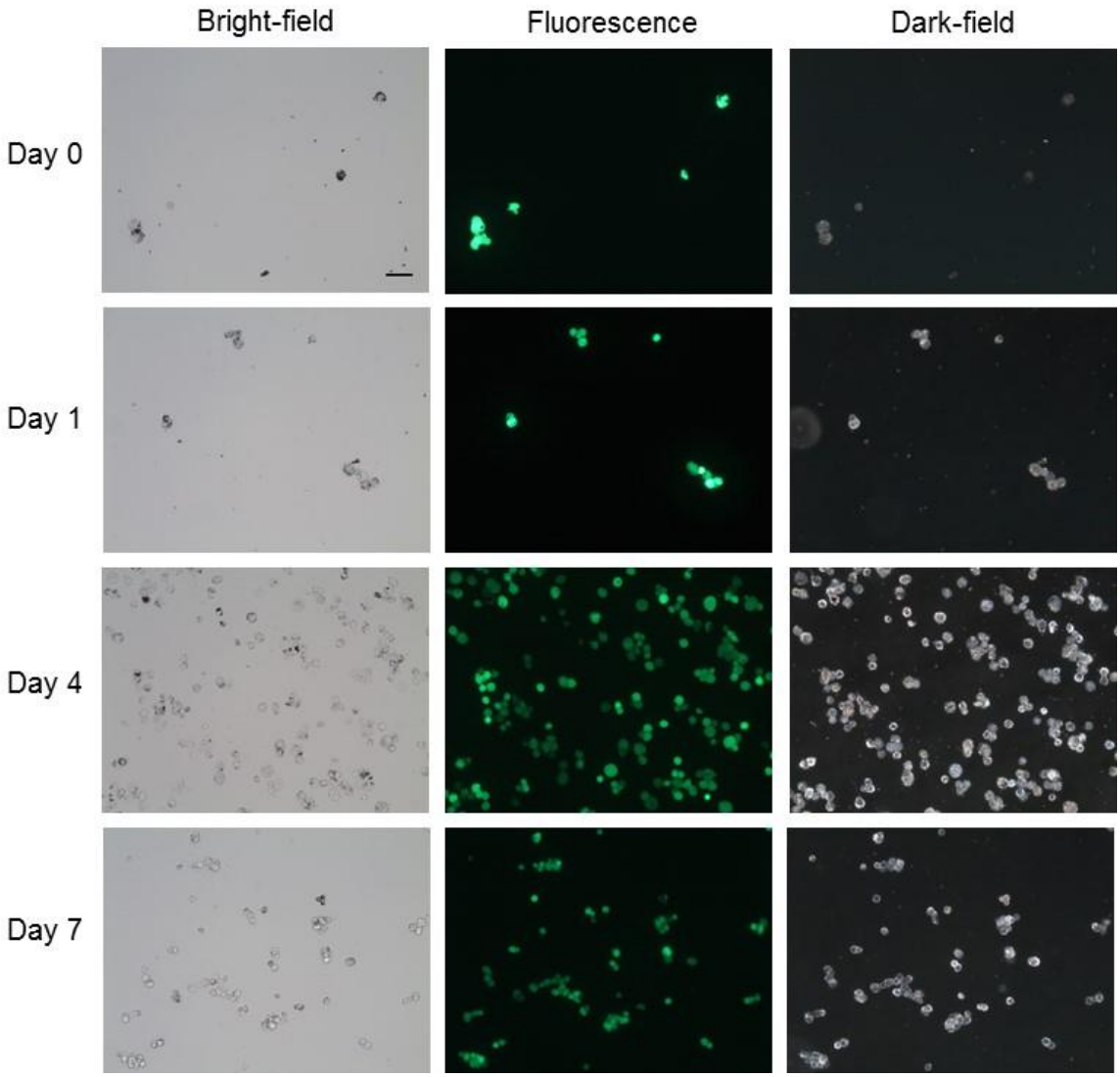

Figure 4.15 LSECs loaded with nanoclusters during the clearance study. Images in the middle show fluorescence due to Calcein AM staining reflecting cell viability. Scale bar = 50 μm

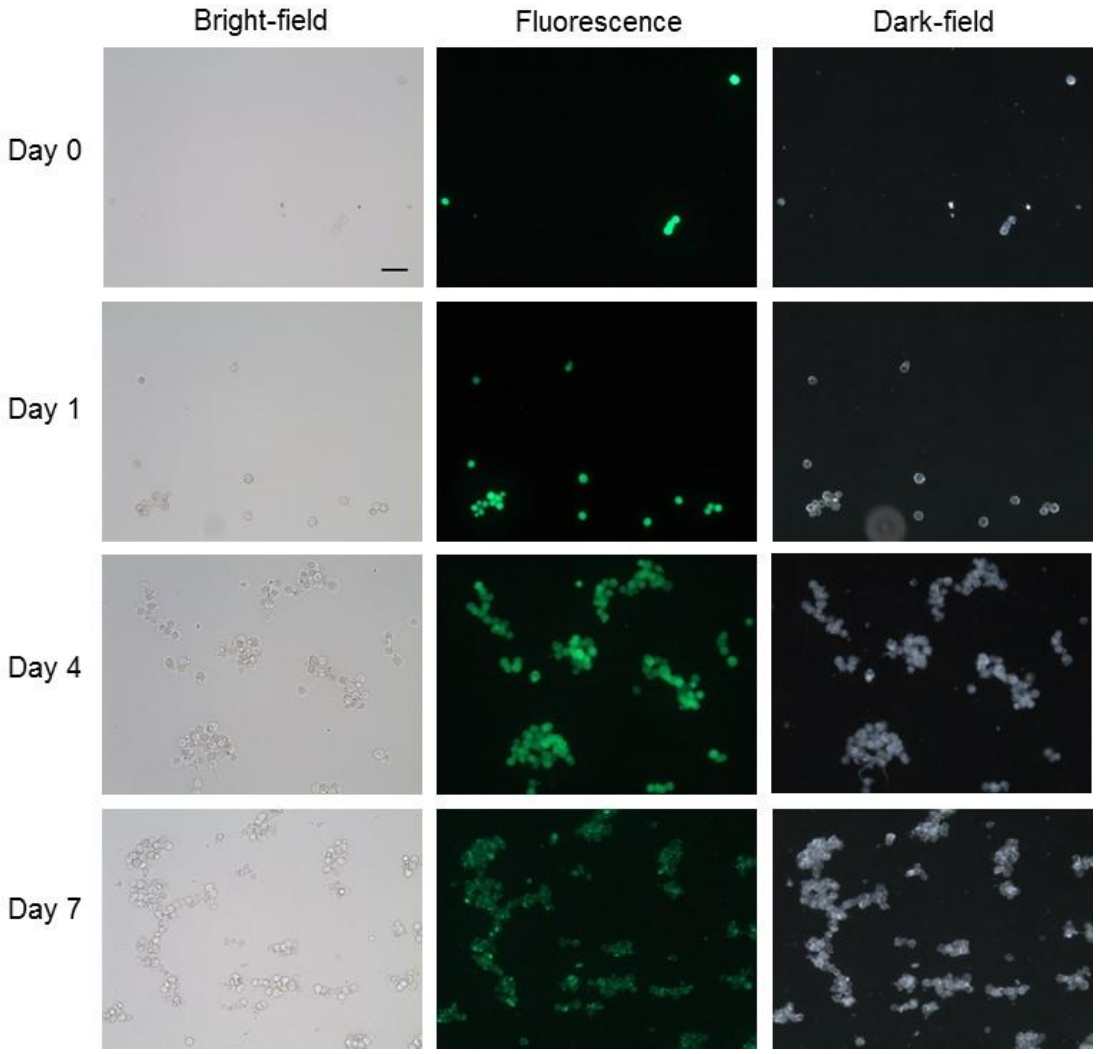

Figure 4.16 Control J774A.1 cells during the clearance study. Images in the middle show fluorescence due to Calcein AM staining reflecting cell viability. Scale bar = 50 μm

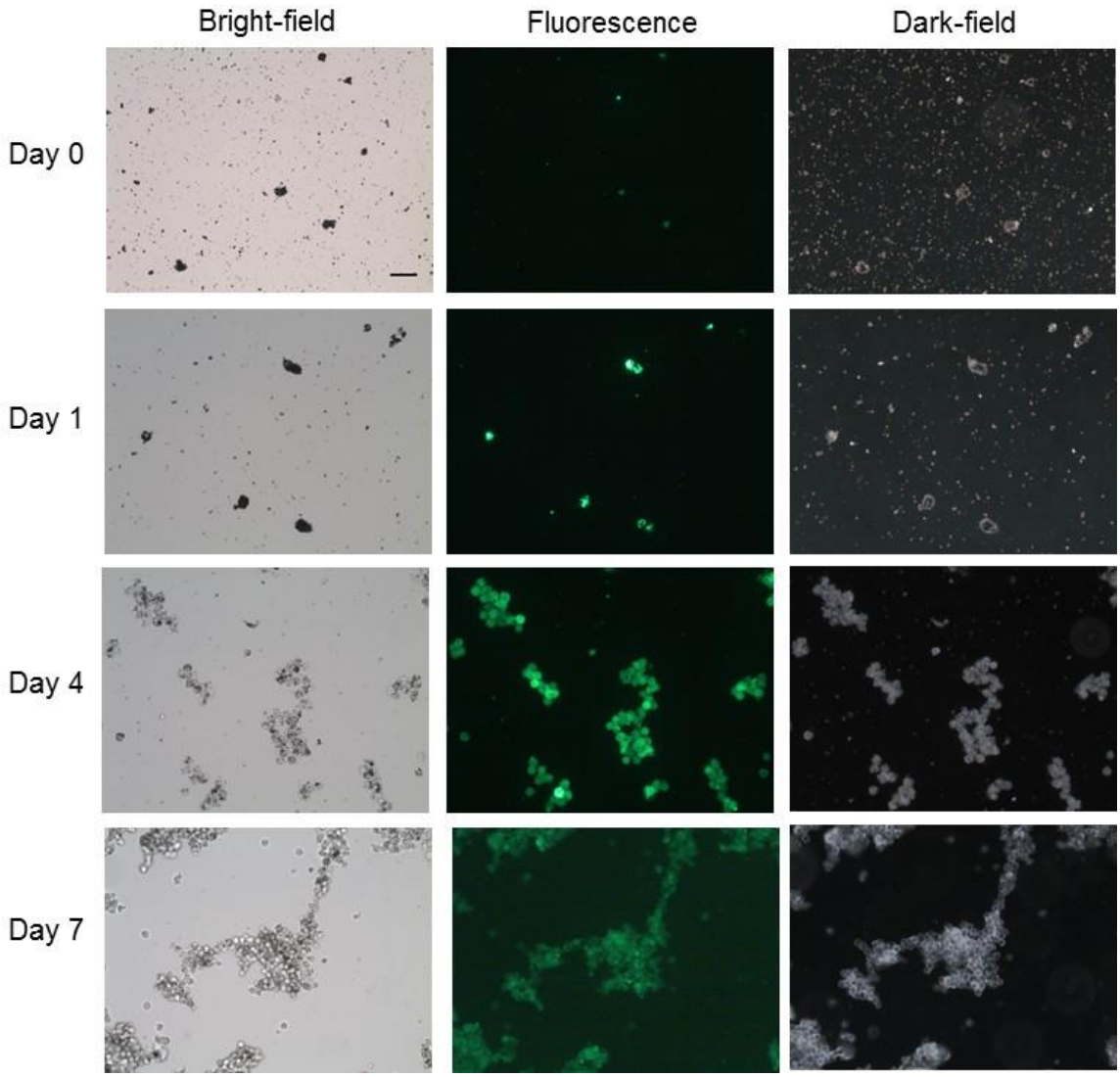

Figure 4.17 J774A.1 cells loaded with nanoclusters during the clearance study. Images in the middle show fluorescence due to Calcein AM staining reflecting cell viability. Scale bar = 50 μm

4.4 SUMMARY

In this study, we have evaluated the pharmacokinetics of biodegradable gold nanoclusters in mice. *In vitro* model proposed using the major phagocytes of the liver accurately decipher the pattern of *in vivo* clearance of nanoparticles from the liver. Liver sinusoidal endothelial cells uptake nanoparticles via endocytosis with fast exocytosis kinetics facilitating early clearance of nanoparticles from the liver. Hepatic macrophages engulf other cells loaded with nanoparticles giving rise in the presence of nanoparticles in macrophages during the second week post nanoclusters administration. As *in vitro* model closely resembles the clearance patterns of the liver, screening of contrast agents with clinical translation potential can be expedited using the fast and less expensive *in vitro* testing before pursuing more labor-intensive *in vivo* evaluations. The feasibility to screen potential contrast agents with *in vitro* model proposed in this study can free up time and resources to enable testing of multiple potential agents and facilitate quick optimization instead of waiting to get results from a time-intensive animal study. The study presented in this chapter will dramatically enhance the number of successful contrast agents being tested in preclinical studies, giving rise to the clinical translation of these promising agents.

Chapter 5: Final Remarks

5.1 Conclusions

This dissertation contributes significantly to the development of the contrast agents suitable for clinical applications by directly addressing the major challenges in translation of nanoparticle-based contrast agents to the clinic. The molecular-specific contrast agents based on gold nanorods developed in chapter 2 offer directional conjugation of antibodies to the nanorod surface, facilitating efficient targeting along with shielding the Fc portion of the antibodies to increase blood half-life by reducing uptake by immune cells via Fc receptors. The robust technique of producing molecular-specific nanorods not only provides an increase in the signal-to-background ratio by enhancing molecular-specific uptake and facilitating efficient accumulation in the diseased region through enhanced blood residence time but also offers high selectivity during optical and photoacoustic imaging. *In vivo* imaging feasibility is demonstrated using noninvasive photoacoustic imaging of cells labeled with molecular-specific nanorods. Photoacoustic (PA) imaging combined with ultrasound imaging offers a safe, cost-effective, and robust technique to obtain functional and morphological information. PA imaging has great potential for clinical use due to multiple advantages including a lack of ionizing radiation or radioactive agents, an imaging depth in centimeters with near infrared contrast agents, and feasibility for molecular-specific imaging as demonstrated in the chapter 2 of this dissertation. The molecular-specific agents developed in this chapter facilitate translational research and foster understanding of disease dynamics by providing the capability for efficient molecular-specific imaging of the diseased site.

Chapter 3 of this dissertation furthers current imaging capabilities by offering a solution to avoid plasmon coupling of gold nanorods upon cell uptake and enabling

sensitive multiplex imaging to track cells. The near-IR contrast agents developed in this project enable tracking of cells with very high sensitivity (detecting a few cells per unit imaging volume), which in turn facilitates an understanding of dynamics played by different cells in the onset, progression, and reoccurrence of a disease. The added capability of fluorescence enables *ex vivo* validation of the tissue after *in vivo* imaging during translational studies.

Chapter 4 correlates *in vivo* distribution of the biodegradable gold nanoclusters with *in vitro* study and proposes a cell culture model that can be used to predict *in vivo* fate of promising contrast agents in a fast, cost-efficient, and reliable way. The *in vitro* model would not only predict biodistribution and clearance patterns in major MPS organs but also enhance the number of these agents going to the clinical trial phase and eventually to the clinic.

The contrast agents developed in this dissertation can facilitate an understanding of biological events at the molecular level, the role of immune cells, cellular distribution, and trafficking in different disease states. Furthermore, the tools proposed in this dissertation will enhance the clinical translation of the promising contrast agents by reducing time to evaluate their biological fate, offering quick feedback for further optimization as well as facilitating robust evaluation of multiple agents simultaneously.

5.2 FUTURE DIRECTIONS

Because the current tracking of cells using silica-coated gold nanorods images the contrast agent – gold nanorods – within the cells, the imaging does not directly assess cell viability *in vivo*. Moreover, the contrast dilution with proliferation may prohibit long-term tracking. Using a strategy similar to reporter gene in combination with nanoparticles can possibly enable highly sensitive detection of proliferative cells using the noninvasive photoacoustic imaging described in this dissertation. [285-287]

For cell-based therapy and imaging using immune cells, enhancing the tumor homing properties of the cells during *ex vivo* expansion and then loading them with nanoparticles can increase the capacity of the immune cells to reach the tumor and enhance their therapeutic efficacy along with imaging sensitivity. [251]

Successful introduction of nanoparticles-based diagnostic agents to the clinic depends heavily on *in vivo* detection sensitivity as well as the clearance of the diagnostic agents after the imaging. The studies in this dissertation demonstrate an efficient way to correlate *in vivo* fate of nanoparticles using an *in vitro* model. A revolutionary approach to ensure final clearance of nanoparticles from the MPS organs is the development of "smart" nanoparticles possibly decorated with biological moieties that direct the intracellular machinery of the cells of the MPS organs to exocytose the engulfed nanoparticles within a reasonable timeframe. [288, 289]

References

[1] A. R. Kherlopian, T. Song, Q. Duan, M. A. Neimark, M. J. Po, J. K. Gohagan, and A. F. Laine, "A review of imaging techniques for systems biology," *BMC Syst Biol,* vol. 2, p. 74, 2008.

[2] I. Georgakoudi, and J. Van Dam, "Characterization of dysplastic tissue morphology and biochemistry in barrett's esophagus using diffuse reflectance and light scattering spectroscopy," *Gastrointest Endosc Clin N Am,* vol. 13, pp. 297-308, 2003.

[3] Y. L. Kim, H. K. Roy, H. Subramanian, V. Backman, P. Pradhan, R. K. Wali, V. M. Turzhitsky, and Y. Liu, "Low-coherence enhanced backscattering: Review of principles and applications for colon cancer screening," *Journal of Biomedical Optics,* vol. 11, pp. 041125-041125-10, 2006.

[4] L. B. Lovat, K. Johnson, G. D. Mackenzie, B. R. Clark, M. R. Novelli, S. Davies, M. O'Donovan, C. Selvasekar*, et al.*, "Elastic scattering spectroscopy accurately detects high grade dysplasia and cancer in barrett's oesophagus," *Gut,* vol. 55, pp. 1078-1083, 2006.

[5] L. T. Perelman, "Optical diagnostic technology based on light scattering spectroscopy for early cancer detection," *Expert Review of Medical Devices,* vol. 3, pp. 787-803, 2006.

[6] I. M. Orfanoudaki, G. C. Themelis, S. K. Sifakis, D. H. Fragouli, J. G. Panayiotides, E. M. Vazgiouraki, and E. E. Koumantakis, "A clinical study of optical biopsy of the uterine cervix using a multispectral imaging system," *Gynecol Oncol,* vol. 96, pp. 119-31, 2005.

[7] W. K. Huh, R. M. Cestero, F. A. Garcia, M. A. Gold, R. S. Guido, K. McIntyre-Seltman, D. M. Harper, L. Burke*, et al.*, "Optical detection of high-grade cervical intraepithelial neoplasia *in vivo*: Results of a 604-patient study," *Am J Obstet Gynecol,* vol. 190, pp. 1249-57, 2004.

[8] P. Arrazola, N. A. Mullani, and W. Abramovits, "Dermlite ii: An innovative portable instrument for dermoscopy without the need of immersion fluids," *Skinmed,* vol. 4, pp. 78-83, 2005.

[9] S. Brand, J. M. Poneros, B. E. Bouma, G. J. Tearney, C. C. Compton, and N. S. Nishioka, "Optical coherence tomography in the gastrointestinal tract," *Endoscopy,* vol. 32, pp. 796-803, 2000.

[10] R. S. DaCosta, B. C. Wilson, and N. E. Marcon, "Optical techniques for the endoscopic detection of dysplastic colonic lesions," *Curr Opin Gastroenterol,* vol. 21, pp. 70-9, 2005.

[11] M. L. James, and S. S. Gambhir, "A molecular imaging primer: Modalities, imaging agents, and applications," *Physiol Rev,* vol. 92, pp. 897-965, 2012.

[12] K. N. Prasad, W. C. Cole, and G. M. Hasse, "Health risks of low dose ionizing radiation in humans: A review," *Exp Biol Med (Maywood),* vol. 229, pp. 378-82, 2004.

[13] C. A. Roobottom, G. Mitchell, and G. Morgan-Hughes, "Radiation-reduction strategies in cardiac computed tomographic angiography," *Clinical Radiology,* vol. 65, pp. 859-867, 2010.
[14] J. V. Frangioni, "New technologies for human cancer imaging," *Journal of Clinical Oncology,* vol. 26, pp. 4012-4021, 2008.
[15] R. A. Kruger, "Photoacoustic ultrasound," *Medical Physics,* vol. 21, pp. 127-31, 1994.
[16] C. G. Hoelen, F. F. de Mul, R. Pongers, and A. Dekker, "Three-dimensional photoacoustic imaging of blood vessels in tissue," *Optics Letters,* vol. 23, pp. 648-50, 1998.
[17] X. Yang, S. E. Skrabalak, Z. Y. Li, Y. Xia, and L. V. Wang, "Photoacoustic tomography of a rat cerebral cortex *in vivo* with au nanocages as an optical contrast agent," *Nano Letters,* vol. 7, pp. 3798-3802, 2007.
[18] B. Wang, E. Yantsen, T. Larson, A. B. Karpiouk, S. Sethuraman, J. L. Su, K. Sokolov, and S. Y. Emelianov, "Plasmonic intravascular photoacoustic imaging for detection of macrophages in atherosclerotic plaques," *Nano Letters,* vol. 9, pp. 2212-2217, 2009.
[19] D. Pan, M. Pramanik, A. Senpan, S. Ghosh, S. A. Wickline, L. V. Wang, and G. M. Lanza, "Near infrared photoacoustic detection of sentinel lymph nodes with gold nanobeacons," *Biomaterials,* vol. 31, pp. 4088-93, 2010.
[20] J. V. Jokerst, M. Thangaraj, P. J. Kempen, R. Sinclair, and S. S. Gambhir, "Photoacoustic imaging of mesenchymal stem cells in living mice via silica-coated gold nanorods," *ACS Nano,* vol. 6, pp. 5920-30, 2012.
[21] C. Kim, S. Park, J. Kim, S. Lee, C. Lee, M. Jeon, and K. Oh, "Objective-free optical-resolution photoacoustic microscopy," *J Biomed Opt,* vol. 18, p. 10501, 2013.
[22] C. Li, and L. V. Wang, "Photoacoustic tomography and sensing in biomedicine," *Phys Med Biol,* vol. 54, pp. R59-97, 2009.
[23] S. Zackrisson, S. M. van de Ven, and S. S. Gambhir, "Light in and sound out: Emerging translational strategies for photoacoustic imaging," *Cancer Res,* vol. 74, pp. 979-1004, 2014.
[24] H. W. Kroto, J. R. Heath, S. O'Brien, R. F. Curl, and R. E. Smalley, "C60: Buckminsterfullerene," *Nature,* vol. 318, pp. 162-163, 1985.
[25] S. Iijima, "Helical microtubules of graphitic carbon," *Nature,* vol. 354, pp. 56-58, 1991.
[26] D. W. Cagle, S. J. Kennel, S. Mirzadeh, J. M. Alford, and L. J. Wilson, "*In vivo* studies of fullerene-based materials using endohedral metallofullerene radiotracers," *Proc Natl Acad Sci U S A,* vol. 96, pp. 5182-7, 1999.
[27] R. D. Bolskar, A. F. Benedetto, L. O. Husebo, R. E. Price, E. F. Jackson, S. Wallace, L. J. Wilson, and J. M. Alford, "First soluble m@c60 derivatives provide enhanced access to metallofullerenes and permit *in vivo* evaluation of gd@c60[c(cooh)2]10 as a mri contrast agent," *Journal of the American Chemical Society,* vol. 125, pp. 5471-5478, 2003.

[28] H. Gong, R. Peng, and Z. Liu, "Carbon nanotubes for biomedical imaging: The recent advances," *Adv Drug Deliv Rev,* vol. 65, pp. 1951-63, 2013.
[29] K. Welsher, L. Zhuang, S. P. Sherlock, J. T. Robinson, C. Zhuo, D. Daranciang, and D. Hongjie, "A route to brightly fluorescent carbon nanotubes for near-infrared imaging in mice," *Nature Nanotechnology,* vol. 4, pp. 773-780, 2009.
[30] S. Diao, G. Hong, J. T. Robinson, L. Jiao, A. L. Antaris, J. Z. Wu, C. L. Choi, and H. Dai, "Chirality enriched (12,1) and (11,3) single-walled carbon nanotubes for biological imaging," *Journal of the American Chemical Society,* vol. 134, pp. 16971-16974, 2012.
[31] J. W. Kang, F. T. Nguyen, N. Lue, R. R. Dasari, and D. A. Heller, "Measuring uptake dynamics of multiple identifiable carbon nanotube species via high-speed confocal raman imaging of live cells," *Nano Letters,* vol. 12, pp. 6170-6174, 2012.
[32] J. H. Choi, F. T. Nguyen, P. W. Barone, D. A. Heller, A. E. Moll, D. Patel, S. A. Boppart, and M. S. Strano, "Multimodal biomedical imaging with asymmetric single-walled carbon nanotube/iron oxide nanoparticle complexes," *Nano Letters,* vol. 7, pp. 861-867, 2007.
[33] A. Al Faraj, K. Cieslar, G. Lacroix, S. Gaillard, E. Canet-Soulas, and Y. Crémillieux, "*In vivo* imaging of carbon nanotube biodistribution using magnetic resonance imaging," *Nano Letters,* vol. 9, pp. 1023-1027, 2009.
[34] O. Vittorio, S. L. Duce, A. Pietrabissa, and A. Cuschieri, "Multiwall carbon nanotubes as mri contrast agents for tracking stem cells," *Nanotechnology,* vol. 22, p. 095706, 2011.
[35] Z. Liu, W. Cai, L. He, N. Nakayama, K. Chen, X. Sun, X. Chen, and H. Dai, "*In vivo* biodistribution and highly efficient tumour targeting of carbon nanotubes in mice," *Nat Nanotechnol,* vol. 2, pp. 47-52, 2007.
[36] M. R. McDevitt, D. Chattopadhyay, J. S. Jaggi, R. D. Finn, P. B. Zanzonico, C. Villa, D. Rey, J. Mendenhall*, et al.*, "Pet imaging of soluble yttrium-86-labeled carbon nanotubes in mice," *PLoS One,* vol. 2, p. e907, 2007.
[37] M. R. McDevitt, D. Chattopadhyay, B. J. Kappel, J. S. Jaggi, S. R. Schiffman, C. Antczak, J. T. Njardarson, R. Brentjens*, et al.*, "Tumor targeting with antibody-functionalized, radiolabeled carbon nanotubes," *Journal of Nuclear Medicine,* vol. 48, pp. 1180-1189, 2007.
[38] S. Y. Hong, G. Tobias, K. T. Al-Jamal, B. Ballesteros, H. Ali-Boucetta, S. Lozano-Perez, P. D. Nellist, R. B. Sim*, et al.*, "Filled and glycosylated carbon nanotubes for *in vivo* radioemitter localization and imaging," *Nat Mater,* vol. 9, pp. 485-90, 2010.
[39] J. W. Kim, E. I. Galanzha, E. V. Shashkov, H. M. Moon, and V. P. Zharov, "Golden carbon nanotubes as multimodal photoacoustic and photothermal high-contrast molecular agents," *Nat Nanotechnol,* vol. 4, pp. 688-94, 2009.
[40] I. G. Ekaterina, V. S. Evgeny, K. Thomas, K. Jin-Woo, Y. Lily, and P. Z. Vladimir, "*In vivo* magnetic enrichment and multiplex photoacoustic detection of circulating tumour cells," *Nature Nanotechnology,* vol. 4, pp. 855-860, 2009.

[41] A. d. l. Zerda, Z. Liu, S. Bodapati, R. Teed, S. Vaithilingam, B. T. Khuri-Yakub, X. Chen, H. Dai*, et al.*, "Ultrahigh sensitivity carbon nanotube agents for photoacoustic molecular imaging in living mice," *Nano Letters,* vol. 10, pp. 2168-2172, 2010.

[42] A. de la Zerda, S. Bodapati, R. Teed, S. Y. May, S. M. Tabakman, Z. Liu, B. T. Khuri-Yakub, X. Chen*, et al.*, "Family of enhanced photoacoustic imaging agents for high-sensitivity and multiplexing studies in living mice," *ACS Nano,* vol. 6, pp. 4694-4701, 2012.

[43] P. K. Avti, S. Hu, C. Favazza, A. G. Mikos, J. A. Jansen, K. R. Shroyer, L. V. Wang, and B. Sitharaman, "Detection, mapping, and quantification of single walled carbon nanotubes in histological specimens with photoacoustic microscopy," *PLoS One,* vol. 7, p. e35064, 2012.

[44] L. Wu, X. Cai, K. Nelson, W. Xing, J. Xia, R. Zhang, A. Stacy, M. Luderer*, et al.*, "A green synthesis of carbon nanoparticles from honey and their use in real-time photoacoustic imaging," *Nano Research,* vol. 6, pp. 312-325, 2013.

[45] P. Rajagopalan, F. Wudl, R. F. Schinazi, and F. D. Boudinot, "Pharmacokinetics of a water-soluble fullerene in rats," *Antimicrob Agents Chemother,* vol. 40, pp. 2262-5, 1996.

[46] M. L. Schipper, N. Nakayama-Ratchford, C. R. Davis, N. W. Kam, P. Chu, Z. Liu, X. Sun, H. Dai*, et al.*, "A pilot toxicology study of single-walled carbon nanotubes in a small sample of mice," *Nat Nanotechnol,* vol. 3, pp. 216-21, 2008.

[47] K. Kostarelos, A. Bianco, and M. Prato, "Promises, facts and challenges for carbon nanotubes in imaging and therapeutics," *Nat Nanotechnol,* vol. 4, pp. 627-33, 2009.

[48] Y. Zhang, J. Deng, F. Guo, C. Li, Z. Zou, W. Xi, J. Tang, Y. Sun*, et al.*, "Functionalized single-walled carbon nanotubes cause reversible acute lung injury and induce fibrosis in mice," *J Mol Med (Berl),* vol. 91, pp. 117-28, 2013.

[49] C. A. Poland, R. Duffin, I. Kinloch, A. Maynard, W. A. Wallace, A. Seaton, V. Stone, S. Brown*, et al.*, "Carbon nanotubes introduced into the abdominal cavity of mice show asbestos-like pathogenicity in a pilot study," *Nat Nanotechnol,* vol. 3, pp. 423-8, 2008.

[50] S. Yamago, H. Tokuyama, E. Nakamura, K. Kikuchi, S. Kananishi, K. Sueki, H. Nakahara, S. Enomoto*, et al.*, "*In vivo* biological behavior of a water-miscible fullerene: 14c labeling, absorption, distribution, excretion and acute toxicity," *Chem Biol,* vol. 2, pp. 385-9, 1995.

[51] C. J. Murphy, and J. L. Coffer, "Quantum dots: A primer," *Applied Spectroscopy,* vol. 56, pp. 16A-27A, 2002.

[52] A. L. Efros, "Interband absorption of light in a semiconductor sphere," *Soviet Physics Semiconductors-Ussr,* vol. 16, pp. 772-775, 1982.

[53] A. I. Ekimov, A. L. Efros, and A. A. Onushchenko, "Quantum size effect in semiconductor microcrystals," *Solid State Communications,* vol. 56, pp. 921-924, 1985.

[54] M. Bruchez, Jr., M. Moronne, P. Gin, S. Weiss, and A. P. Alivisatos, "Semiconductor nanocrystals as fluorescent biological labels," *Science (Washington, D. C.),* vol. 281, pp. 2013-2016, 1998.
[55] W. C. Chan, and S. Nie, "Quantum dot bioconjugates for ultrasensitive nonisotopic detection," *Science,* vol. 281, pp. 2016-8., 1998.
[56] E. Petryayeva, W. R. Algar, and I. L. Medintz, "Quantum dots in bioanalysis: A review of applications across various platforms for fluorescence spectroscopy and imaging," *Applied Spectroscopy,* vol. 67, pp. 215-252, 2013.
[57] F. E. Wagner, S. Haslbeck, L. Stievano, S. Calogero, Q. A. Pankhurst, and K. P. Martinek, "Before striking gold in gold-ruby glass," *Nature,* vol. 407, pp. 691-2, 2000.
[58] M. Knoll, and E. Ruska, "The electron microscope," *Z. Physik,* vol. 78, pp. 318-339, 1932.
[59] J. Turkevich, and J. Hillier, "Electron microscopy of colloidal systems," *Analytical Chemistry,* vol. 21, pp. 475-485, 1949.
[60] V. V. Mody, R. Siwale, A. Singh, and H. R. Mody, "Introduction to metallic nanoparticles," *J Pharm Bioallied Sci,* vol. 2, pp. 282-9, 2010.
[61] S. Shukla, A. Priscilla, M. Banerjee, R. R. Bhonde, J. Ghatak, P. V. Satyam, and M. Sastry, "Porous gold nanospheres by controlled transmetalation reaction: A novel material for application in cell imaging," *Chemistry of Materials,* vol. 17, pp. 5000-5005, 2005.
[62] Z. H. Kim, and S. R. Leone, "High-resolution apertureless near-field optical imaging using gold nanosphere probes," *Journal of Physical Chemistry B,* vol. 110, pp. 19804-19809, 2006.
[63] M. C. Skala, M. J. Crow, A. Wax, and J. A. Izatt, "Photothermal optical coherence tomography of epidermal growth factor receptor in live cells using immunotargeted gold nanospheres," *Nano Letters,* vol. 8, pp. 3461-3467, 2008.
[64] S. Mallidi, T. Larson, J. Tam, P. P. Joshi, A. Karpiouk, K. Sokolov, and S. Emelianov, "Multiwavelength photoacoustic imaging and plasmon resonance coupling of gold nanoparticles for selective detection of cancer," *Nano Letters,* vol. 9, pp. 2825-2831, 2009.
[65] W. Lu, G. Zhang, R. Zhang, L. G. Flores, Q. Huang, J. G. Gelovani, and C. Li, "Tumor site–specific silencing of nf-κb p65 by targeted hollow gold nanosphere–mediated photothermal transfection," *Cancer Research,* vol. 70, pp. 3177-3188, 2010.
[66] L. R. Hirsch, R. J. Stafford, J. A. Bankson, S. R. Sershen, B. Rivera, R. E. Price, J. D. Hazle, N. J. Halas*, et al.*, "Nanoshell-mediated near-infrared thermal therapy of tumors under magnetic resonance guidance," *Proceedings of the National Academy of Sciences of the United States of America,* vol. 100, pp. 13549-13554, 2003.
[67] C. Loo, A. Lin, L. Hirsch, M.-H. Lee, J. Barton, N. Halas, J. West, and R. Drezek, "Nanoshell-enabled photonics-based imaging and therapy of cancer," *Technology in cancer research & treatment,* vol. 3, pp. 33-40, 2004.

[68] J. M. Stern, J. Stanfield, W. Kabbani, J.-T. Hsieh, and J. A. Cadeddu, "Selective prostate cancer thermal ablation with laser activated gold nanoshells," *The Journal of Urology,* vol. 179, pp. 748-753, 2008.
[69] S. K. Baek, A. R. Makkouk, T. Krasieva, C. H. Sun, S. J. Madsen, and H. Hirschberg, "Photothermal treatment of glioma; an *in vitro* study of macrophage-mediated delivery of gold nanoshells," *J Neurooncol,* 2011.
[70] J. Chen, D. Wang, J. Xi, L. Au, A. Siekkinen, A. Warsen, Z.-Y. Li, H. Zhang*, et al.*, "Immuno gold nanocages with tailored optical properties for targeted photothermal destruction of cancer cells," *Nano Letters,* vol. 7, pp. 1318-1322, 2007.
[71] K. H. Song, C. Kim, C. M. Cobley, Y. Xia, and L. V. Wang, "Near-infrared gold nanocages as a new class of tracers for photoacoustic sentinel lymph node mapping on a rat model," *Nano Lett,* vol. 9, pp. 183-8, 2009.
[72] Y. Xia, W. Li, C. M. Cobley, J. Chen, X. Xia, Q. Zhang, M. Yang, E. C. Cho*, et al.*, "Gold nanocages: From synthesis to theranostic applications," *Accounts of Chemical Research,* vol. 44, pp. 914-924, 2011.
[73] K. Imura, T. Nagahara, and H. Okamoto, "Plasmon mode imaging of single gold nanorods," *Journal of the American Chemical Society,* vol. 126, pp. 12730-12731, 2004.
[74] H. Wang, T. B. Huff, D. A. Zweifel, W. He, P. S. Low, A. Wei, and J.-X. Cheng, "*In vitro* and *in vivo* two-photon luminescence imaging of single gold nanorods," *Proceedings of the National Academy of Sciences of the United States of America,* vol. 102, pp. 15752-15756, 2005.
[75] A. Wei, Q. Wei, and A. P. Leonov, "Gold nanorods as theranostic agents," in *Nanoplatform-based molecular imaging*, ed: John Wiley & Sons, Inc., 2011, pp. 659-681.
[76] C. L. Bayer, Y.-S. Chen, S. Kim, S. Mallidi, K. Sokolov, and S. Emelianov, "Multiplex photoacoustic molecular imaging using targeted silica-coated gold nanorods," *Biomed. Opt. Express,* vol. 2, pp. 1828-1835, 2011.
[77] J. Choi, J. Yang, D. Bang, J. Park, J. S. Suh, Y. M. Huh, and S. Haam, "Targetable gold nanorods for epithelial cancer therapy guided by near-ir absorption imaging," *Small,* vol. 8, pp. 746-53, 2012.
[78] P. K. Jain, K. S. Lee, I. H. El-Sayed, and M. A. El-Sayed, "Calculated absorption and scattering properties of gold nanoparticles of different size, shape, and composition: Applications in biological imaging and biomedicine," *Journal of Physical Chemistry B,* vol. 110, pp. 7238-7248, 2006.
[79] M. Hu, J. Chen, Z.-Y. Li, L. Au, G. V. Hartland, X. Li, M. Marquez, and Y. Xia, "Gold nanostructures: Engineering their plasmonic properties for biomedical applications," *Chemical Society Reviews,* vol. 35, pp. 1084-1094, 2006.
[80] G. Bao, S. Mitragotri, and S. Tong, "Multifunctional nanoparticles for drug delivery and molecular imaging," *Annu Rev Biomed Eng,* vol. 15, pp. 253-82, 2013.

[81] S. Stolik, J. A. Delgado, A. Pérez, and L. Anasagasti, "Measurement of the penetration depths of red and near infrared light in human "*ex vivo*" tissues," *Journal of Photochemistry and Photobiology B: Biology,* vol. 57, pp. 90-93, 2000.
[82] J. T. Robinson, K. Welsher, S. M. Tabakman, S. P. Sherlock, H. Wang, R. Luong, and H. Dai, "High performance *in vivo* near-ir (>1 mum) imaging and photothermal cancer therapy with carbon nanotubes," *Nano Res,* vol. 3, pp. 779-793, 2010.
[83] D. Fried, M. Staninec, C. L. Darling, C. Lee, H. Kang, and K. H. Chan, "*In vivo* near-ir imaging of occlusal lesions at 1310-nm," *Proc Soc Photo Opt Instrum Eng,* vol. 7884, 2011.
[84] M. Xu, and L. V. Wang, "Photoacoustic imaging in biomedicine," *Rev. Sci. Instrum,* vol. 77, p. 041101, 2006.
[85] G. J. Nusz, S. M. Marinakos, A. C. Curry, A. Dahlin, F. Hook, A. Wax, and A. Chilkoti, "Label-free plasmonic detection of biomolecular binding by a single gold nanorod," *Analytical Chemistry,* vol. 80, pp. 984-989, 2008.
[86] X. Huang, S. Neretina, and M. A. El-Sayed, "Gold nanorods: From synthesis and properties to biological and biomedical applications," *Advanced Materials,* vol. 21, pp. 4880-4910, 2009.
[87] L. Tong, Q. Wei, A. Wei, and J.-X. Cheng, "Gold nanorods as contrast agents for biological imaging: Optical properties, surface conjugation and photothermal effects," *Photochemistry and Photobiology,* vol. 85, pp. 21-32, 2009.
[88] C. Yu, and J. Irudayaraj, "Multiplex biosensor using gold nanorods," *Analytical Chemistry,* vol. 79, pp. 572-579, 2007.
[89] N. J. Durr, T. Larson, D. K. Smith, B. A. Korgel, K. Sokolov, and A. Ben-Yakar, "Two-photon luminescence imaging of cancer cells using molecularly targeted gold nanorods," *Nano Letters,* vol. 7, pp. 941-945, 2007.
[90] A. Agarwal, S. W. Huang, M. O'Donnell, K. C. Day, M. Day, N. Kotov, and S. Ashkenazi, "Targeted gold nanorod contrast agent for prostate cancer detection by photoacoustic imaging," *Journal of Applied Physics,* vol. 102, pp. 064701-1, 2007.
[91] H. Cui, and X. Yang, "*In vivo* imaging and treatment of solid tumor using integrated photoacoustic imaging and high intensity focused ultrasound system " *Medical Physics,* vol. 37, pp. 4777-4781, 2010.
[92] S. Mallidi, G. P. Luke, and S. Emelianov, "Photoacoustic imaging in cancer detection, diagnosis, and treatment guidance," *Trends in Biotechnology,* vol. 29, pp. 213-221, 2011.
[93] X. Huang, I. H. El-Sayed, W. Qian, and M. A. El-Sayed, "Cancer cell imaging and photothermal therapy in the near-infrared region by using gold nanorods," *Journal of the American Chemical Society,* vol. 128, pp. 2115-2120, 2006.
[94] J. Shah, S. Park, S. Aglyamov, T. Larson, L. Ma, K. Sokolov, K. Johnston, T. E. Milner*, et al.*, "Photoacoustic imaging and temperature measurement for photothermal cancer therapy," *J. Biomed. Opt.,* vol. 13, p. 034024, 2008.

[95] E. B. Dickerson, E. C. Dreaden, X. Huang, I. H. El-Sayed, H. Chu, S. Pushpanketh, J. F. McDonald, and M. A. El-Sayed, "Gold nanorod assisted near-infrared plasmonic photothermal therapy (pptt) of squamous cell carcinoma in mice," *Cancer Letters,* vol. 269, pp. 57-66, 2008.
[96] X. Huang, I. H. El-Sayed, W. Qian, and M. A. El-Sayed, "Cancer cells assemble and align gold nanorods conjugated to antibodies to produce highly enhanced, sharp, and polarized surface raman spectra: A potential cancer diagnostic marker," *Nano Letters,* vol. 7, pp. 1591-1597, 2007.
[97] K. Sokolov, K.-B. Sung, T. Collier, A. Clark, D. Arifler, A. Lacy, M. Descour, and R. Richards-Kortum, "Endoscopic microscopy," *Disease markers,* vol. 18, pp. 269-91., 2002.
[98] L. Clark Anne, M. Gillenwater Ann, G. Collier Thomas, R. Alizadeh-Naderi, K. El-Naggar Adel, and R. Richards-Kortum Rebecca, "Confocal microscopy for real-time detection of oral cavity neoplasia," *Clinical cancer research : an official journal of the American Association for Cancer Research,* vol. 9, pp. 4714-21., 2003.
[99] K. Basen-Engquist, H. Shinn Eileen, C. Warneke, C. de Moor, T. Le, R. Richards-Kortum, and M. Follen, "Patient distress and satisfaction with optical spectroscopy in cervical dysplasia detection," *American journal of obstetrics and gynecology,* vol. 189, pp. 1136-42., 2003.
[100] A. M. Fowler, "A molecular approach to breast imaging," *Journal of Nuclear Medicine,* vol. 55, pp. 177-180, 2014.
[101] R. M. Sharkey, and D. M. Goldenberg, "Perspectives on cancer therapy with radiolabeled monoclonal antibodies," *J Nucl Med,* vol. 46 Suppl 1, pp. 115S-27S, 2005.
[102] M. E. Davis, "The first targeted delivery of sirna in humans via a self-assembling, cyclodextrin polymer-based nanoparticle: From concept to clinic," *Molecular Pharmaceutics,* vol. 6, pp. 659-668, 2009.
[103] Y. Matsumura, M. Gotoh, K. Muro, Y. Yamada, K. Shirao, Y. Shimada, M. Okuwa, S. Matsumoto*, et al.*, "Phase i and pharmacokinetic study of mcc-465, a doxorubicin (dxr) encapsulated in peg immunoliposome, in patients with metastatic stomach cancer," *Ann Oncol,* vol. 15, pp. 517-25, 2004.
[104] M. K. Yu, J. Park, and S. Jon, "Targeting strategies for multifunctional nanoparticles in cancer imaging and therapy," *Theranostics,* vol. 2, pp. 3-44, 2012.
[105] D. Peer, J. M. Karp, S. Hong, O. C. Farokhzad, R. Margalit, and R. Langer, "Nanocarriers as an emerging platform for cancer therapy," *Nat Nanotechnol,* vol. 2, pp. 751-60, 2007.
[106] C. Alric, J. Taleb, G. Le Duc, C. Mandon, C. Billotey, A. Le Meur-Herland, T. Brochard, F. Vocanson*, et al.*, "Gadolinium chelate coated gold nanoparticles as contrast agents for both x-ray computed tomography and magnetic resonance imaging," *J Am Chem Soc,* vol. 130, pp. 5908-15, 2008.

[107] M. M. van Schooneveld, D. P. Cormode, R. Koole, J. T. van Wijngaarden, C. Calcagno, T. Skajaa, J. Hilhorst, D. C. t Hart*, et al.*, "A fluorescent, paramagnetic and pegylated gold/silica nanoparticle for mri, ct and fluorescence imaging," *Contrast Media Mol Imaging,* vol. 5, pp. 231-6, 2010.
[108] A. J. Mieszawska, W. J. Mulder, Z. A. Fayad, and D. P. Cormode, "Multifunctional gold nanoparticles for diagnosis and therapy of disease," *Mol Pharm,* vol. 10, pp. 831-47, 2013.
[109] I. H. El-Sayed, X. Huang, and M. A. El-Sayed, "Surface plasmon resonance scattering and absorption of anti-egfr antibody conjugated gold nanoparticles in cancer diagnostics: Applications in oral cancer," *Nano Letters,* vol. 5, pp. 829-834, 2005.
[110] D. P. Cormode, T. Skajaa, M. M. van Schooneveld, R. Koole, P. Jarzyna, M. E. Lobatto, C. Calcagno, A. Barazza*, et al.*, "Nanocrystal core high-density lipoproteins: A multimodality contrast agent platform," *Nano Lett,* vol. 8, pp. 3715-23, 2008.
[111] S. C. Tang, Y. Y. Fu, W. F. Lo, T. E. Hua, and H. Y. Tuan, "Vascular labeling of luminescent gold nanorods enables 3-d microscopy of mouse intestinal capillaries," *ACS Nano,* vol. 4, pp. 6278-84, 2010.
[112] J. F. Hainfeld, M. J. O'Connor, F. A. Dilmanian, D. N. Slatkin, D. J. Adams, and H. M. Smilowitz, "Micro-ct enables microlocalisation and quantification of her2-targeted gold nanoparticles within tumour regions," *Br J Radiol,* vol. 84, pp. 526-33, 2011.
[113] D. N. Heo, D. H. Yang, H. J. Moon, J. B. Lee, M. S. Bae, S. C. Lee, W. J. Lee, I. C. Sun*, et al.*, "Gold nanoparticles surface-functionalized with paclitaxel drug and biotin receptor as theranostic agents for cancer therapy," *Biomaterials,* vol. 33, pp. 856-66, 2012.
[114] A. Kumar, H. Ma, X. Zhang, K. Huang, S. Jin, J. Liu, T. Wei, W. Cao*, et al.*, "Gold nanoparticles functionalized with therapeutic and targeted peptides for cancer treatment," *Biomaterials,* vol. 33, pp. 1180-9, 2012.
[115] P. P. Joshi, S. J. Yoon, W. G. Hardin, S. Emelianov, and K. V. Sokolov, "Conjugation of antibodies to gold nanorods through fc portion: Synthesis and molecular specific imaging," *Bioconjugate Chemistry,* vol. 24, pp. 878-888, 2013.
[116] S. K. Libutti, G. F. Paciotti, A. A. Byrnes, H. R. Alexander, Jr., W. E. Gannon, M. Walker, G. D. Seidel, N. Yuldasheva*, et al.*, "Phase i and pharmacokinetic studies of cyt-6091, a novel pegylated colloidal gold-rhtnf nanomedicine," *Clin Cancer Res,* vol. 16, pp. 6139-49, 2010.
[117] M. M. Bednar, and A. Perry, "Neurorestoration therapeutics for neurodegenerative and psychiatric disease," *Neurol Res,* vol. 34, pp. 129-42, 2012.
[118] I. J. de Vries, W. J. Lesterhuis, J. O. Barentsz, P. Verdijk, J. H. van Krieken, O. C. Boerman, W. J. Oyen, J. J. Bonenkamp*, et al.*, "Magnetic resonance tracking of dendritic cells in melanoma patients for monitoring of cellular therapy," *Nat Biotechnol,* vol. 23, pp. 1407-13, 2005.

[119] C. M. Long, and J. W. Bulte, "*In vivo* tracking of cellular therapeutics using magnetic resonance imaging," *Expert Opin Biol Ther,* vol. 9, pp. 293-306, 2009.
[120] D. P. Cormode, E. Roessl, A. Thran, T. Skajaa, R. E. Gordon, J. P. Schlomka, V. Fuster, E. A. Fisher*, et al.*, "Atherosclerotic plaque composition: Analysis with multicolor ct and targeted gold nanoparticles," *Radiology,* vol. 256, pp. 774-82, 2010.
[121] R. H. Menk, E. Schultke, C. Hall, F. Arfelli, A. Astolfo, L. Rigon, A. Round, K. Ataelmannan*, et al.*, "Gold nanoparticle labeling of cells is a sensitive method to investigate cell distribution and migration in animal models of human disease," *Nanomedicine,* vol. 7, pp. 647-54, 2011.
[122] M. M. Welling, M. Duijvestein, A. Signore, and L. van der Weerd, "*In vivo* biodistribution of stem cells using molecular nuclear medicine imaging," *J Cell Physiol,* vol. 226, pp. 1444-52, 2011.
[123] B. N. Park, W. Shim, G. Lee, O. Y. Bang, Y. S. An, J. K. Yoon, and Y. H. Ahn, "Early distribution of intravenously injected mesenchymal stem cells in rats with acute brain trauma evaluated by (99m)tc-hmpao labeling," *Nucl Med Biol,* vol. 38, pp. 1175-82, 2011.
[124] E. Barbarese, S. Y. Ho, J. S. D'Arrigo, and R. H. Simon, "Internalization of microbubbles by tumor cells *in vivo* and *in vitro*," *J Neurooncol,* vol. 26, pp. 25-34, 1995.
[125] M. A. Kuliszewski, H. Fujii, C. Liao, A. H. Smith, A. Xie, J. R. Lindner, and H. Leong-Poi, "Molecular imaging of endothelial progenitor cell engraftment using contrast-enhanced ultrasound and targeted microbubbles," *Cardiovasc Res,* vol. 83, pp. 653-62, 2009.
[126] J. Li, X. Chang, X. Chen, Z. Gu, F. Zhao, Z. Chai, and Y. Zhao, "Toxicity of inorganic nanomaterials in biomedical imaging," *Biotechnol Adv,* 2014.
[127] W. H. D. Jong, W. I. Hagens, P. Krystek, M. C. Burger, A. J. A. M. Sips, and R. E. Geertsma, "Particle size-dependent organ distribution of gold nanoparticles after intravenous adminostration," *Biomaterials,* vol. 29, pp. 1912-1919, 2008.
[128] Q. Zhang, V. M. Hitchins, A. M. Schrand, S. M. Hussain, and P. L. Goering, "Uptake of gold nanoparticles in murine macrophage cells without cytotoxicity or production of pro-inflammatory mediators," *Nanotoxicology,* vol. 5, pp. 284-95, 2011.
[129] H. Yang, C. Sun, Z. Fan, X. Tian, L. Yan, L. Du, Y. Liu, C. Chen*, et al.*, "Effects of gestational age and surface modification on materno-fetal transfer of nanoparticles in murine pregnancy," *Sci Rep,* vol. 2, p. 847, 2012.
[130] H. S. Choi, W. Liu, P. Misra, E. Tanaka, J. P. Zimmer, B. Itty Ipe, M. G. Bawendi, and J. V. Frangioni, "Renal clearance of quantum dots," *Nat Biotech,* vol. 25, pp. 1165-1170, 2007.
[131] X. D. Zhang, D. Wu, X. Shen, P. X. Liu, F. Y. Fan, and S. J. Fan, "*In vivo* renal clearance, biodistribution, toxicity of gold nanoclusters," *Biomaterials,* vol. 33, pp. 4628-38, 2012.

[132] N. Khlebtsov, and L. Dykman, "Biodistribution and toxicity of engineered gold nanoparticles: A review of *in vitro* and *in vivo* studies," *Chemical Society Reviews,* vol. 40, pp. 1647-1671, 2011.
[133] E. Sadauskas, G. Danscher, M. Stoltenberg, U. Vogel, A. Larsen, and H. Wallin, "Protracted elimination of gold nanoparticles from mouse liver," *Nanomedicine,* vol. 5, pp. 162-9, 2009.
[134] S. K. Balasubramanian, J. Jittiwat, J. Manikandan, C. N. Ong, L. E. Yu, and W. Y. Ong, "Biodistribution of gold nanoparticles and gene expression changes in the liver and spleen after intravenous administration in rats," *Biomaterials,* vol. 31, pp. 2034-42, 2010.
[135] R. Shukla, V. Bansal, M. Chaudhary, A. Basu, R. R. Bhonde, and M. Sastry, "Biocompatibility of gold nanoparticles and their endocytotic fate inside the cellular compartment: A microscopic overview," *Langmuir,* vol. 21, pp. 10644-10654, 2005.
[136] P. P. Joshi, S. J. Yoon, Y. S. Chen, S. Emelianov, and K. V. Sokolov, "Development and optimization of near-ir contrast agents for immune cell tracking," *Biomed Opt Express,* vol. 4, pp. 2609-18, 2013.
[137] J. Tam, J. Tam, A. Murthy, D. Ingram, L. Ma, K. Travis, K. Johnston, and K. Sokolov, "Controlled assembly of biodegradable plasmonic nanoclusters for near-infrared imaging and therapeutic applications," *ACS Nano,* vol. 4, pp. 2178-2184, 2010.
[138] A. K. Murthy, R. J. Stover, A. U. Borwankar, G. D. Nie, S. Gourisankar, T. M. Truskett, K. V. Sokolov, and K. P. Johnston, "Equilibrium gold nanoclusters quenched with biodegradable polymers," *ACS Nano,* vol. 7, pp. 239-251, 2013.
[139] S. J. Yoon, S. Mallidi, J. M. Tam, J. O. Tam, A. Murthy, K. P. Johnston, K. V. Sokolov, and S. Y. Emelianov, "Utility of biodegradable plasmonic nanoclusters in photoacoustic imaging," *Opt Lett,* vol. 35, pp. 3751-3, 2010.
[140] B. D. Chithrani, and W. C. W. Chan, "Elucidating the mechanism of cellular uptake and removal of protein-coated gold nanoparticles of different sizes and shapes," *Nano Letters,* vol. 7, pp. 1542-1550, 2007.
[141] R. E. Yanes, D. Tarn, A. A. Hwang, D. P. Ferris, S. P. Sherman, C. R. Thomas, J. Lu, A. D. Pyle*, et al.*, "Involvement of lysosomal exocytosis in the excretion of mesoporous silica nanoparticles and enhancement of the drug delivery effect by exocytosis inhibition," *Small,* vol. 9, pp. 697-704, 2013.
[142] R. E. Serda, A. Mack, A. L. van de Ven, S. Ferrati, K. Dunner, Jr., B. Godin, C. Chiappini, M. Landry*, et al.*, "Logic-embedded vectors for intracellular partitioning, endosomal escape, and exocytosis of nanoparticles," *Small,* vol. 6, pp. 2691-700, 2010.
[143] J. Panyam, and V. Labhasetwar, "Dynamics of endocytosis and exocytosis of poly(d,l-lactide-co-glycolide) nanoparticles in vascular smooth muscle cells," *Pharm Res,* vol. 20, pp. 212-20, 2003.

[144] X. Jiang, C. Rocker, M. Hafner, S. Brandholt, R. M. Dorlich, and G. U. Nienhaus, "Endo- and exocytosis of zwitterionic quantum dot nanoparticles by live hela cells," *ACS Nano,* vol. 4, pp. 6787-97, 2010.
[145] D. Bartczak, S. Nitti, T. M. Millar, and A. G. Kanaras, "Exocytosis of peptide functionalized gold nanoparticles in endothelial cells," *Nanoscale,* vol. 4, pp. 4470-2, 2012.
[146] Y. Kim, M. H. Pourgholami, D. L. Morris, H. Lu, and M. H. Stenzel, "Effect of shell-crosslinking of micelles on endocytosis and exocytosis: Acceleration of exocytosis by crosslinking," *Biomaterials Science,* vol. 1, pp. 265-275, 2013.
[147] Z. Wang, N. Li, J. Zhao, J. C. White, P. Qu, and B. Xing, "Cuo nanoparticle interaction with human epithelial cells: Cellular uptake, location, export, and genotoxicity," *Chem Res Toxicol,* vol. 25, pp. 1512-21, 2012.
[148] S. Ohta, S. Inasawa, and Y. Yamaguchi, "Real time observation and kinetic modeling of the cellular uptake and removal of silicon quantum dots," *Biomaterials,* vol. 33, pp. 4639-45, 2012.
[149] I. Stayton, J. Winiarz, K. Shannon, and Y. Ma, "Study of uptake and loss of silica nanoparticles in living human lung epithelial cells at single cell level," *Anal Bioanal Chem,* vol. 394, pp. 1595-608, 2009.
[150] M. Ekkapongpisit, A. Giovia, G. Nicotra, M. Ozzano, G. Caputo, and C. Isidoro, "Labeling and exocytosis of secretory compartments in rbl mastocytes by polystyrene and mesoporous silica nanoparticles," *Int J Nanomedicine,* vol. 7, pp. 1829-40, 2012.
[151] Slowing, II, J. L. Vivero-Escoto, Y. Zhao, K. Kandel, C. Peeraphatdit, B. G. Trewyn, and V. S. Lin, "Exocytosis of mesoporous silica nanoparticles from mammalian cells: From asymmetric cell-to-cell transfer to protein harvesting," *Small,* vol. 7, pp. 1526-32, 2011.
[152] Z. Chu, Y. Huang, Q. Tao, and Q. Li, "Cellular uptake, evolution, and excretion of silica nanoparticles in human cells," *Nanoscale,* vol. 3, pp. 3291-9, 2011.
[153] C. Y. Fang, V. Vaijayanthimala, C. A. Cheng, S. H. Yeh, C. F. Chang, C. L. Li, and H. C. Chang, "The exocytosis of fluorescent nanodiamond and its use as a long-term cell tracker," *Small,* vol. 7, pp. 3363-70, 2011.
[154] L. Hu, Z. Mao, Y. Zhang, and C. Gao, "Influences of size of silica particles on the cellular endocytosis, exocytosis and cell activity of hepg2 cells," *Journal of Nanoscience Letters,* vol. 1, pp. 1-16, 2011.
[155] M. J. Buckmaster, D. Lo Braico, Jr., A. L. Ferris, and B. Storrie, "Retention of pinocytized solute by cho cell lysosomes correlates with molecular weight," *Cell Biol Int Rep,* vol. 11, pp. 501-7, 1987.
[156] P. V. Asharani, M. P. Hande, and S. Valiyaveettil, "Anti-proliferative activity of silver nanoparticles," *BMC Cell Biol,* vol. 10, p. 65, 2009.
[157] O. Diou, N. Tsapis, and E. Fattal, "Targeted nanotheranostics for personalized cancer therapy," *Expert Opin Drug Deliv,* vol. 9, pp. 1475-87, 2012.
[158] K. Sokolov, M. Follen, J. Aaron, I. Pavlova, A. Malpica, R. Lotan, and R. Richards-Kortum, "Real-time vital optical imaging of precancer using anti-

epidermal growth factor receptor antibodies conjugated to gold nanoparticles," *Cancer Research,* vol. 63, pp. 1999-2004, 2003.
[159] K. Sokolov, J. Aaron, B. Hsu, D. Nida, A. Gillenwater, M. Follen, C. MacAulay, K. Adler-Storthz*, et al.*, "Optical systems for *in vivo* molecular imaging of cancer," *Technology in cancer research & treatment,* vol. 2, pp. 491-504, 2003.
[160] W. J. Parak, D. Gerion, T. Pellegrino, D. Zanchet, C. Micheel, S. C. Williams, R. Boudreau, M. A. Le Gros*, et al.*, "Biological applications of colloidal nanocrystals," *Nanotechnology,* vol. 14, pp. R15-R27, 2003.
[161] P. Alivisatos, "The use of nanocrystals in biological detection," *Nature Biotechnology,* vol. 22, pp. 47-52, 2004.
[162] C. Loo, A. Lowery, N. Halas, J. West, and R. Drezek, "Immunotargeted nanoshells for integrated cancer imaging and therapy," *Nano Letters,* vol. 5, pp. 709-711, 2005.
[163] K. Aslan, J. R. Lakowicz, and C. D. Geddes, "Plasmon light scattering in biology and medicine: New sensing approaches, visions and perspectives," *Current Opinion in Chemical Biology,* vol. 9, pp. 538-544, 2005.
[164] G. L. Liu, Y. Yin, S. Kunchakarra, B. Mukherjee, D. Gerion, S. D. Jett, D. G. Bear, J. W. Gray*, et al.*, "A nanoplasmonic molecular ruler for measuring nuclease activity and DNA footprinting," *Nat Nano,* vol. 1, pp. 47-52, 2006.
[165] T. A. Larson, J. Bankson, J. Aaron, and K. Sokolov, "Hybrid plasmonic magnetic nanoparticles as molecular specific agents for mri/optical imaging and photothermal therapy of cancer cells," *Nanotechnology,* vol. 18, p. 325101, 2007.
[166] S. Mallidi, T. Larson, J. Aaron, K. Sokolov, and S. Emelianov, "Molecular specific optoacoustic imaging with plasmonic nanoparticles," *Optics Express,* vol. 15, pp. 6583-6588, 2007.
[167] J. N. Anker, W. P. Hall, O. Lyandres, N. C. Shah, J. Zhao, and R. P. Van Duyne, "Biosensing with plasmonic nanosensors," *Nature Materials,* vol. 7, pp. 442-453, 2008.
[168] A. Curry, M. J. Crow, and A. Wax, "Molecular imaging of epidermal growth factor receptor in live cells with refractive index sensitivity using dark-field microspectroscopy and immunotargeted nanoparticles," *Journal of Biomedical Optics,* vol. 13, p. 014022
2008.
[169] P. K. Jain, X. Huang, I. H. El-Sayed, and M. A. El-Sayed, "Noble metals on the nanoscale: Optical and photothermal properties and some applications in imaging, sensing, biology, and medicine," *Accounts of Chemical Research,* vol. 41, pp. 1578-1586, 2008.
[170] S. E. Lee, and L. P. Lee, "Biomolecular plasmonics for quantitative biology and nanomedicine," *Current Opinion in Biotechnology,* vol. 21, pp. 489-497, 2010.
[171] N. Chanda, V. Kattumuri, R. Shukla, A. Zambre, K. Katti, A. Upendran, R. R. Kulkarni, P. Kan*, et al.*, "Bombesin functionalized gold nanoparticles show *in vitro* and *in vivo* cancer receptor specificity," *Proceedings of the National Academy of Sciences,* vol. 107, pp. 8760-8765, 2010.

[172] M. J. Crow, S. M. Marinakos, J. M. Cook, A. Chilkoti, and A. Wax, "Plasmonic flow cytometry by immunolabeled nanorods," *Cytometry Part A : Journal of the International Society for Advancement of Cytometry,* vol. 79, pp. 57-65, 2011.
[173] N. Chanda, R. Shukla, A. Zambre, S. Mekapothula, R. Kulkarni, K. Katti, K. Bhattacharyya, G. Fent*, et al.*, "An effective strategy for the synthesis of biocompatible gold nanoparticles using cinnamon phytochemicals for phantom ct imaging and photoacoustic detection of cancerous cells," *Pharmaceutical Research,* vol. 28, pp. 279-291, 2011.
[174] A. E. Prigodich, A. H. Alhasan, and C. A. Mirkin, "Selective enhancement of nucleases by polyvalent DNA-functionalized gold nanoparticles," *Journal of the American Chemical Society,* vol. 133, pp. 2120-2123, 2011.
[175] E. C. Dreaden, M. A. Mackey, X. Huang, B. Kang, and M. A. El-Sayed, "Beating cancer in multiple ways using nanogold," *Chemical Society Reviews,* vol. 40, pp. 3391-3404, 2011.
[176] S. Bharill, C. Chen, B. Stevens, J. Kaur, Z. Smilansky, W. Mandecki, I. Gryczynski, Z. Gryczynski*, et al.*, "Enhancement of single-molecule fluorescence signals by colloidal silver nanoparticles in studies of protein translation," *ACS Nano,* vol. 5, pp. 399-407, 2010.
[177] K. M. Lee, A. Neogi, P. Basu Neogi, M. Kim, B. Kim, R. Luchowski, Z. Gryczynski, N. Calander*, et al.*, "Silver nanostructure sensing platform for maximum-contrast fluorescence cell imaging," *J Biomed Opt,* vol. 16, p. 056008, 2011.
[178] P. Matteini, F. Ratto, F. Rossi, and R. Pini, "Emerging concepts of laser-activated nanoparticles for tissue bonding," *J Biomed Opt,* vol. 17, p. 010701, 2012.
[179] J. Aaron, N. Nitin, K. Travis, S. Kumar, T. Collier, S. Y. Park, M. Jose-Yacaman, L. Coghlan*, et al.*, "Imaging of epidermal growth factor receptor in early carcinogenesis using plasmon resonance coupling of metal nanoparticles.," *Journal of Biomedical Optics,* vol. 12, p. 034007, 2007.
[180] G. L. Liu, Y. Yin, S. Kunchakarra, B. Mukherjee, D. Gerion, S. D. Jett, D. G. Bear, J. W. Gray*, et al.*, "A nanoplasmonic molecular ruler for measuring nuclease activity and DNA footprinting," *Nature Nanotechnology,* vol. 1, pp. 47-52, 2006.
[181] A. Wax, and K. Sokolov, "Molecular imaging and darkfield microspectroscopy of live cells using gold plasmonic nanoparticles," *Laser & Photonics Reviews,* vol. 3, pp. 146-158, 2009.
[182] R. Mercatelli, G. Romano, F. Ratto, P. Matteini, S. Centi, F. Cialdai, M. Monici, R. Pini*, et al.*, "Quantitative measurement of scattering and extinction spectra of nanoparticles by darkfield microscopy," *Applied Physics Letters,* vol. 99, 2011.
[183] J. Park, A. Estrada, K. Sharp, K. Sang, J. A. Schwartz, D. K. Smith, C. Coleman, J. D. Payne*, et al.*, "Two-photon-induced photoluminescence imaging of tumors using near-infrared excited gold nanoshells," *Opt. Express,* vol. 16, pp. 1590-1599, 2008.

[184] A. A. Oraevsky, "Gold and silver nanoparticles as contrast agents for optoacoustic tomography," *Opt. Sci. Eng.,* vol. 144, pp. 373-386, 2009.
[185] V. Ntziachristos, and D. Razansky, "Molecular imaging by means of multispectral optoacoustic tomography (msot)," *Chemical Reviews,* vol. 110, pp. 2783-2794, 2010.
[186] V. Ntziachristos, "Going deeper than microscopy: The optical imaging frontier in biology," *Nat Meth,* vol. 7, pp. 603-614, 2010.
[187] C. Kim, H. M. Song, X. Cai, J. Yao, A. Wei, and L. V. Wang, "*In vivo* photoacoustic mapping of lymphatic systems with plasmon-resonant nanostars," *J Mater Chem,* vol. 21, pp. 2841-2844, 2011.
[188] L. V. Wang, and S. Hu, "Photoacoustic tomography: *In vivo* imaging from organelles to organs," *Science,* vol. 335, pp. 1458-1462, 2012.
[189] A. V. Liopo, A. Conjusteau, and A. A. Oraevsky, "Peg-coated gold nanorod monoclonal antibody conjugates in preclinical research with optoacoustic tomography, photothermal therapy, and sensing," in *Proc. SPIE*, 2012, p. 822344.
[190] W. Li, X. Cai, C. Kim, G. Sun, Y. Zhang, R. Deng, M. Yang, J. Chen*, et al.*, "Gold nanocages covered with thermally-responsive polymers for controlled release by high-intensity focused ultrasound," *Nanoscale,* vol. 3, pp. 1724-1730, 2011.
[191] V. P. Zharov, E. N. Galitovskaya, C. Johnson, and T. Kelly, "Synergistic enhancement of selective nanophotothermolysis with gold nanoclusters: Potential for cancer therapy," *Lasers in surgery and medicine,* vol. 37, pp. 219-226, 2005.
[192] W. F. Cheong, S. A. Prahl, and A. J. Welch, "A review of the optical properties of biological tissues," *IEEE Journal of Selected Topics in Quantum Electronics,* vol. 26, pp. 2166-2185, 1990.
[193] M. Sowa, L. Leonardi, A. Matas, B. Schattka, M. Hewko, J. Payette, and H. Mantsch, "Near infrared spectroscopy: *In vivo* tissue analysis," in *Encyclopedia of analytical chemistry*. vol. 1, R. Meyers, Ed., ed: John Wiley & Sons Ltd., 2000, pp. 251-281.
[194] M. Oishi, J. Nakaogami, T. Ishii, and Y. Nagasaki, "Smart pegylated gold nanoparticles for the cytoplasmic delivery of sirna to induce enhanced gene silencing," *Chemistry Letters,* vol. 35, pp. 1046-1047, 2006.
[195] S. E. Lee, G. L. Liu, F. Kim, and L. P. Lee, "Remote optical switch for localized andselective control of gene interference," *Nano Letters,* vol. 9, pp. 562-570, 2009.
[196] G. Wang, W. Sun, Y. Luo, and N. Fang, "Resolving rotational motions of nano-objects in engineered environments and live cells with gold nanorods and differential interference contrast microscopy," *Journal of the American Chemical Society,* vol. 132, pp. 16417-16422, 2010.
[197] D. Yeager, A. Karpiouk, B. Wang, J. Amirian, K. Sokolov, R. Smalling, and S. Emelianov, "Intravascular photoacoustic imaging of exogenously labeled atherosclerotic plaque through luminal blood," *J Biomed Opt,* vol. 17, p. 106016, 2012.

[198] T. S. Hauck, A. A. Ghazani, and W. C. W. Chan, "Assessing the effect of surface chemistry on gold nanorod uptake, toxicity, and gene expression in mammalian cells," *Small,* vol. 4, pp. 153-159, 2008.
[199] C. J. Murphy, A. M. Gole, J. W. Stone, P. N. Sisco, A. M. Alkilany, E. C. Goldsmith, and S. C. Baxter, "Gold nanoparticles in biology: Beyond toxicity to cellular imaging," *Accounts of Chemical Research,* vol. 41, pp. 1721-1730, 2008.
[200] R. Lévy, U. Shaheen, Y. Cesbron, and V. Sée, "Gold nanoparticles delivery in mammalian live cells: A critical review," *Nano Reviews,* vol. 1, 2010.
[201] B. Nikoobakht, and M. A. El-Sayed, "Evidence for bilayer assembly of cationic surfactants on the surface of gold nanorods," *Langmuir,* vol. 17, pp. 6368-6374, 2001.
[202] B. Nikoobakht, and M. A. El-Sayed, "Preparation and growth mechanism of gold nanorods (nrs) using seed-mediated growth method," *Chemistry of Materials,* vol. 15, pp. 1957-1962, 2003.
[203] C. Grabinski, N. Schaeublin, A. Wijaya, H. D'Couto, S. H. Baxamusa, K. Hamad-Schifferli, and S. M. Hussain, "Effect of gold nanorod surface chemistry on cellular response," *ACS Nano,* vol. 5, pp. 2870-2879, 2011.
[204] S. Perumal, A. Hofmann, N. Scholz, E. Rühl, and C. Graf, "Kinetics study of the binding of multivalent ligands on size-selected gold nanoparticles," *Langmuir,* vol. 27, pp. 4456-4464, 2011.
[205] C. Yu, L. Varghese, and J. Irudayaraj, "Surface modification of cetyltrimethylammonium bromide-capped gold nanorods to make molecular probes," *Langmuir,* vol. 23, pp. 9114-9119, 2007.
[206] C.-W. Wei, C.-K. Liao, Y.-Y. Chen, C.-R. C. Wang, A.-A. Ding, D.-B. Shiehd, and P.-C. Li, "*In vivo* photoacoustic imaging with multiple selective targeting using bioconjugated gold nanorods," in *Photons Plus Ultrasound: Imaging and Sensing 2008: The Ninth Conference on Biomedical Thermoacoustics, Optoacoustics, and Acousto-optics*, San Jose, CA, USA, 2008, pp. 68560J-11.
[207] H. Liao, and J. H. Hafner, "Gold nanorod bioconjugates," *Chemistry of Materials,* vol. 17, pp. 4636-4641, 2005.
[208] M. Eghtedari, A. V. Liopo, J. A. Copland, A. A. Oraevsky, and M. Motamedi, "Engineering of hetero-functional gold nanorods for the *in vivo* molecular targeting of breast cancer cells," *Nano Lett,* vol. 9, pp. 287-91, 2009.
[209] T. Niidome, M. Yamagata, Y. Okamoto, Y. Akiyama, H. Takahashi, T. Kawano, Y. Katayama, and Y. Niidome, "Peg-modified gold nanorods with a stealth character for *in vivo* applications," *Journal of Controlled Release,* vol. 114, pp. 343-347, 2006.
[210] S. Kumar, J. Aaron, and K. V. Sokolov, "Directional conjugation of antibodies to nanoparticles for synthesis of multiplexed optical contrast agents with both delivery and targeting moieties," *Nature Protocols,* vol. 3, pp. 314-320, 2008.
[211] G. Fleminger, E. Hadas, T. Wolf, and B. Solomon, "Oriented immobilization of periodate-oxidized monoclonal antibodies on amino and hydrazide derivatives of eupergit c," *Appl Biochem Biotechnol,* vol. 23, pp. 123-37, 1990.

[212] L. Vigderman, P. Manna, and E. R. Zubarev, "Quantitative replacement of cetyl trimethylammonium bromide by cationic thiol ligands on the surface of gold nanorods and their extremely large uptake by cancer cells," *Angewandte Chemie Int. Ed.,* vol. 51, pp. 636-641, 2012.
[213] J. L. Perry, K. G. Reuter, M. P. Kai, K. P. Herlihy, S. W. Jones, J. C. Luft, M. Napier, J. E. Bear*, et al.*, "Pegylated print nanoparticles: The impact of peg density on protein binding, macrophage association, biodistribution, and pharmacokinetics," *Nano Letters,* vol. 12, pp. 5304-5310, 2012.
[214] K. Bezdek, "Circle packings into convex domains of the euclidean and hyperbolic plane and the sphere.," *Geometriae Dedicata* vol. 21, pp. 249-255, 1986.
[215] B. Thierry, J. Ng, T. Krieg, and H. J. Griesser, "A robust procedure for the functionalization of gold nanorods and noble metal nanoparticles," *Chemical Communications,* vol. 0, pp. 1724-1726, 2009.
[216] G. Beamson, and D. Briggs, *High resolution xps of organic polymers : The scienta esca300 database*. Chichester [England]; New York: Wiley, 1992.
[217] N. Chanda, R. Shukla, K. V. Katti, and R. Kannan, "Gastrin releasing protein receptor specific gold nanorods: Breast and prostate tumor avid nanovectors for molecular imaging," *Nano Letters,* vol. 9, pp. 1798-1805, 2009.
[218] L. M. Liz-Marzán, J. Pérez-Juste, and I. Pastoriza-Santos, "Plasmonics of gold nanorods. Considerations for biosensing," in *Nanomaterials for application in medicine and biology*, M. Giersig, and G. B. Khomutov, Eds., ed: Springer Netherlands, 2008, pp. 103-111.
[219] X. Wang, Y. Li, H. Wang, Q. Fu, J. Peng, Y. Wang, J. Du, Y. Zhou*, et al.*, "Gold nanorod-based localized surface plasmon resonance biosensor for sensitive detection of hepatitis b virus in buffer, blood serum and plasma," *Biosensors and Bioelectronics,* vol. 26, pp. 404-410, 2010.
[220] A. M. Alkilany, P. K. Nagaria, C. R. Hexel, T. J. Shaw, C. J. Murphy, and M. D. Wyatt, "Cellular uptake and cytotoxicity of gold nanorods: Molecular origin of cytotoxicity and surface effects," *Small,* vol. 5, pp. 701-708, 2009.
[221] A. M. Alkilany, P. K. Nagaria, M. D. Wyatt, and C. J. Murphy, "Cation exchange on the surface of gold nanorods with a polymerizable surfactant: Polymerization, stability, and toxicity evaluation," *Langmuir,* vol. 26, pp. 9328-9333, 2010.
[222] J. Aaron, K. Travis, N. Harrison, and K. Sokolov, "Dynamic imaging of molecular assemblies in live cells based on nanoparticle plasmon resonance coupling," *Nano Letters,* vol. 9, pp. 3612-3618, 2009.
[223] P. Jha, D. Golovko, S. Bains, D. Hostetter, R. Meier, M. F. Wendland, and H. E. Daldrup-Link, "Monitoring of natural killer cell immunotherapy using noninvasive imaging modalities," *Cancer Res,* vol. 70, pp. 6109-13, 2010.
[224] C. E. Green, T. Liu, V. Montel, G. Hsiao, R. D. Lester, S. Subramaniam, S. L. Gonias, and R. L. Klemke, "Chemoattractant signaling between tumor cells and macrophages regulates cancer cell migration, metastasis and neovascularization," *PLoS One,* vol. 4, p. e6713, 2009.

[225] H. Hong, Y. Yang, Y. Zhang, and W. Cai, "Non-invasive cell tracking in cancer and cancer therapy," *Curr Top Med Chem,* vol. 10, pp. 1237-48, 2010.
[226] I. F. Tannock, C. M. Lee, J. K. Tunggal, D. S. Cowan, and M. J. Egorin, "Limited penetration of anticancer drugs through tumor tissue: A potential cause of resistance of solid tumors to chemotherapy," *Clin Cancer Res,* vol. 8, pp. 878-84, 2002.
[227] A. H. Kyle, L. A. Huxham, D. M. Yeoman, and A. I. Minchinton, "Limited tissue penetration of taxanes: A mechanism for resistance in solid tumors," *Clin Cancer Res,* vol. 13, pp. 2804-10, 2007.
[228] M. R. Choi, K. J. Stanton-Maxey, J. K. Stanley, C. S. Levin, R. Bardhan, D. Akin, S. Badve, J. Sturgis*, et al.*, "A cellular trojan horse for delivery of therapeutic nanoparticles into tumors," *Nano Lett,* vol. 7, pp. 3759-65, 2007.
[229] L. Kennedy, A. Bear, J. Young, N. Lewinski, J. Kim, A. Foster, and R. Drezek, "T cells enhance gold nanoparticle delivery to tumors *in vivo*," *Nanoscale Research Letters,* vol. 6, pp. 1-11, 2011.
[230] L. M. Ricles, S. Y. Nam, K. Sokolov, S. Y. Emelianov, and L. J. Suggs, "Function of mesenchymal stem cells following loading of gold nanotracers," *International J of Nanomedicine,* vol. 6, pp. 407-416, 2011.
[231] S. Y. Nam, L. M. Ricles, L. J. Suggs, and S. Y. Emelianov, "*In vivo* ultrasound and photoacoustic monitoring of mesenchymal stem cells labeled with gold nanotracers," *PLoS One,* vol. 7, p. e37267, 2012.
[232] A. A. Oraevsky, A. A. Karabutov, S. V. Solomatin, E. V. Savateeva, V. A. Andreev, Z. Gatalica, H. Singh, and R. D. Fleming, "Laser optoacoustic imaging of breast cancer *in vivo*," *Proceedings of SPIE,* vol. 4256, pp. 6-15, 2001.
[233] X. Wang, Y. Pang, G. Ku, X. Xie, G. Stoica, and L. V. Wang, "Noninvasive laser-induced photoacoustic tomography for structural and functional *in vivo* imaging of the brain," *Nature Biotechnology,* vol. 21, pp. 803-806, 2003.
[234] B. M. Reinhard, M. Siu, H. Agarwal, A. P. Alivisatos, and J. Liphardt, "Calibration of dynamic molecular rulers based on plasmon coupling between gold nanoparticles," *Nano Letters,* vol. 5, pp. 2246-2252, 2005.
[235] J. S. Aaron, N. Nitin, K. Travis, S. Kumar, T. Collier, S. Y. Park, M. José-Yacamán, L. Coghlan*, et al.*, "Plasmon resonance coupling of metal nanoparticles for molecular imaging of carcinogenesis *in vivo*," *J. Biomed. Opt.,* vol. 12, p. 034007, 2007.
[236] T. A. Larson, P. P. Joshi, and K. Sokolov, "Preventing protein adsorption and macrophage uptake of gold nanoparticles via a hydrophobic shield," *ACS Nano,* vol. 6, pp. 9182-90, 2012.
[237] T. P. Gustafson, Q. Cao, S. T. Wang, and M. Y. Berezin, "Design of irreversible optical nanothermometers for thermal ablations," *Chemical Communications,* vol. 49, pp. 680-2, 2013.
[238] A. Taruttis, E. Herzog, D. Razansky, and V. Ntziachristos, "Real-time imaging of cardiovascular dynamics and circulating gold nanorods with multispectral optoacoustic tomography," *Opt. Express,* vol. 18, pp. 19592-19602, 2010.

[239] F. Ratto, P. Matteini, S. Centi, F. Rossi, and R. Pini, "Gold nanorods as new nanochromophores for photothermal therapies," *Journal of Biophotonics,* vol. 4, pp. 64-73, 2011.
[240] Arnida, M. M. Janát-Amsbury, A. Ray, C. M. Peterson, and H. Ghandehari, "Geometry and surface characteristics of gold nanoparticles influence their biodistribution and uptake by macrophages," *European Journal of Pharmaceutics and Biopharmaceutics,* vol. 77, pp. 417-423, 2011.
[241] Y.-S. Chen, W. Frey, S. Kim, K. Homan, P. Kruizinga, K. Sokolov, and S. Emelianov, "Enhanced thermal stability of silica-coated gold nanorods for photoacoustic imaging and image-guided therapy," *Optics Express,* vol. 18, pp. 8867-8878, 2010.
[242] J. Godoy-Navajas, M. P. Aguilar-Caballos, and A. Gomez-Hens, "Synthesis and characterization of oxazine-doped silica nanoparticles for their potential use as stable fluorescent reagents," *J Fluoresc,* vol. 20, pp. 171-80, 2010.
[243] H. Shi, X. He, K. Wang, Y. Yuan, K. Deng, J. Chen, and W. Tan, "Rhodamine b isothiocyanate doped silica-coated fluorescent nanoparticles (rbitc-dsfnps)–based bioprobes conjugated to annexin v for apoptosis detection and imaging," *Nanomedicine: Nanotechnology, Biology and Medicine,* vol. 3, pp. 266-272, 2007.
[244] R. Snyderman, M. C. Pike, D. G. Fischer, and H. S. Koren, "Biologic and biochemical activities of continuous macrophage cell lines p388d1 and j774.1," *The Journal of Immunology,* vol. 119, pp. 2060-2066, 1977.
[245] R. Goldman, "Induction of a high phagocytic capability in p388d1, a macrophage-like tumor cell line, by 1α,25-dihydroxyvitamin d3," *Cancer Research,* vol. 44, pp. 11-19, 1984.
[246] L. L. Chen, L. Jiang, Y. L. Wang, J. Qian, and S. He, "Multilayered polyelectrolyte-coated gold nanorods as multifunctional optical contrast agents for cancer cell imaging," *J Zhejiang Univ Sci B,* vol. 11, pp. 417-22, 2010.
[247] A. K. Oyelere, P. C. Chen, X. Huang, I. H. El-Sayed, and M. A. El-Sayed, "Peptide-conjugated gold nanorods for nuclear targeting," *Bioconjugate Chemistry,* vol. 18, pp. 1490-1497, 2007.
[248] H. Ding, K.-T. Yong, I. Roy, H. E. Pudavar, W. C. Law, E. J. Bergey, and P. N. Prasad, "Gold nanorods coated with multilayer polyelectrolyte as contrast agents for multimodal imaging," *The Journal of Physical Chemistry C,* vol. 111, pp. 12552-12557, 2007.
[249] C. Ungureanu, R. Kroes, W. Petersen, T. A. M. Groothuis, F. Ungureanu, H. Janssen, F. W. B. van Leeuwen, R. P. H. Kooyman*, et al.*, "Light interactions with gold nanorods and cells: Implications for photothermal nanotherapeutics," *Nano Letters,* vol. 11, pp. 1887-1894, 2011.
[250] C. L. Bayer, S. Y. Nam, Y. S. Chen, and S. Y. Emelianov, "Photoacoustic signal amplification through plasmonic nanoparticle aggregation," *J Biomed Opt,* vol. 18, p. 16001, 2013.

[251] B. Fisher, B. S. Packard, E. J. Read, J. A. Carrasquillo, C. S. Carter, S. L. Topalian, J. C. Yang, P. Yolles*, et al.*, "Tumor localization of adoptively transferred indium-111 labeled tumor infiltrating lymphocytes in patients with metastatic melanoma," *J Clin Oncol,* vol. 7, pp. 250-61, 1989.
[252] F. Hirschhaeuser, H. Menne, C. Dittfeld, J. West, W. Mueller-Klieser, and L. A. Kunz-Schughart, "Multicellular tumor spheroids: An underestimated tool is catching up again," *J Biotechnol,* vol. 148, pp. 3-15, 2010.
[253] Y. S. Chen, W. Frey, S. Kim, P. Kruizinga, K. Homan, and S. Emelianov, "Silica-coated gold nanorods as photoacoustic signal nanoamplifiers," *Nano Lett,* vol. 11, pp. 348-54, 2011.
[254] L. Balogh, S. S. Nigavekar, B. M. Nair, W. Lesniak, C. Zhang, L. Y. Sung, M. S. T. Kariapper, A. El-Jawahri*, et al.*, "Significant effect of size on the *in vivo* biodistribution of gold composite nanodevices in mouse tumor models," *Nanomedicine: Nanotechnology, Biology and Medicine,* vol. 3, pp. 281-296, 2007.
[255] M. L. Schipper, G. Iyer, A. L. Koh, Z. Cheng, Y. Ebenstein, A. Aharoni, S. Keren, L. A. Bentolila*, et al.*, "Particle size, surface coating, and pegylation influence the biodistribution of quantum dots in living mice," *Small,* vol. 5, pp. 126-134, 2009.
[256] L. Tong, W. He, Y. Zhang, W. Zheng, and J. X. Cheng, "Visualizing systemic clearance and cellular level biodistribution of gold nanorods by intrinsic two-photon luminescence," *Langmuir,* vol. 25, pp. 12454-9, 2009.
[257] G. P. Goodrich, L. Bao, K. Gill-Sharp, K. L. Sang, J. Wang, and J. D. Payne, "Photothermal therapy in a murine colon cancer model using near-infrared absorbing gold nanorods," *J Biomed Opt,* vol. 15, p. 018001, 2010.
[258] A. K. Murthy, R. J. Stover, W. G. Hardin, R. Schramm, G. D. Nie, S. Gourisankar, T. M. Truskett, K. V. Sokolov*, et al.*, "Charged gold nanoparticles with essentially zero serum protein adsorption in undiluted fetal bovine serum," *J Am Chem Soc,* vol. 135, pp. 7799-802, 2013.
[259] J. O. Tam, "Interactions of composite gold nanoparticles with cells and tissue : Implications in clinical translation for cancer imaging and therapy," Doctor of Philosophy PhD Thesis, Biomedical Engineering, University of Texas at Austin, Austin, 2012.
[260] E. Sadauskas, H. Wallin, M. Stoltenberg, U. Vogel, P. Doering, A. Larsen, and G. Danscher, "Kupffer cells are central in the removal of nanoparticles from the organism," *Particle and Fibre Toxicology,* vol. 4, pp. 1-7, 2007.
[261] P. F. Lalor, W. K. Lai, S. M. Curbishley, S. Shetty, and D. H. Adams, "Human hepatic sinusoidal endothelial cells can be distinguished by expression of phenotypic markers related to their specialised functions *in vivo*," *World J Gastroenterol,* vol. 12, pp. 5429-39, 2006.
[262] S. A. Mousavi, M. Sporstol, C. Fladeby, R. Kjeken, N. Barois, and T. Berg, "Receptor-mediated endocytosis of immune complexes in rat liver sinusoidal

endothelial cells is mediated by fcgammariib2," *Hepatology,* vol. 46, pp. 871-84, 2007.
[263] K. Elvevold, B. Smedsrod, and I. Martinez, "The liver sinusoidal endothelial cell: A cell type of controversial and confusing identity," *Am J Physiol Gastrointest Liver Physiol,* vol. 294, pp. G391-400, 2008.
[264] L. P. Ganesan, S. Mohanty, J. Kim, K. R. Clark, J. M. Robinson, and C. L. Anderson, "Rapid and efficient clearance of blood-borne virus by liver sinusoidal endothelium," *PLoS Pathog,* vol. 7, p. e1002281, 2011.
[265] K. K. Sørensen, P. McCourt, T. Berg, C. Crossley, D. L. Couteur, K. Wake, and B. Smedsrød, "The scavenger endothelial cell: A new player in homeostasis and immunity," *American Journal of Physiology - Regulatory, Integrative and Comparative Physiology,* vol. 303, pp. R1217-R1230, 2012.
[266] R. Kjeken, S. A. Mousavi, A. Brech, T. Gjøen, and T. Berg, "Fluid phase endocytosis of [125i]iodixanol in rat liver parenchymal, endothelial and kupffer cells," *Cell and Tissue Research,* vol. 304, pp. 221-230, 2001.
[267] C. J. Detzel, W. Leng, P. J. Vikesland, and P. Rajagopalan, "Intracellular localization and kinetics of uptake and clearance of gold nanoparticles in primary hepatic cells," *Nano LIFE,* vol. 02, p. 1241008, 2012.
[268] L. Bouwens, M. Baekeland, R. De Zanger, and E. Wisse, "Quantitation, tissue distribution and proliferation kinetics of kupffer cells in normal rat liver," *Hepatology,* vol. 6, pp. 718-22, 1986.
[269] B. G. Lopez, M. S. Tsai, J. L. Baratta, K. J. Longmuir, and R. T. Robertson, "Characterization of kupffer cells in livers of developing mice," *Comp Hepatol,* vol. 10, p. 2, 2011.
[270] S. M. Goorden, T. E. Buffart, A. Bakker, and M. M. Buijs, "[liver disorders in adults: Alt and ast]," *Ned Tijdschr Geneeskd,* vol. 157, p. A6443, 2013.
[271] D. Bazile, C. Prud'homme, M. T. Bassoullet, M. Marlard, G. Spenlehauer, and M. Veillard, "Stealth me.Peg-pla nanoparticles avoid uptake by the mononuclear phagocytes system," *J Pharm Sci,* vol. 84, pp. 493-8, 1995.
[272] M. T. Peracchia, E. Fattal, D. Desmaele, M. Besnard, J. P. Noel, J. M. Gomis, M. Appel, J. d'Angelo*, et al.*, "Stealth pegylated polycyanoacrylate nanoparticles for intravenous administration and splenic targeting," *J Control Release,* vol. 60, pp. 121-8, 1999.
[273] D. E. Owens, 3rd, and N. A. Peppas, "Opsonization, biodistribution, and pharmacokinetics of polymeric nanoparticles," *Int J Pharm,* vol. 307, pp. 93-102, 2006.
[274] L. P. Smith, K. W. Hunter, E. C. Oldfield, and G. T. Strickland, "Murine malaria: Blood clearance and organ sequestration of plasmodium yoelii-infected erythrocytes," *Infect Immun,* vol. 38, pp. 162-7, 1982.
[275] S. M. Moghimi, C. J. Porter, I. S. Muir, L. Illum, and S. S. Davis, "Non-phagocytic uptake of intravenously injected microspheres in rat spleen: Influence of particle size and hydrophilic coating," *Biochem Biophys Res Commun,* vol. 177, pp. 861-6, 1991.

[276] R. E. Mebius, and G. Kraal, "Structure and function of the spleen," *Nat Rev Immunol,* vol. 5, pp. 606-16, 2005.
[277] I. C. Lin, M. Liang, T. Y. Liu, Z. M. Ziora, M. J. Monteiro, and I. Toth, "Interaction of densely polymer-coated gold nanoparticles with epithelial caco-2 monolayers," *Biomacromolecules,* vol. 12, pp. 1339-48, 2011.
[278] J. Panyam, W. Z. Zhou, S. Prabha, S. K. Sahoo, and V. Labhasetwar, "Rapid endo-lysosomal escape of poly(dl-lactide-co-glycolide) nanoparticles: Implications for drug and gene delivery," *FASEB J,* vol. 16, pp. 1217-26, 2002.
[279] I. C. Lin, M. Liang, T. Y. Liu, M. J. Monteiro, and I. Toth, "Cellular transport pathways of polymer coated gold nanoparticles," *Nanomedicine,* vol. 8, pp. 8-11, 2012.
[280] L. C. Wu, L. W. Chu, L. W. Lo, Y. C. Liao, Y. C. Wang, and C. S. Yang, "Programmable cellular retention of nanoparticles by replacing the synergistic anion of transferrin," *ACS Nano,* vol. 7, pp. 365-75, 2013.
[281] J. S. Park, T. H. Han, K. Y. Lee, S. S. Han, J. J. Hwang, D. H. Moon, S. Y. Kim, and Y. W. Cho, "N-acetyl histidine-conjugated glycol chitosan self-assembled nanoparticles for intracytoplasmic delivery of drugs: Endocytosis, exocytosis and drug release," *J Control Release,* vol. 115, pp. 37-45, 2006.
[282] J. Park, and Y. Cho, "*In vitro* cellular uptake and cytotoxicity of paclitaxel-loaded glycol chitosan self-assembled nanoparticles," *Macromolecular Research,* vol. 15, pp. 513-519, 2007.
[283] K. Tahara, S. Tadokoro, H. Yamamoto, Y. Kawashima, and N. Hirashima, "The suppression of ige-mediated histamine release from mast cells following exocytic exclusion of biodegradable polymeric nanoparticles," *Biomaterials,* vol. 33, pp. 343-51, 2012.
[284] L. D. DeLeve, "Liver sinusoidal endothelial cells and liver regeneration," *J Clin Invest,* vol. 123, pp. 1861-6, 2013.
[285] Y. T. Nguyen, H. K. Kim, J. S. Kwon, Y. S. Kim, T. R. Yoon, Y. Ahn, M. H. Jeong, and I. K. Park, "Efficient transfer of reporter gene-loaded nanoparticles to bone marrow stromal cells (d1) by reverse transfection," *J Nanosci Nanotechnol,* vol. 10, pp. 3170-4, 2010.
[286] S. C. Berman, C. Galpoththawela, A. A. Gilad, J. W. Bulte, and P. Walczak, "Long-term mr cell tracking of neural stem cells grafted in immunocompetent versus immunodeficient mice reveals distinct differences in contrast between live and dead cells," *Magn Reson Med,* vol. 65, pp. 564-74, 2011.
[287] Y. Liang, P. Walczak, and J. W. Bulte, "Comparison of red-shifted firefly luciferase ppy re9 and conventional luc2 as bioluminescence imaging reporter genes for *in vivo* imaging of stem cells," *J Biomed Opt,* vol. 17, p. 016004, 2012.
[288] L. M. Traub, "Tickets to ride: Selecting cargo for clathrin-regulated internalization," *Nat Rev Mol Cell Biol,* vol. 10, pp. 583-96, 2009.
[289] M. C. Field, A. Sali, and M. P. Rout, "Evolution: On a bender--bars, escrts, cops, and finally getting your coat," *J Cell Biol,* vol. 193, pp. 963-72, 2011.

Vita

Pratixa Paritosh Joshi graduated from high school in Gujarat, India in 1994. She then attended Dharamsinh Desai Institute of Technology in Nadiad, Gujarat and received a Bachelor's of Engineering in Chemical Engineering in 1998. After getting married, she followed her husband to the United States. After two years of intensive study, she obtained a Master's of Science degree in Chemical Engineering at the University of Oklahoma in 2004. Her Master's thesis focused on the design of sensitive glucose sensors based on redox polymer and carbon nanotubes. In 2005, she started working as a research associate at the University of Texas Health Science Center at Houston before joining the University of Texas at Austin in 2008. At UT-Austin, she continued her full-time employment in the laboratory of Dr. Konstantin Sokolov and worked towards her Ph.D. on a staff education benefit.

Permanent email address: joshipratixa@yahoo.com
This dissertation was typed by the author.